NAGAOKA UNIVERSITY OF TECHNOLOGY

DOCTORAL THESIS

Estimation of Ultimate Lateral Resistance of Pile Group, and Ultimate Bearing Capacity of Rigid Footing under Complex Load by using Rigid Plastic Finite Element Method

剛塑性有限要素法による群杭の極限横抵抗力と複合荷重に対する剛基礎の極限支持力の評価

Author:
PHAM Ngoc Quang

Supervisor:
Professor OHTSUKA Satoru

A thesis submitted in partial fulfillment of the requirements for the degree of

Doctor of Engineering

in

Energy and Environment Science

Examination committees: Professor Dr. Eng. Ohtsuka Satoru (Chairman)
Professor Dr. Eng. Sugimoto Mitsutaka
Assoc. Professor Dr. Eng. Kobayashi Shunichi
Assoc. Professor Dr. Eng. Toyota Hirofumi
Assoc. Professor Dr. Agri. Fukumoto Yutaka

Department of Civil and Environmental Engineering
Nagaoka University of Technology
Niigata, JAPAN 2020

August-2020

Declaration of Authorship

I, PHAM Ngoc Quang, declare that this thesis titled "Estimation of ultimate lateral resistance of pile group, and ultimate bearing capacity of rigid footing under complex load by using rigid plastic finite element method" and the work presented in it, are my own. I confirm that:

- This work was done wholly or mainly while in candidature for a research degree at this University

- Where any part of this thesis has previously been submitted for a degree or any other qualification at this University or any other institution, this has been clearly stated.

- Where I have consulted the published work of others, this is always clearly attributed.

- Where I have quoted from the work of others, the source is always given. With the exception of such quotations, this thesis is entirely my own work.

- I have acknowledged all main sources of help.

- Where the thesis is based on work done by myself jointly with others, I have made clear exactly what was done by others and what I have contributed myself.

………………………   …………………...

Student's signature   Date

I certify that I have read this dissertation and that, in my opinion, it is fully adequate in scope and quality as a dissertation for the three-years degree of Doctor of Engineering.

………………………   …………………...

Suppervisor's signature   Date

(Prof. Ohtsuka Satoru)

Abstract

In design of building, the pile foundations and the rigid footings have routinely been designed to carry the vertical load of the superstructure, resist the horizontal load from wind and wave loads, and the moment load coming from the eccentric vertical or horizontal loads. This study mainly focuses on the following objectives by using the rigid plastic finite element method (RPFEM); 1) The assessment for group effect on ultimate lateral resistance of piles against uniform ground movement; 2) Ultimate bearing capacity of rigid footing under eccentric vertical load; 3) Limit load space of rigid footing under eccentrically inclined load; and 4) Ultimate bearing capacity of rigid footing resting on sand layer over clay:

[1] Firstly, in earthquake engineering, pile foundations have typically been designed to withstand the lateral loading that results from large displacements due to ground movement caused by strong earthquakes during which the distress and failure of superstructures may take place when the lateral load exceeds the ultimate lateral resistance of the piles. The aim of this study is to estimate the ultimate lateral resistance of piles especially in terms of the group effect induced by the pile arrangement. Several experimental and numerical analyses have been conducted on pile groups to investigate the group effect when the groups are subjected to uniform large horizontal ground movement. However, these previous studies usually calculated the ultimate lateral resistance of the pile groups by applying the load to the piles. The present study directly assesses the ultimate lateral resistance of pile groups against ground movement by systematically varying the direction of the ground movement. Although the load bearing ratio of each pile in a pile group, defined as the ratio of the ultimate lateral resistance of each pile in a pile group to that of a single pile, is an important design criterion, it was difficult to assess in past works. This study focuses on the load bearing ratio of each pile against ground movement in various directions. The use of the finite element method (FEM) provides options for simulating the pile-soil system with complex pile arrangements by taking the complicated geometry of the problem into account. The ultimate lateral resistance is examined here for pile groups consisting of a 2x2 arrangement of four piles, as well as two piles, three piles, four piles, and an infinite number of piles arranged in a row through case studies in which the pile spacing is changed by applying the two-dimensional rigid plastic finite element method (RPFEM). The RPFEM was extended in this work to calculate not only the total ultimate lateral resistance of pile groups, but also the load bearing

ratio of the piles in the group. The obtained results indicate that the load bearing ratio generally increases with an increase in pile spacing and converges to almost unity at a pile spacing ratio of 3.0 with respect to the pile diameter. Moreover, the group effect was further investigated by considering the failure mode of the ground around the piles.

(2) Secondly, in geotechnical engineering, the stability of rigid footings under eccentric vertical loads is an important issue. This is because the number of superstructure buildings has increased and the situation of structures being subjected to eccentric vertical loading is occurring more and more frequently. In this study, focus is placed on the ultimate bearing capacity of a footing against the eccentric load placed on two types of soil, namely, sandy soil and clayey soil, using a finite element analysis. For the sandy soil, the study newly introduces an interface element into the footing-soil system in order to properly evaluate the interaction between the footing and the soil, which greatly affects the failure mechanism of the footing-soil system. For the clayey soil, the study improves the analysis procedure by introducing a zero-tension analysis into the footing-soil system. Two friction conditions between the footing and the soils are considered; one models a perfectly rough condition and the other models a perfectly smooth condition. For a two-dimensional analysis of the footing-soil system, the rigid plastic finite element method (RPFEM) is applied to calculate the ultimate bearing capacity of the eccentrically loaded footing. The RPFEM is extended in this work to calculate not only the ultimate bearing capacity, but also the distribution of contact stress along the footing base. The study thoroughly investigates the effect of the eccentric vertical load on the ultimate bearing capacity in the normalized form of V/V_{ult} and e/B where e is the length of the eccentricity and B is the width of the footing. V_{ult} indicates the ultimate bearing capacity for the centric vertical load. The failure envelope in the plane of V/V_{ult} and M/BV_{ult} is further investigated under various conditions for the sandy and clayey soils. M is the moment load induced by the eccentric vertical load. This study examines the applicability of the failure envelope obtained for the eccentric vertical load to the cases where two variables, V and M, are independently prescribed. The obtained results are coincident and indicate the wide applicability of the failure envelope in the normalized V-M plane in practice. Finally, in a comparison with previous researches, the numerical data in the present study lead to the derivation of new equations for the failure envelopes of both sandy and clayey soils.

(3) Thirdly, the objective of this study was to evaluate the bearing capacity of a rigid footing on the free

surface of uniform sandy and clayey soils under the action of eccentric and inclined loading using a finite element analysis by assuming that the soils follow the Drucker-Prager yield function. In the two-dimensional analysis of the footing-soil system, the rigid plastic finite element method (RPFEM) was applied to calculate the ultimate bearing capacity of the eccentric-inclined loaded footing. In the numerical analysis, an interface element was introduced to simulate the footing-soil system with the rigid plastic constitutive equation developed by the authors. The footing was considered to be rigid and rough, as it most often is in reality. This study thoroughly considered the effect of the soil properties on load inclination factors i_γ and i_c in order to investigate the validity of the current design methods. In particular, the effects of the horizontal load in two directions on the ultimate bearing capacity of the footing and the failure envelopes in the V-H-M space were clarified, namely, positive and negative horizontal loads. The results showed that the positive horizontal load had a negative effect on the bearing capacity, while the negative horizontal load had the opposite effect in the presence of eccentrically inclined loading. The failure mode of the footing-soil system was clearly seen in the difference between the two directions of horizontal load. Through a series of numerical analyses, new equations were proposed for load inclination factors i_γ and i_c, and for the failure envelopes in the V-H-M space, taking into account the direction of the horizontal load. The obtained limit load space was proved to be rational in comparison to those given in the literature. Furthermore, the applicability of the limit load space to different computation conditions and independently prescribed moments was examined. Consequently, the failure envelope for each type of soil in the V-H-M space was clearly seen to be unique.

(4) Finally, this study investigates the ultimate bearing capacity of a rigid footing on the free surface of sand overlying clay using the rigid plastic finite element method (RPFEM). An interface element is newly introduced to properly evaluate the interaction between the footing and the soil, which greatly effects the failure mechanism of the footing-soil system. Two friction conditions are employed for the footing surface, namely, perfectly rough and perfectly smooth. The RPFEM is extended to calculate the distribution of contact normal stress along the footing base corresponding to changes in the thickness of the sand layer. The improvement in the bearing capacity is intensified by increasing the internal friction angle and the thickness of the sand layer. Two cases are considered for the clay layer below the sand layer, namely, a weak layer and a stiff layer. The failure mode of two-layered soils is found to change from the general shear

mode to the punching shear mode by a reduction in the shear strength of the clay layer. In the general shear mode, the sheared area of the ground is limited to the sand layer, while in the punching shear mode, the sheared area is distributed throughout the two layers. Therefore, the ultimate bearing capacity obtained here is lower than that of a single layer of sandy soil in the case of the punching shear mode. In this study, a bearing capacity formula for the punching shear mode is newly proposed based on the computed results.

Acknowledgements

List of Symbols

Material parameters

c Cohesion of soil

c_s Cohesion at the contact plane

ϕ Internal friction angle of soil

ϕ_s Internal friction angle at the contact plane

γ Unit weight of soil

a,b The material constant

Hyperplasticity parameters

$\dot{\varepsilon}$ Vector of total strain

$\dot{e}$ The norm of strain rate

I_1 The first invariant of stress

J_2 Second invariant of deviator stress

κ Penalty constant

σ_{ij} Stress

s_{ij} Deviator stress

t_s Shear component of stress vector at the contact plane

t_n Normal component of stress vector at the contact plane

Lateral resistance parameters

p_u Ultimate lateral resistance of single pile

D Outside diameter of pile

S Pile spacing

L Square pile

α Direction of ground movement

Bearing capacity parameters

q Ultimate bearing capacity

i_γ, i_c, i_q Load inclination factor

N_c Cohesion factor

N_q Deep surcharge factor

N_γ Self-weight factor

α Load inclination angle

σ_n Contact normal stress

τ Contact shear stress

K_p Coefficient of passive earth pressure

K_s Punching shear coefficient

δ Mobilized friction angle

θ Shear angle of rigid sand block

D Sand layer thickness

Footing parameters

B Footing width

B' Effective footing width

e Eccentricity

Load parameters

V Vertical load

V_{ult} Ultimate bearing capacity of centric vertical load

H Horizontal load

M Moment load

Publications

A. Peer Reviewed Journal

1. Pham, N. Quang, Ohtsuka, S., Isobe, K. and Fukumoto, Y.: Group effect on ultimate lateral resistance of piles against uniform ground movement, Soils and Foundations, 59(1), 27-40, 2019. https://doi.org/10.1016/j.sandf.2018.08.013.

2. Pham, N. Quang, Ohtsuka, S., Isobe, K. and Fukumoto, Y., Hoshina, T.: Ultimate bearing capacity of rigid footing under eccentric vertical load, Soils and Foundations, 59(6), 1980-1991,2019. https://doi.org/10.1016/j.sandf.2019.09.004.

3. Pham, N. Quang, Ohtsuka, S., Isobe, K. and Fukumoto, Y.: Limit load space of rigid footing under eccentric inclined load, Soils and Foundations, 60(4), 1-14, 2020. https://doi.org/10.1016/j.sandf.2020.05.004.

B. Full Paper Peer Reviewed-International Proceeding

1. Pham, N. Quang, Ohtsuka, S., Isobe, K. and Fukumoto, Y.: Group effect on ultimate lateral resistance of piles in clayey soils against horizontal ground movement, Proceedings of the 15th International Conference of the International Association for Computer Methods and Advances in Geomechanics, Wuhan, China, USB, 2017.

2. Pham, N. Quang, Ohtsuka, S., Isobe, K. and Fukumoto, Y.: Ultimate lateral resistance of pile group in clayey soils against various direction of ground movement, Proceedings of the 1st Vietnam Symposium on Advances in Offshore Engineering - Energy and Geotechnics, Hanoi, Vietnam, Vol.1, pp.408-414, 2018. https://doi.org/10.1007/978-981-13-2306-5_57.

3. Pham, N. Quang, Ohtsuka, S., Isobe, K. and Fukumoto, Y.: Ultimate bearing capacity of footing on sandy soil against eccentric vertical load, Proceeding of the 4th International Conference on Geotechnics for Sustainable Infrastructure Development - Geotec Hanoi, Vietnam, Vol.4, pp.1135-1142, 2019. https://doi.org/10.1007/978-981-15-2184-3_148

(4) Pham, N.Quang, Ohtsuka, S., Isobe, K. and Fukumoto, Y.: Effect of Ground Movement Direction on Ultimate Lateral Resistance of Line Alignment Piles in Clay, Transactions on GIGAKU, Vol.6, No.1, pp.06003/1-06003/8, 2019.

(5) Pham, N.Quang, Ohtsuka, S., Isobe, K. and Fukumoto, Y.: Consideration on limit load space of footing on various soils under eccentric vertical load, Proceeding of the 16th International Conference of the International Association for Computer Methods and Advances in Geomechanics, Torino-Italy, Vol..16, 1-8, 2020. Accepted

C. National Conference Papers

(1) Pham, N.Quang, Ohtsuka, S., and Fukumoto, Y.: Estimation of ultimate lateral resistance of pile groups in clayey soils owing to horizontal ground movement, The 2nd STI-Gigaku(International Gigaku Conference in Nagaoka)-Japan, 105, 2017.

(2) Pham, N.Quang, Ohtsuka, S., Isobe, K. and Fukumoto, Y.: Group effect on ultimate lateral resistance of piles against uniform ground movement, The 53rd Japan National Conference on Geotechnical Engineering, Vol.53, pp.1359-1360, 2018.

(3) Pham, N.Quang, Ohtsuka, S., Isobe, K. and Fukumoto, Y.: Effect of Ground Movement Direction on Ultimate Lateral Resistance of Line Alignment Piles in Clay, The 7th International GIGAKU Conference in Nagaoka, pp.57, 2018.

(4) Pham, N.Quang, Ohtsuka, S., Fukumoto, Y., and Fukumoto Y.: Ultimate bearing capacity of rigid footing on sandy soil against eccentric vertical load, The 54rd Japan National Conference on Geotechnical Engineering, Vol.54, pp.1187-1188, 2019

(5) Ohtsuka, S., Dung, A. Huynh, Pham, N.Quang.: Examination on applicability of ultimate bearing capacity formula by taking account of size effect of footing, The 22nd Applied Mechanics Symposium, Japan Society of Civil Engineers, Vol. 22, pp353-354, 2019

(6) Pham, N.Quang, Ohtsuka, S., Fukumoto, Y., and Fukumoto Y: Ultimate bearing capacity of rigid footing on sandy soils for eccentrically inclined load. The 4th STI-Gigaku (International Gigaku Conference in Nagaoka)-Japan, 2019.

(7) Dung, A. Huynh, Pham, N.Quang., Ohtsuka, S., Fukumoto, Y.: Numerical analyses for ultimate bearing

capacity formula of intermediate soil ground in consideration of scale effect of foundation, The 54rd Japan National Conference on Geotechnical Engineering, Vol.54, pp.1149-1150, 2019.

(8) Pham, N.Quang, Ohtsuka, S., Isobe, K., and Fukumoto Y.: Ultimate bearing capacity of rigid footing on sandy soil against eccentrically inclined load, The 55rd Japan National Conference on Geotechnical Engineering, Vol.55, pp.1-2, 2020.

Contents

List of figures

List of tables

Chapter 1

INTRODUCTION

1.1 BACKGROUND AND PURPOSES

In earthquake engineering, the stability of pile foundations under the horizontal ground movement is an important issue, because that the earthquake is occurring more and more frequently. Ultimate lateral resistance of piles is an important design value which expresses the load applied to the pile which is p_u. Although there are several methods available for predicting ultimate lateral resistance of piles. For example, Broms (1964) studied the slip line method to calculate the ultimate lateral resistance of singe pile driven into cohesive soil. He reported the values of p_u in the range of 8.28 c_u – 12.56 c_u for various piles with circular and rectangular shapes and with smooth and rough surfaces, in which c_u was the undrained shear strength of the ground. Randolph and Houlsby (1984) used two-dimensional lower-bound and upper-bound limit analyses to provide the collapse load for circular piles in cohesion soil. The ultimate lateral resistance of the single pile was in the range of 9.14 c_u for perfectly smooth piles to 11.94 c_u for perfectly rough piles. However, more complex problem arises for pile groups because the ultimate lateral resistance of each pile is different among all the piles in a pile group due to the pile-soil-pile interaction effect. The support of each pile in a group leads to the total of the ultimate lateral resistance that is greatly varied by the pile spacing. It required that the group effect problem in a group have to be investigated. The group effect on ultimate lateral resistance has been investigated by several researcher using numerical analysis and model test. Stewart (1992), Chen (1994), Chen and Poulos (1997), and Goh et al. (1997) used numerical analyses to calculate the ultimate lateral resistance of pile groups against horizontal ground movement. The analyses showed that the ultimate lateral resistance of a pile in a pile group was generally lower than that of a single pile due to the pile-soil interaction. The same results were also obtained in model tests conducted by Cox et al. (1984), Chen and Poulos et al. (1997), Pan (1998), Pan et al. (2002), Llyas et al. (2004), Miao (2005), Miao et al. (2008), and Bauer et al. (2016). In this study, the pile-soil system is simulated by employing a rigid plastic finite element analysis (RPFEM) based on the upper bound theorem. The effect of the direction of the ground movement and the pile arrangement on the ultimate lateral resistance of pile groups

and the load bearing ratio of each pile is investigated. Pile groups consisting of a 2x2 arrangement of four piles, as well as two piles, three piles, four piles, and an infinite number of piles arranged in a row are intensively investigated by changing the pile spacing.

In geotechnical engineering, rigid footings have routinely been designed to withstand the complex loads that result from the combination of vertical and horizontal as well as moment loads. Typically, the vertical load stems from the weight of the superstructure, the horizontal load comes from wind and wave loads and the moment load comes from the eccentric vertical or horizontal loads. In practice, rigid footings often suffer under the eccentric vertical or the eccentrically inclined loads. Therefore, the stability of a rigid footing on the free surface of soils under complex loading is of practical interest. Estimation of the ultimate bearing capacity of the rigid footing is one of the complicated problems in practice. Many formulas were proposed to calculate the ultimate bearing capacity, such as, Terzaghi (1943), Meryerhof (1951, 1953, 1963), Hansen (1961, 1970) and Vesic (1973, 1975) by producing a series of model test on sandy and clayey soils. Although many works have been performed to investigate the ultimate bearing capacity against the eccentric vertical and the eccentrically inclined loadings, a comprehensive understanding of both the failure mechanism of the footing-soil system and the failure envelopes in the vertical load - horizontal load - moment (V-H-M) space has not yet been established. In footing-soil systems, the ultimate bearing capacity of the footing depends on the friction condition between the footing and the soil, which has been modeled under one of two extreme conditions, namely, perfectly rough and perfectly smooth. However, only a few researches have been conducted to evaluate the ultimate bearing capacity under two friction conditions of the footing-soil surface. In addition, most of the previous studies on clayey soil, such as those by Bransby (2001), Gourvenec (2008) and Khitas et al. (2017), considered a fully bonded interface between the footing and the soil which is capable of transmitting full tension. However, the occurrence of tensile stress in the soil was not real. Some literature is available on rigid footings under eccentric vertical loads with a zero-tension interface. Their finding raises the question of the effect of the footing-soil tensile stress on the ultimate bearing capacity and the failure mechanism in the presence of eccentric loading. In this study, a zero-tension analysis is introduced to widely consider the interaction between the footing and the soil in clayey soil.

Under eccentrically inclined loading, most of the previous studies, such as those by Loukidis et al.

(2008), Krabbenhoft et al. (2013), and Shen et al. (2016), investigated the bearing capacity of eccentrically inclined loaded footings without considering the effect of the direction of the horizontal loads on the failure envelopes in the *V-H-M* space or the failure mechanism of the footing-soil system. Their findings raise a question as to whether the direction of the horizontal loads has an effect on the ultimate bearing capacity and the failure mechanism in the presence of eccentrically inclined loading. Focus is placed here on the ultimate bearing capacity of a footing against the action of eccentric and inclined loads taking into account the direction of the horizontal loads.

In geotechnical practice, the top layer of soft clay in native soils is often replaced by cohesionless soil in order to improve the bearing capacity of the substrate. The failure mechanisms of the two-layered soils are complex because the failure may break through the upper sand layer to the lower clay layer, or may only be within the sand layer. The question is raised as to whether the soil properties and geometric conditions of the top sand layer or the below clay layer has an effect the ultimate bearing capacity and the failure mechanism in the presence of vertical loading.

Recently, the numerical analyses are used as an efficient technique to solve the complex problem related to geotechnical engineering. The RPFEM has been applied in geotechnical engineering by Tamura et al. (1984, 1990) and Asaoka and Ohtsuka (1986, 1987, and 1990), and was further developed by Tamura et al. (1987) for friction material. In this method, the limit load is computed without the assumption of the potential failure mechanism. The RPFEM was originally developed based on the upper bound theorem in the limit analysis, but was shown to have been derived directly from the rigid plastic constitutive equation by Tamura et al. (1984). The advantage of the rigid plastic constitutive equation is that it can be extended and then applied to soils with more complicated material properties for the non-associated flow rule. In this study, the rigid plastic constitutive equation for the Drucker-Prager yield function is employed by the application of the penalty method. Hoshina et al. (2011) introduced a new constitutive equation for solid elements, to simulate the footing and the soil, and for interface elements, to simulate the interface plane between the footing and the soil. This method is based on the upper bound theorem in the limit analysis.

RPFEM was clearly shown to be effective to investigate the ultimate lateral resistance of the pile group and the ultimate bearing capacity of the footing under the complex loadings by being clarified the failure mechanism of them.

1.2 OBJECTIVES OF THE STUDY

For the pile group, the aim of this study is to estimate the ultimate lateral resistance of piles especially in terms of the group effect induced by the pile arrangement. The ultimate lateral resistance of pile groups was assessed by systematically varying the direction of the ground movement. Moreover, focuses is placed on the load bearing ratio of each pile against ground movement in various directions, in which the load bearing ratio is defined as the ratio of the ultimate lateral resistance of each pile in a pile group to that of a single pile, is an important design criterion, it was difficult to assess in past works. The ultimate lateral resistance is examined here for pile groups consisting of a 2x2 arrangement of four piles, as well as two piles, three piles, four piles, and an infinite number of piles arranged in a row through case studies in which the pile spacing is changed by applying the two-dimensional rigid plastic finite element method (RPFEM).

For the rigid footing under eccentric vertical load, the objective of this study is to estimate the ultimate bearing capacity of a footing against the eccentric load placed on two types of soil, namely, sandy soil and clayey soil, using a finite element analysis. The RPFEM is extended in this work to calculate not only the ultimate bearing capacity, but also the distribution of contact stress along the footing base. The study thoroughly investigates the effect of the eccentric vertical load on the ultimate bearing capacity in the normalized form of V/V_{ult} and e/B. The failure envelope in V-M plane is further investigated under various conditions for the sandy and clayey soils. This study examines the applicability of the failure envelope obtained for the eccentric vertical load to the cases where two variables, V and M, are independently prescribed.

For the rigid footing under eccentrically inclined load, the objective of this paper was to evaluate the bearing capacity of a rigid footing on the free surface of uniform sandy and clayey soils under the action of eccentric and inclined loadings. The footing was considered to be rigid and rough, as it most often is in reality. This study thoroughly considered the effect of the soil properties on load inclination factors i_γ and i_c in order to investigate the validity of the current design methods. In particular, the effects of the horizontal load in two directions on the ultimate bearing capacity of the footing and the failure envelopes in the V-H-M space were clarified, namely, positive and negative horizontal loads. Furthermore, the applicability of the limit load space to different computation conditions and independently prescribed moments was examined. Consequently, the failure envelope for each type of soil in the V-H-M space was

clearly seen to be unique.

For the rigid footing on sand overlying clay, the focus here is placed on an investigation of the bearing capacity and the failure mechanism of a rigid footing located on sand overlying clay by increasing thickness D and the internal friction angle ϕ of the sand layer for two extreme friction conditions, for which two cases are considered for the shear strength of the clay layer, namely, a weak layer and a stiff layer. Moreover, the study introduces a new equation based on the limit equilibrium condition of a rigid sand block during punching shear failure to determine the ultimate bearing capacity. The proposed equation provides results in close agreement with those given in the literature, while remaining simple and efficient enough to be used in practice.

1.3 THESIS OUTLINE

The present study focuses on the following main objective: 1) The assessment for Group effect on ultimate lateral resistance of piles against uniform ground movement; 2) Ultimate bearing capacity of rigid footing under eccentric vertical load; 3) Limit load space of rigid footing under eccentrically inclined load, and 4) Ultimate bearing capacity of rigid footing resting on sand layer over clay, with six chapters described as the follows:

Chapter 1 gives the general background of the ultimate lateral resistance of the pile group, the ultimate bearing capacity of the rigid footing, and objective of research work.

Chapter 2 gives the rigid plastic finite element method (RPFEM)

Chapter 3 is a chapter for group effect on ultimate lateral resistance of piles against uniform ground movement.

Chapter 4 is a chapter for ultimate bearing capacity of rigid footing under eccentric vertical load.

Chapter 5 is a chapter for limit load space of rigid footing under eccentrically inclined load.

Chapter 6 gives some areas requiring further work (ultimate bearing capacity of rigid footing resting on sand layer over clay)

References

Asaoka, A., and Ohtsuka, S., 1986. The analysis of failure of a normally consolidated clay foundation under embankment loading. Soils and Foundations. 26(2), 47-59.

Asaoka, A., and Ohtsuka, S., 1987. Bearing capacity analysis of a normally consolidated clay foundation. Soils and Foundations. 27(3), 58-70.

Asaoka, A., Ohtsuka, S., and Matsuo, M., 1990. Coupling analyses of limiting equilibrium state for normally consolidated and lightly overconsolidated soils. Soils and Foundations. 30(3), 109-123.

Bauer, J., Kempfert, H.-G., and Reul, O. (2016). Lateral pressure on piles due to horizontal soil movement. International Journal of Physical Modelling in Geotechnics, 16 (4), 173-184

Bransby, M.F. and Springman, S.M. (1999). Selection of load-transfer functions for passive lateral loading of pile groups. Computers and Geotechnics. 24 (3), 155-184.

Broms, B.B. (1964). Lateral Resistance of Piles in Cohesive Soils. Journal of the Soil Mechanics and Foundations Division. ASCE. 90 (2), 27-63.

Cox, W.R., Dixon, D.A. and Murphy, B.S. (1984). Lateral-Load Tests on 25.4mm (1-in.) Diameter Piles in Very Soft Clay in Side-by-Side and In-line Groups. Laterally Loaded Deep Foundations: Analysis and Performance. ASTM STP 835. Kansas City. Mo., 122-139.

Chen, L.T. (1994). Effect of lateral soil movements on pile foundation. PhD thesis, Univ. of Sydney, Sydney, Australia.

Chen, L.T. and Poulos, H.G. (1996). The behavior of piles subjected to lateral soil movements. Res. Rep. No. 731, Univ. of Sydney, Sydney, Australia.

Chen, L.T. and Poulos, H.G. (1997). Piles Subjected to Lateral Soil Movements. J. Geotech. Geotech. Eng. ASCE. 123 (9), 802-811.

Chen, L.T., Poulos, H.G. and Hull, T.S. (1997). Model test on pile groups subjected to lateral soil movement. Soils and Foundations. 37 (1), 1-12.

Goh, A. T. C., Tech, C.I. and Wong, K. S. (1997). Analysis of piles subjected to embankment induced lateral soil movements. Journal of Geotechnical and Geoenvironmental Engineering. ASCE. 123 (9), 792-801.

Gourvenec, S., 2008. Effect of embedment on the undrained capacity of shallow foundations under general loading. Géotechnique. 58(3), 177-186.

Hansen, J. B. 1961. A general formula for bearing capacity. Danish Geotechnical Institute, Bulletin No. 11, 38-46.

Hansen, J. B. 1970. A revised and extended formula for bearing capacity. Danish Geotechnical Institute, Bulletin No. 28, 5-11.

Hoshina, T., Ohtsuka, S., and Isobe, K., 2011. Rigid plastic analysis for slope including thin weak layer. Geotechnical Journal. 6, 191-200 (in Japanese).

Khitas, N.E.H., Benmeddour, D., Mellas, M. and Mabrouki, A., 2017. The undrained bearing capacity of strip footings under eccentric loading: effect of soil-footing interface tensile strength. International Journal of Geotechnical Engineering. 1-7.

Krabbenhoft, S., Damkilde, L., and Krabbenhoft, K. 2013. Bearing capacity of strip footings in cohesionless soil subject to eccentric and inclined loads. International Journal of Geomechanics, 14(3), 04014003.

Loukidis, D., Chakraborty, T. and Salgado, R., 2008. Bearing capacity of strip footings on purely frictional soil under eccentric and inclined loads. Canadian Geotechnical Journal. 45(6), 768-787.

Meyerhof, G.G., 1953. The bearing capacity of foundations under eccentric and inclined loads. In Proc. of the 3rd Int. Conf. on SMFE (Vol. 1, 440-445).

Meyerhof, G. G., 1963. Some recent research on the bearing capacity of foundations. Canadian Geotechnical Journal. 1(1), 16-26.

Llyas, T., Leung, C.F., Chow, Y.K. and Budi, S.S. (2004). Centrifuge Model Study of Laterally Loaded Pile Groups in Clay. J. Geotech. Geoenviron. Eng. ASCE. 130 (3), 274-283.

Miao, L. (2005). Effects of lateral soil movements on piles. Ph.D. Thesis, Nanyang Technological University.

Miao, L.F., Goh A.T.C., Wong, K.S., and Teh, C.I. (2008). Ultimate soil pressure for pile groups in soft clay subjected to lateral soil movements. DFI Journal: The Journal of the Deep Foundations Institute 2(1): 42-51.

Pan, J. L. (1998). Experimental and numerical study of the behavior of piles subjected to lateral soil movement. Ph.D. Thesis, Nanyang Technological University.

Pan, J.L., Goh, A. T. C., Wong, K.S. and Teh, C. I. (2002). Ultimate soil pressures for piles subjected to lateral soil movements. Journal of Geotechnical and Geonvironmental Engineering. ASCE. 128 (6), 530-535.

Shen, Z., Feng, X., and Gourvenec, S., 2016. Undrained capacity of surface foundations with zero-tension interface under planar V-H-M loading. Computers and Geotechnics. 73, 47-57.

Stewart, D. P. (1992). Lateral loading of piled bridge abutments due to embankment construction. Ph.D. Thesis, The University of Western Australia.

Tamura, T., Kobayashi, S. and Sumi, T. (1984). Limit analysis of soil structure by rigid plastic finite element method. Soils and Foundations. 24 (1), 34-42.

Tamura, T., Kobayashi, S. and Sumi, T. (1987). Rigid Plastic Finite Element Method for Frictional Materials. Soils and Foundations. 27 (3), 1-12.

Tamura, T., Kobayashi, S. and Sumi, T. (1990). Rigid Plastic Finite Element Method in Geotechnical Engineering Computational. Current Japanese Material Research, 15-23.

Terzaghi, K., 1943. Theoretical soil mechanics. Wiley, New York.

Vesic, A. S. 1973. Analysis of ultimate loads of shallow foundations. Journal of Soil Mechanics and Foundations Division, ASCE, 99(1), 45-73.

Vesic, A.S. 1975. Bearing capacity of shallow foundations. In Foundation engineering handbook. Edited by H.F. Winterkorn and H.-Y. Fang. Van Nostrand Reinhold, New York, 121-147.

Chapter 2
RIGID PLASTIC FINITE ELEMENT METHOD

2.1 INTRODUCTION

Numerical analysis is powerful mathematical tool which is possible to solve any engineering problems. The finite element method (FEM) is widely employed as one of the well-established technique to solve complex problems in various fields of civil engineering applications, for both the research and the design of real engineering problems. In geotechnical engineering, FEM has been applied to estimate the ultimate lateral resistance of pile group such as Stewart (1992), Chen (1994), Chen and Poulos (1997) and Goh et al. (1997), estimate the ultimate bearing capacity such as Sloan and Randolph (1982), Georgiadis and Butterfield (1988) and Gottardi and Buterfield (1993), ect. Rigid plastic finite element method has been employed in geotechnical engineering by Tamura et al. (1984, 1987, 1980), Asaoka and Ohtsuka (1986, 1987) and Asaoka et al. (1990). The method is originally developed based on the upper bound theorem in the limit analysis, but was shown to have been derived directly from the rigid plastic constitutive equation by Tamura et al. (1984). The advantage of the rigid plastic constitutive equation is that it can be extend and then applied to soils with more complicated material properties for the non-associated flow rule. In this study, the rigid plastic constitutive equation for Drucker-Prager yield function is employed by the application of the penalty method. Hoshina et al. (2011), Komura et al. (2016) developed the rigid plastic constitutive equation by introducing the dilatancy condition that is explicity modeled through the use of the penalty method. The limit load is obtained by introducing the constraint condition for external work into the equilibrium equation using the penalty method in the same way. Since the penalty method incorporates the constraint condition directly into the governing equation, high computation efficiency can be achieved.

2.2 RIGID PLASTIC CONSTITUTIVE EQUATION FOR FINITE ELEMENT METHOD

2.2.1 Rigid plastic constitutive equation for solid elements

Tamura et al. (1987) developed the rigid plastic constitutive equation for frictional material. This study

employs the rigid plastic constitutive equation based on his derivation. The Drucker-Prager yield function is expressed as follows:

$$f(\boldsymbol{\sigma}) = aI_1 + \sqrt{J_2} - b = 0 \tag{1}$$

where, I_1 is the first invariant of stress σ_{ij}, and $I_1 = tr(\sigma_{ij})$ for which the extension stress is defined as positive.

J_2 is the second invariant of deviator stress s_{ij}, defined as $J_2 = \dfrac{1}{2} s_{ij} s_{ij}$, and coefficients $a = \dfrac{\tan\phi}{\sqrt{9 + 12\tan^2\phi}}$

and $b = \dfrac{3c}{\sqrt{9 + 12\tan^2\phi}}$ are the material constants corresponding to the shear resistance angle and cohesion,

respectively, under the plane strain condition. Strain rate $\dot{\varepsilon}$, which is a purely plastic component, should satisfy the volumetric constraint condition on the dilation property of the soil, as follows:

$$h(\dot{\boldsymbol{\varepsilon}}) = \dot{\varepsilon}_v - \frac{3a}{\sqrt{3a^2 + \dfrac{1}{2}}} \dot{e} = \dot{\varepsilon}_v - \eta\dot{e} = 0 \tag{2}$$

where, $\dot{\varepsilon}_v$ and $\dot{e}$ indicate the volumetric strain rate and the norm of the strain rate, respectively.

Parameter η is defined in Eq. (2). The stress vector is shown by two component stresses of which the first stress of, $\boldsymbol{\sigma}^{(1)}$, uniquely determines the yield function, and the second stress, $\boldsymbol{\sigma}^{(2)}$, expresses indeterminate stress parameter β, which remains unknown until the boundary value problem given by Eq. (2) is solved.

$$\boldsymbol{\sigma}^{(1)} = \lambda\frac{\partial f}{\partial \boldsymbol{\sigma}} = \frac{b}{\sqrt{3a^2 + \dfrac{1}{2}}} \frac{\dot{\boldsymbol{\varepsilon}}}{\dot{e}} \tag{3}$$

$$\boldsymbol{\sigma}^{(2)} = \beta\frac{\partial h}{\partial \dot{\boldsymbol{\varepsilon}}} = \beta\left(\boldsymbol{I} - \frac{3a}{\sqrt{3a^2 + \dfrac{1}{2}}} \frac{\dot{\boldsymbol{\varepsilon}}}{\dot{e}} \right) \tag{4}$$

The rigid plastic constitutive equation is expressed by the Lagragian method after Tamura (1991), as follows:

$$\boldsymbol{\sigma} = \boldsymbol{\sigma}^{(1)} + \boldsymbol{\sigma}^{(2)} = \frac{b}{\sqrt{3a^2 + \dfrac{1}{2}}} \frac{\dot{\boldsymbol{\varepsilon}}}{\dot{e}} + \beta\left(\boldsymbol{I} - \frac{3a}{\sqrt{3a^2 + \dfrac{1}{2}}} \frac{\dot{\boldsymbol{\varepsilon}}}{\dot{e}} \right) \tag{5}$$

Hoshina et al. derived the constitutive equation by introducing the constraint condition on the strain rate

directly into the constitutive equation with the use of the penalty method (Hoshina et al. (2011); Nguyen et al. (2016); and Pham et al. (2019a, 2019b, 2020). The stress-strain rate relation for the Drucker-Prager yield function is expressed as follows:

$$\boldsymbol{\sigma} = \frac{b}{\sqrt{3a^2 + \frac{1}{2}}} \frac{\dot{\boldsymbol{\varepsilon}}}{\dot{e}} + \kappa\left(\dot{\varepsilon}_v - \eta\dot{e}\right)\left(\boldsymbol{I} - \frac{3a}{\sqrt{3a^2 + \frac{1}{2}}} \frac{\dot{\boldsymbol{\varepsilon}}}{\dot{e}}\right)$$

(6)

where κ is a penalty constant. The FEM, together with this constitutive equation, provides an equivalent equation for the upper bound theorem in plasticity; the method is called the RPFEM in this study. It is a noted property of this constitutive equation that the relationship between stress and the strain rate is specified. The norm of the strain rate is substantially indeterminate since focus is placed on the limit state of the structure. Stress is determined for the normalized strain rate using its norm in order to determine the limit load coefficient for the prescribed load. Hoshina et al. (2011) introduced the constraint condition on external work into the equilibrium equation by using the penalty method. They reported that more rational results were obtained by the developed method than by methods in previous works. The use of the penalty method is advantageous in that it can shorten the computation time and lead to stable computational results. Since this study focuses on cohesive soils, as mentioned above, the constitutive equation is limited to the von Mises yield function where the soil composing the ground exhibits plastically incompressible deformations. The rigid plastic constitutive equation is simple and effective for assessing the limit state of the ground due to the advantage of not using an uncertain elastic modulus for the ground.

2.2.2 Rigid plastic constitutive equation for contact plane

At the contact plane where the displacement velocity is discontinuous, the stress at the limit state is expressed by the following Coulomb yield function:

$$f(\mathbf{t}) = |t_s| - c_s + t_n \tan\phi_s$$

(7)

where, t_s and t_n are the shear and normal components of the stress vector at the contact plane. ϕ_s and c_s are the material parameters corresponding to the internal friction angle and the cohesion at the contact plane

In the present analysis, an interface element of zero thickness is introduced into the contact plane between two bodies, as seen in **Fig. 1.1(a)**. $\Delta \dot{\mathbf{u}}$ is the vector of the relative displacement velocity at the discontinuous line of displacement velocity, and $\Delta \dot{\mathbf{u}} = \dot{\mathbf{u}}^+ - \dot{\mathbf{u}}^-$ is shown in **Fig. 1.1(b)**.

(a) Stress conditions on interface surface   (b) Line of motion on interface surface
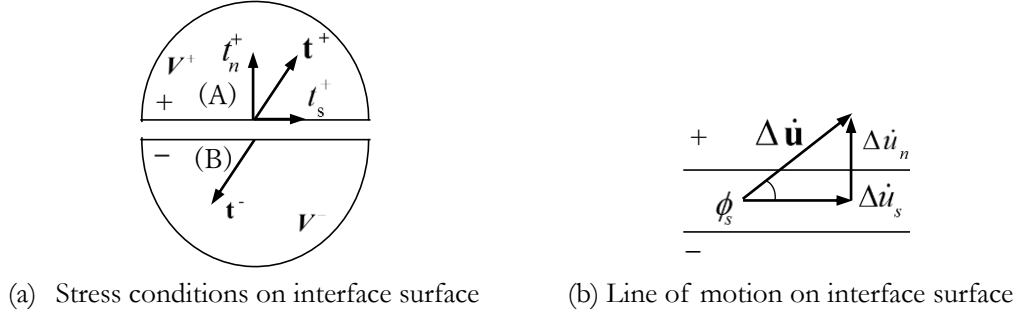
Figure 1.1 Stress vector and vector of relative displacement velocity.

The volumetric constraint condition for the Coulomb yield function is expressed as follows:

$$h\left(\Delta \dot{\mathbf{u}}\right) = \left|\Delta \dot{u}_s\right| \tan\phi_s - \Delta \dot{u}_n = \left(\frac{\Delta u_s}{\left|\Delta u_s\right|} \cdot \tan\phi_s - 1\right)\left(\begin{array}{c} \Delta \dot{u}_s \\ \Delta \dot{u}_n \end{array}\right) = \mathbf{a} \cdot \Delta \dot{\mathbf{u}} = 0 \tag{8}$$

where, $\Delta \dot{u}_n$ is a component of the relative displacement velocity normal to the discontinuous line and $\Delta \dot{u}_s$ is a tangential component. The stress vector is divided into the stress of $\mathbf{t}^{(1)}$, determined for the yield function, and the indeterminate stress of $\mathbf{t}^{(2)}$ in the same way as that for the volumetric constraint condition of the solid element. The following equation is derived for the interface element:

$$\mathbf{t}^{(1)} = \gamma_s \frac{\partial f}{\partial \mathbf{t}} = \frac{c_s}{\cos\phi_s \left(1 + \tan^2\phi_s\right)} \frac{\Delta \dot{\mathbf{u}}}{\left\|\Delta \dot{\mathbf{u}}\right\|} \tag{9}$$

$$\mathbf{t}^{(2)} = \omega_s \frac{\partial h}{\partial \Delta \dot{\mathbf{u}}} = \omega_s \mathbf{a} \tag{10}$$

where, ω_s is the indeterminate stress parameter; it is determined by solving the boundary value problem with Eq. (8) by directly considering the volumetric constraint condition with a penalty constant, ξ. The stress and relative displacement velocity relation for the interface element is expressed as follows:

$$\mathbf{t} = \mathbf{t}^{(1)} + \mathbf{t}^{(2)} = \frac{c_s}{\cos\phi_s \left(1 + \tan^2\phi_s\right)} \frac{\Delta \dot{\mathbf{u}}}{\left\|\Delta \dot{\mathbf{u}}\right\|} + \xi\left(\mathbf{a} \cdot \Delta \dot{\mathbf{u}}\right)\mathbf{a} \tag{11}$$

2.3 CONCLUSIONS.

RPFEM was clearly shown to be effective to investigate the ultimate lateral resistance of the pile group

and the ultimate bearing capacity of the footing under the complex loadings by being clarified the failure mechanism of them.

Moreover, the applicability of the rigid plastic constitutive equation to the assessment of the ultimate bearing capacity is examined from the viewpoints of the interaction between the footing and the soil and the failure mechanism of the footing-soil system.

References.

Asaoka, A., and Ohtsuka, S., 1986. The analysis of failure of a normally consolidated clay foundation under embankment loading. Soils and Foundations. 26(2), 47-59.

Asaoka, A., and Ohtsuka, S., 1987. Bearing capacity analysis of a normally consolidated clay foundation. Soils and Foundations. 27(3), 58-70.

Asaoka, A., Ohtsuka, S., and Matsuo, M., 1990. Coupling analyses of limiting equilibrium state for normally consolidated and lightly overconsolidated soils. Soils and Foundations. 30(3), 109-123.

Chen, L.T. (1994). Effect of lateral soil movements on pile foundation. PhD thesis, Univ. of Sydney, Sydney, Australia.

Chen, L.T. and Poulos, H.G. (1996). The behavior of piles subjected to lateral soil movements. Res. Rep. No. 731, Univ. of Sydney, Sydney, Australia.

Chen, L.T. and Poulos, H.G. (1997). Piles Subjected to Lateral Soil Movements. J. Geotech. Geotech. Eng. ASCE. 123 (9), 802-811.

Georgiadis, M., and Butterfield, R., 1988. Displacements of footings on sand under eccentric and inclined loads. Canadian Geotechnical Journal. 25(2), 199-212.

Gottardi, G., and Butterfield, R., 1993. On the bearing capacity of surface footings on sand under general planar loads. Soils and Foundations. 33(3), 68-79.

Goh, A. T. C., Tech, C.I. and Wong, K. S. (1997). Analysis of piles subjected to embankment induced lateral soil movements. Journal of Geotechnical and Geoenvironmental Engineering. ASCE. 123 (9), 792-801.

Hoshina, T., Ohtsuka, S. and Isobe, K. (2011). Ultimate bearing capacity of ground by rigid plastic finite element method taking account of stress dependent non-linear strength property. Journal of Applied Mechanics. 6, 191-200. (in Japanese)

Komura, S., Shiratori, Y., Ohtsuka, S. and Hoshina, T. (2016). Discussion on ultimate lateral resistance of pile in clayey ground during earthquake. Society of Civil Engineering. 72 (2), 48-61. (in Japanese)

Nguyen, Du L., Ohtsuka, S., Hoshina, T. and Isobe, K. (2016). Discussion on size effect of footing in ultimate bearing capacity of sandy soil using rigid plastic finite element method. Soils and Foundations. 56 (1), 93-103.

Stewart, D. P. (1992). Lateral loading of piled bridge abutments due to embankment construction. Ph.D. Thesis, The University of Western Australia.

Pham, Q. N., Ohtsuka, S., Isobe, K., & Fukumoto, Y (2019a). Group effect on ultimate lateral resistance of piles against uniform ground movement. Soils and Found. 59(1): 27-40.

Pham, Q. N., Ohtsuka, S., Isobe, K., Fukumoto, Y., & Hoshina, T (2019b). Ultimate bearing capacity of rigid footing under eccentric vertical load. Soils and Found. 59(6): 1980-1991.

Pham, Q. N., Ohtsuka, S., Isobe, K., & Fukumoto, Y (2020). Limit load space of rigid footing under eccentrically inclined load. Soils and Found. Accepted (Article in press).

Tamura, T., Kobayashi, S. and Sumi, T., 1984. Limit analysis of soil structure by rigid plastic finite element method. Soils and Foundations. 24 (1), 34-42.

Tamura, T., Kobayashi, S. and Sumi, T., 1987. Rigid Plastic Finite Element Method for Frictional Materials. Soils and Foundations. 27 (3), 1-12.

Tamura, T., Kobayashi, S. and Sumi, T., 1990. Rigid Plastic Finite Element Method in Geotechnical Engineering Computational. Current Japanese Material Research. 15-23.

Chapter 3

GROUP EFFECT ON ULTIMATE LATERAL RESISTANCE OF PILES AGAINST UNIFORM GROUND MOVEMENT

3.1 INTRODUCTION

When an earthquake occurs, piles installed in the ground are laterally loaded due to the ground displacement caused by the earthquake's vibrations. Thus, it is important to design piles in such a way that they will remain safe during earthquakes. For this purpose, it is necessary to assess the magnitude of the load that will be applied to the piles during an earthquake. This load is usually assessed by a spring model using the lateral ground displacement recorded during past earthquakes. Recently, however, due to the development of highly sensitive sensors and systems to measure an earthquake's vibrations, the measured maximum acceleration is becoming larger every year and earthquake records must be updated to reflect these changes. This situation causes an increase in the cost of constructing pile foundations; and thus, more economical and suitable design methods are being intensively sought. When the ground displacement is large, rather than occurring together with the piles, the deformation of the ground leads the ground movement to pass around the piles. Therefore, it is natural that a bi-linear spring model is introduced to assess the load applied to the piles. The ultimate load applied to the piles is computed for the limit state where the ground displacement passes through the piles. In this study, the ultimate load is described as the ultimate lateral resistance of the piles. For most pile problems, the lateral resistance of the piles is usually assessed along the longitudinal direction of the piles. This study, however, concentrates on the cross section of the piles so that a two-dimensional analysis can be conducted. Since earthquakes take place in short periods of time, the ground deforms under an undrained condition. Thus, the ground is usually modeled by cohesive material. In this study, focus is placed on clayey soils, since the displacement of clayey soils is generally observed to be greater during an earthquake. However, focus is sometimes placed on sandy soils when the ground has been liquefied by an earthquake. It is widely known that liquefied sandy soil causes great lateral deformation. The physical properties of liquefied sandy soil are not clear; and therefore, the

material is often assumed cohesive in the design.

In pile-soil systems, the ultimate lateral resistance of the piles depends exclusively on the pile-soil adhesion. Although the pile-soil adhesion depends on the pile material (concrete, steel or wood), it has been modeled under two extreme conditions, namely, either perfectly smooth or perfectly rough. This study models the adhesion under the perfectly rough condition from the conservative viewpoint. To investigate the resistance of laterally loaded single piles, several empirical and theoretical investigations have been performed to analyze the ultimate lateral resistance of single piles, such as those by Broms (1964) and Randolph and Houlsby (1984). In these works, the ultimate lateral resistance of the piles was compared to the prescribed load applied to the piles. Broms (1964) studied the slip line method to calculate the ultimate lateral resistance of single piles driven into cohesive soil. They reported lateral resistance in the range of 8.28 c_u-12.56 c_u for various piles with circular and rectangular shapes and with smooth and rough surfaces, in which c_u was the undrained shear strength of the ground. A solution was provided for all pile surface conditions, and the shapes of the slip lines around the piles were predicted. Randolph and Houlsby (1984) used two-dimensional lower-bound and upper-bound limit analyses to provide the collapse load for circular piles in cohesive soil. The ultimate lateral resistance of the piles was in the range of 9.14 c_u for perfectly smooth piles to 11.94 c_u for perfectly rough piles. However, more complex problems arise for pile groups because the ultimate lateral resistance of each pile is different among all the piles in a pile group due to the pile-soil interaction effect. The group effect on the ultimate lateral resistance has been investigated by several researchers using numerical analyses and model tests. Stewart (1992), Chen (1994), Chen and Poulos (1997), and Goh et al. (1997) used numerical analyses to calculate the ultimate lateral resistance of pile groups against horizontal ground movement. The analyses showed that the ultimate lateral resistance of a pile in a pile group was generally lower than that of a single pile due to the pile-soil interaction. The same results were also obtained in model tests conducted by Cox et al. (1984), Chen and Poulos et al. (1997), Pan (1998), Pan et al. (2002), Llyas et al. (2004), Miao (2005), Miao et al. (2008), and Bauer et al. (2016). In recent years, several researchers have reported the group effect on the ultimate lateral resistance using numerical analyses, such as Georgiadis et al. (2013a, 2013b. 2013c) and Zhao et al. (2017a, 2017b). However, most of the previous studies involved the analysis of the limit load for the prescribed load applied to the piles. That is, since the load being applied to each pile in a pile group was not known prior to analysis, the past works

were focused on the ultimate lateral resistance of single piles. The ultimate lateral resistance of a pile group is affected by many factors, such as the pile spacing, the number of piles, and the direction of the ground movement against the pile arrangement.

In this study, the pile-soil system is simulated by employing a rigid plastic finite element analysis based on the upper bound theorem. The rigid plastic finite element method (RPFEM) has been applied in geotechnical engineering by Tamura et al. (1984, 1990) and was further developed by Tamura et al. (1987) for frictional material. In this method, the limit load is computed without the assumption of the potential failure mechanism. The method is effective for computing the ultimate lateral resistance of pile groups against horizontal ground movement in clayey soils. The RPFEM was originally developed based on the upper bound theorem in the limit analysis, but was shown to have been derived directly from the rigid plastic constitutive equation by Tamura et al. (1984). The advantage of the rigid plastic constitutive equation is that it can be extended and then applied to soils with more complicated material properties for the non-associated flow rule. In this study, the rigid plastic constitutive equation for the Drucker-Prager yield function is employed by the application of the penalty method. Hoshina et al. (2011), Komura et al. (2016), and Nguyen et al. (2016) developed the rigid plastic constitutive equation by introducing the dilatancy condition that is explicitly modeled through the use of the penalty method. The limit load is obtained by introducing the constraint condition for external work into the equilibrium equation using the penalty method in the same way. Since the penalty method incorporates the constraint condition directly into the governing equation, high computational efficiency can be achieved.

Only a few studies have considered the effect of the loading direction on the ultimate lateral resistance of pile groups, such as the numerical analyses of Georgiadis et al. (2013), Zhao et al. (2017) and the model tests of Kashiwa et al. (2007) and Su et al. (2015). However, Georgiadis et al. (2013), Zhao et al. (2017) provided the total ultimate resistance of the pile group, rather than the ultimate reaction of each pile in the group subjected to horizontal ground movement. In this study, the effect of the direction of the ground movement and the pile arrangement on the ultimate lateral resistance of pile groups and the load bearing ratio of each pile is investigated. Pile groups consisting of a 2x2 arrangement of four piles, as well as two piles, three piles, four piles, and an infinite number of piles arranged in a row are intensively investigated by changing the pile spacing.

3.2 ANALYSIS OF BOUNDARY CONDITIONS OF MODEL UNDER PLANE STRAIN CONDITION

As was mentioned as the object of this study in the Introduction, although the lateral resistance of the pile is exerted along the longitudinal direction of the pile which increases with depth from a minimum value at the ground surface to a maximum value at a certain critical depth and remains constant up to the bottom part of the pile. This study introduces a two-dimensional model to analyze the behavior of the ground surrounding the pile. It treats the pile-soil interaction below the critical depth which indicates the threshold value where the failure mode of the ground changes from three-dimensional to two-dimensional behavior. The study newly defines the boundary conditions for the assessment of the ultimate lateral resistance of pile groups. **Figures 3.1(a**) and **(b)** show two ways to simulate the pile-soil system with different boundary conditions. One way is to assess the reaction force at the limit state by applying a uniform velocity field to the pile, while the other way is to assess the ultimate lateral resistance by applying a load to the pile. To survey the ultimate lateral resistance of a pile group, the model in **Figure 3.1(a)** is necessary for the computation in consideration of the piles-soil interaction which is unknown prior to the analysis. **Figure 3.1(a)** shows the typical finite element mesh and the first boundary condition of the single piles used in the analysis. A mesh with approximately 4000 four-node iso-parametric rectangular elements was used to model the piles and the soil surrounding the piles. A finer density mesh was employed around the piles. Each pile was modeled as a solid element and the strength of the pile was set to be higher than that of the soil in order to simulate a rigid pile. The soil and the piles were modeled as rigid perfectly plastic material with the following properties: the undrained shear strength of the soil was c_u=100 kPa and the internal friction angle of the soil was ϕ=0°, while the shear strength of the pile material was c_p=50000 kPa and the internal friction angle of the piles was ϕ=0°. Analyses were performed for a pile diameter of D=0.6 m. In particular, higher strength elements were employed for the outer boundary elements in order to simulate the homogeneous ground movement at the boundary elements. A uniform distributed load was applied at all nodes of the rigid outer boundary elements to define the prescribed load and the load coefficient. The ultimate lateral resistance was assessed by computing the limit value for this load coefficient. The center of each pile was set as the fixed velocity boundary condition and the reaction of the piles was computed to analyze the load bearing ratio. The two boundary surfaces, parallel to the direction of the ground movement, were set as the

slider condition. The distance from the center of a pile to all four boundary surfaces was basically set to be far away in order to avoid the effect of the boundary conditions on the failure mode of the ground around the pile; it was set at more than 10.0 D in all analyses. **Figure 3.1(b)** shows the second boundary condition for directly applying the load on the pile, as was seen in past works. While the center of each pile was set to be under the free condition, the four boundary surfaces were set to be under the fixed condition. The analysis was performed by applying a uniformly distributed load on all nodes of the pile diameter.

(a)   (b)
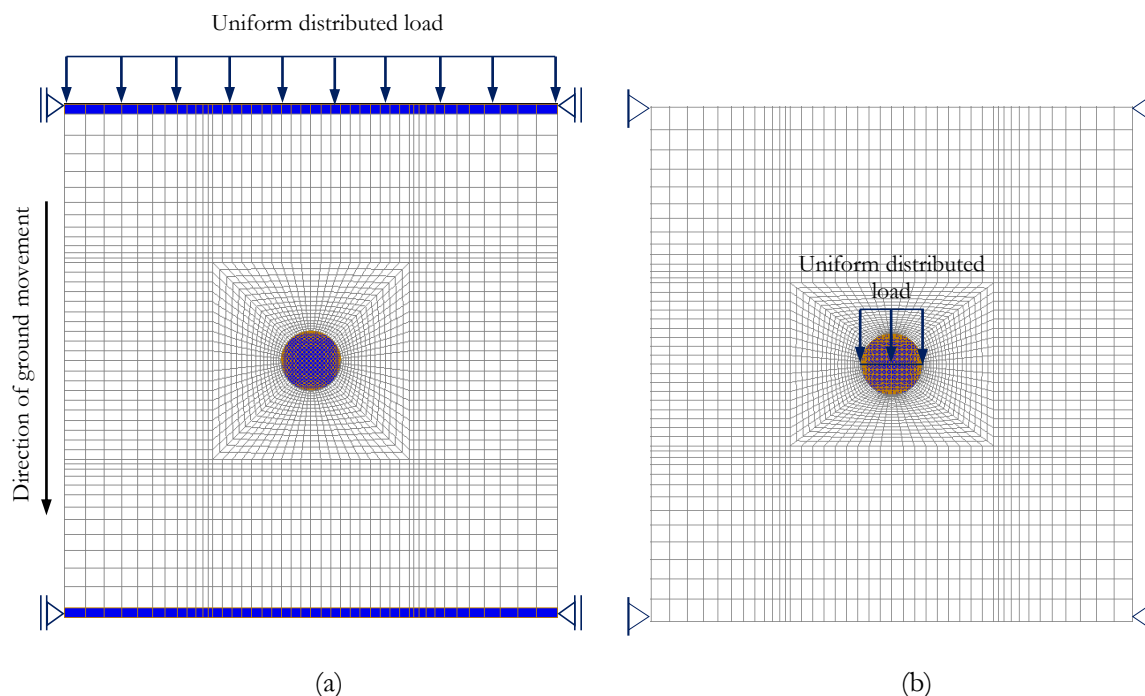
Figure 3.1. Typical finite element mesh and two boundary conditions of single pile for RPFEM

The ultimate lateral resistance of the pile was generally obtained as a value close to 12.27 c_u for model (a) and 12.30 c_u for model (b), in which the total resistance is normalized by the length of the pile diameter. As a result, since the setting of the shear strength and the pile diameter does not affect the ultimate lateral resistance, the ultimate lateral resistance is shown irrespective of them. The results obtained for the strain rate distribution for a single pile are shown in **Fig. 3.2.** The norm of the strain rate presented contour lines in the range of $\dot{e}_{max} \sim \dot{e}_{min} (=0)$. The distribution of $\dot{e}$ shows the failure mode of the ground and reflects the pile-soil interaction effect. **Figure 3.2** shows the failure modes of a single pile under both boundary conditions. The failure zone of the ground around the pile is observed in the range of 1.5 D-2.0 D from the center of the pile and is the same as the slip line described in Broms (1964), Georgiadis et al. (2013a,

2013b, 2013c), and Zhao et al. (2017a, 2017b). The obtained ultimate lateral resistance of a single pile against the horizontal ground movement was as 12.27 c_u for the perfectly rough pile condition, which is similar to the value of 11.95 c_u reported by Georgiadis et al. (2013a, 2013b, 2013c). The difference may be caused by the fact that they employed different models, namely, the soil and the pile were modeled as linear elastic-perfectly plastic and linear elastic materials in their work. The ultimate lateral resistance of a single pile was also computed by the RPFEM in the same way as in past works in which the pull-out force was directly applied to the pile, as shown in **Fig. 3.2(b)**. The obtained value was found to coincide with that of the problem defined in **Fig. 3.1(a)**. This indicates that the method proposed for assessing the ultimate lateral resistance of piles is rational and accurate. In addition, the method provides a load bearing ratio for each pile in the pile group against the homogenous ground movement. The upper bound method tends to overestimate the limit value even though an optimization is conducted. Basically, it is difficult to judge the magnitude of an exact solution; however, the results obtained here have apparently proven it to be almost the same as that in past works.

p_u=12.27 c_u　　　　　　　　p_u=12.30 c_u

(a)　　　　　　　　　　　　(b)
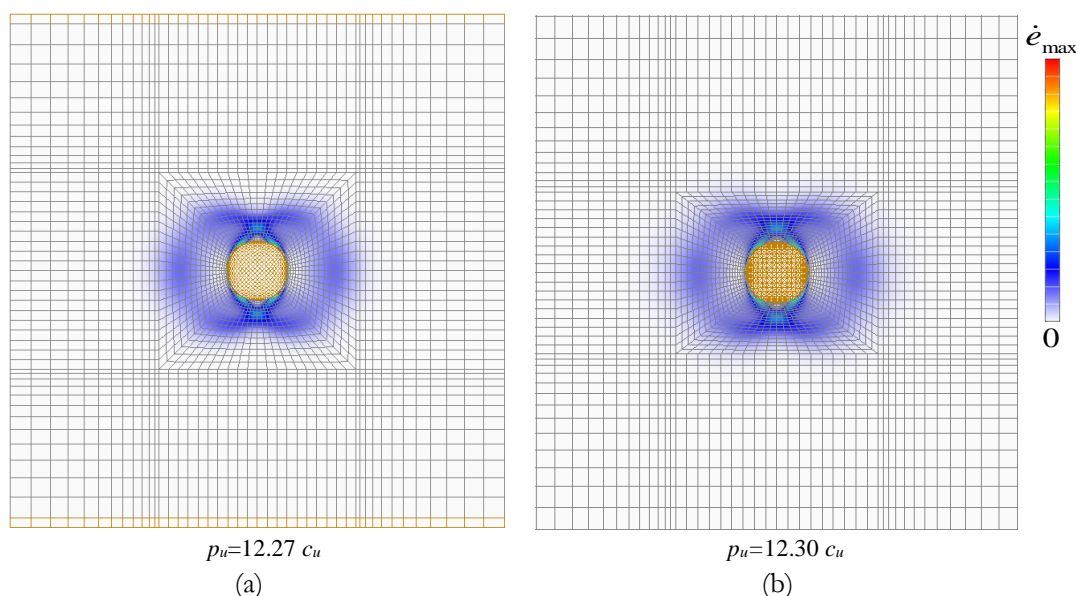
Figure 3.2. Failure modes of single pile in two models

3.3 ULTIMATE LATERAL RESISTANCE OF 2x2 PILE GROUP

3.3.1 Group effect on ultimate lateral resistance

In practice, piles are often employed in a group and the performance of the piles is influenced by the pile-soil interaction. Therefore, to survey the group effect, the ultimate lateral resistance of a 2x2 pile group

in clayey soil was investigated in this study. The ultimate lateral resistance was systematically computed for changes in the pile spacing where the spacing, s, is the distance between the centers of two piles. When the four piles and the intermediate ground between the piles form a rigid body, the ultimate lateral resistance of the 2x2 pile group can be compared with that of a square pile. A numerical simulation was conducted for horizontal ground movement by fixing the pile spacing from 1.5 D to 6.0 D, in which D is the outside diameter of a single pile. The size of the square pile L was adjusted to have the same outer perimeter as a pile group and $L=s+D$.
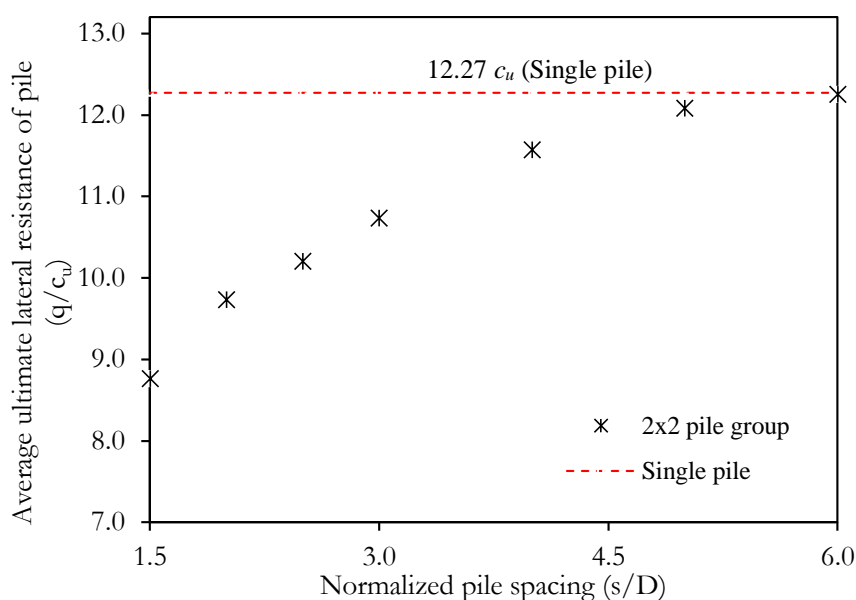
Figure 3.3. Average ultimate lateral resistance of pile in 2x2 pile group.

Figure 3.3 shows the variation of the average ultimate lateral resistance of pile in 2x2 pile group with the normalized pile spacing s/D, in which the average ultimate lateral resistance (q/c_u) of piles is expressed as q/c_u to indicate the normalized value by the undrained shear strength of clay c_u. The average ultimate lateral resistance q (kN/m²) is subsequently calculated by dividing the total ultimate lateral reaction force Q (kN/m) by the pile diameter and the number of piles. The average ultimate lateral resistance of pile tends to increase with an increasing pile spacing and coincides with the ultimate lateral resistance of 12.27 c_u the isolated single pile at a sufficiently large pile spacing. This trend was found to have been caused by the difference in the failure modes of the ground peripheral of the piles, as seen in **Fig. 3.4**. The failure mode

of the ground around the piles apparently changed as the pile spacing increased from 1.5 D to 6.0 D.
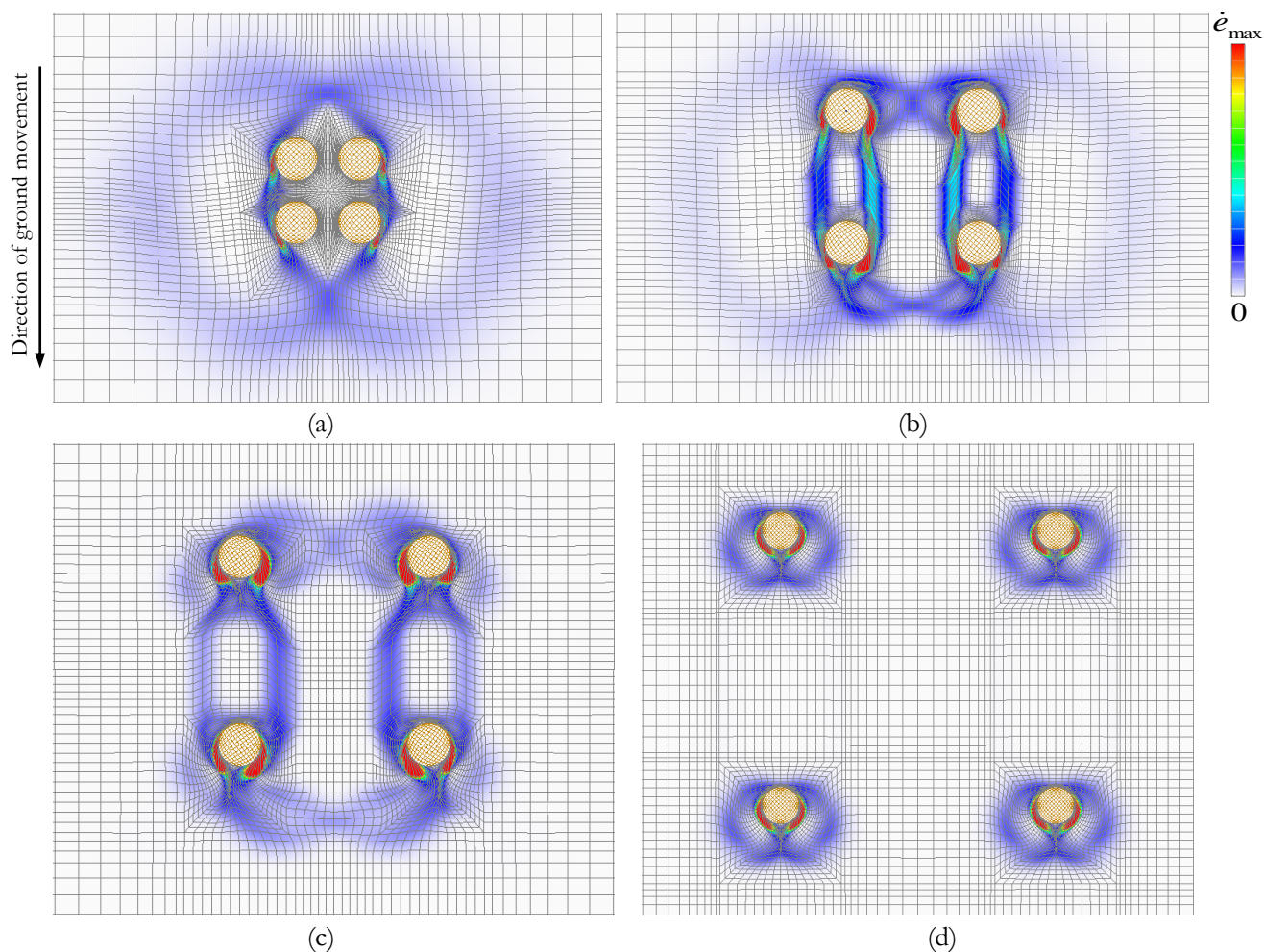
Figure 3.4. Deformation diagrams of 2x2 pile group: (a) s/D=1.5, (b) s/D=3.0, (c) s/D=4.5, and (d) s/D=6.0 in direction of 90 degrees.

The results obtained for the strain rate distribution of the two models with a normalized pile spacing s/D=1.5 and a normalized pile width L/D=2.5 are shown in **Fig. 3.5.** The figure expresses the failure modes of both the pile group in case of s/D=1.5 and the square pile corresponding to pile group. The total ultimate lateral reaction force of two models was obtained to almost coincide each other, namely, 2126 (kN/m) and 2167 (kN/m), respectively. This is because in the case of a normalized pile spacing s/D=1.5, the ground between the piles did not undergo any plastic deformation due to the support of the piles, as shown in **Fig. 3.5(a)**. Four different failure modes of the ground around the 2x2 pile group are indicated in **Figs. 3.4(a)**, **3.4(b)**, **3.4(c)**, and **3.4(d)** for normalized pile spacing s/D=1.5, 3.0, 4.5, and 6.0, respectively.

It is noted that all figures only present the ground around the piles in order to focus the failure mode of the ground, despite the wider ground area was analyzed to avoid the effect of the boundary condition. They express the deformation of the ground by multiplying the arbitrary time by the obtained nodal velocity in order to clearly indicate each failure mode. The illustrated deformation expresses the failure mode at the limit state. With an increase in pile spacing, the failure mode of the ground is found to change. At a smaller pile spacing, two pile lines form a rigid block and the intermediate ground between the two pile lines passes through the piles along the two pile lines. The detailed failure mode of the intermediate ground reflects the pile spacing even though the failure modes seem similar. Finally, when the pile spacing reaches 6.0 D, no group effect can be observed, as shown in **Fig. 3.4(d).**

Q=2126 kN/m
(a)

Q=2167 kN/m
(b)
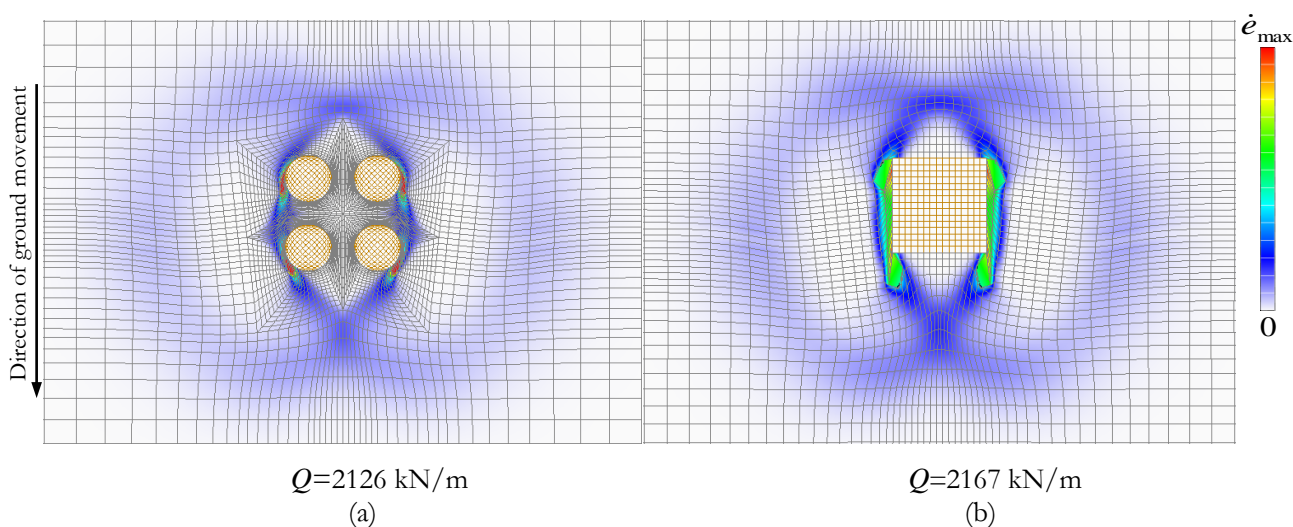
Figure 3.5. a) Deformation diagrams of 2x2 pile group with normalized pile spacing s/D=1.5 in case of 90deg

b) Deformation diagram of square pile with normalized pile width L/D=2.5

(In computation D=0.6m was employed)

3.3.2 Effect of direction of ground movement on ultimate lateral resistance

Georgiadis et al. (2013) and Zhao et al. (2017) investigated the effect of the loading direction on the ultimate lateral resistance of two-pile groups, with a tetrapod jacket foundation and a tripod foundation, for the prescribed load applied to piles. They demonstrated the change in the ultimate lateral resistance of pile group and the failure mode of the ground around the piles. The present study investigates the effect of

the direction of the ground movement on the ultimate lateral resistance of a 2x2 pile group for various horizontal directions. The horizontal direction angle is defined as being the angle between the direction of the ground movement and the pile to pile axis, and the angle varies from 0 to 90 degrees. The load applied to the piles is basically unknown and must be determined through computation.
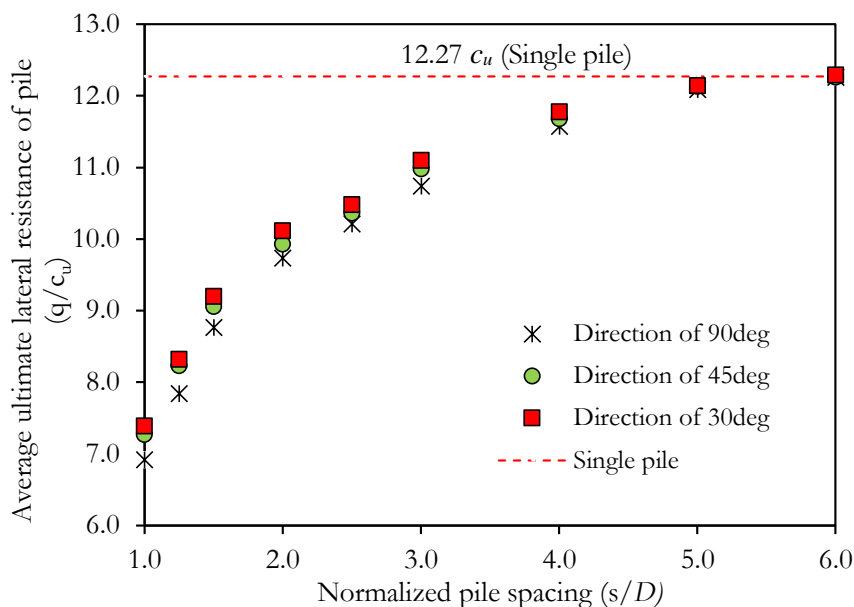
Figure 3.6. Effect of the direction of ground movement on average ultimate lateral resistance of 2x2 pile group

The effect of the direction of the ground movement on the average ultimate lateral resistance (q/c_u) is presented in **Fig. 3.6.** It indicates that the average ultimate lateral resistance increased with the increase in pile spacing for all cases of direction angles. It was the lowest at 90 degrees; however, the greatest difference in ultimate lateral resistance among the various direction angles did not exceed 7% at any pile spacing and little effect of the direction was observed. These results are preferable from the design viewpoint because the resistance performance of a pile group can be expected to be sufficient for any direction of ground movement. In all cases of ground movement direction, the difference was maximum at a small pile spacing. However, it is noticeable that the effect of the direction of the ground movement on the failure mode of the ground around the piles was different, as shown in **Figs. 3.4 and 3.7**. At the small pile spacing of 1.5 D, although the average ultimate lateral resistance of pile was similar for any direction of ground movement,

the change in the failure mode of the ground peripheral of the piles was clearly observed in **Figs. 3.4(a)**, **3.7(a)**, and **3.7(c)**. It is noted that the intermediate ground surrounding the four piles deformed in the cases of 30 and 45 degrees, whereas no plastic deformation was observed in the case of 90 degrees, as seen in **Fig. 3.4(a)**. For the pile spacing of 6.0 D, the failure mode of the ground was obtained as being almost the same as that in **Figs. 3.4(d)**, **3.7(b)**, and **3.7(d)** regardless of the direction of the ground movement.
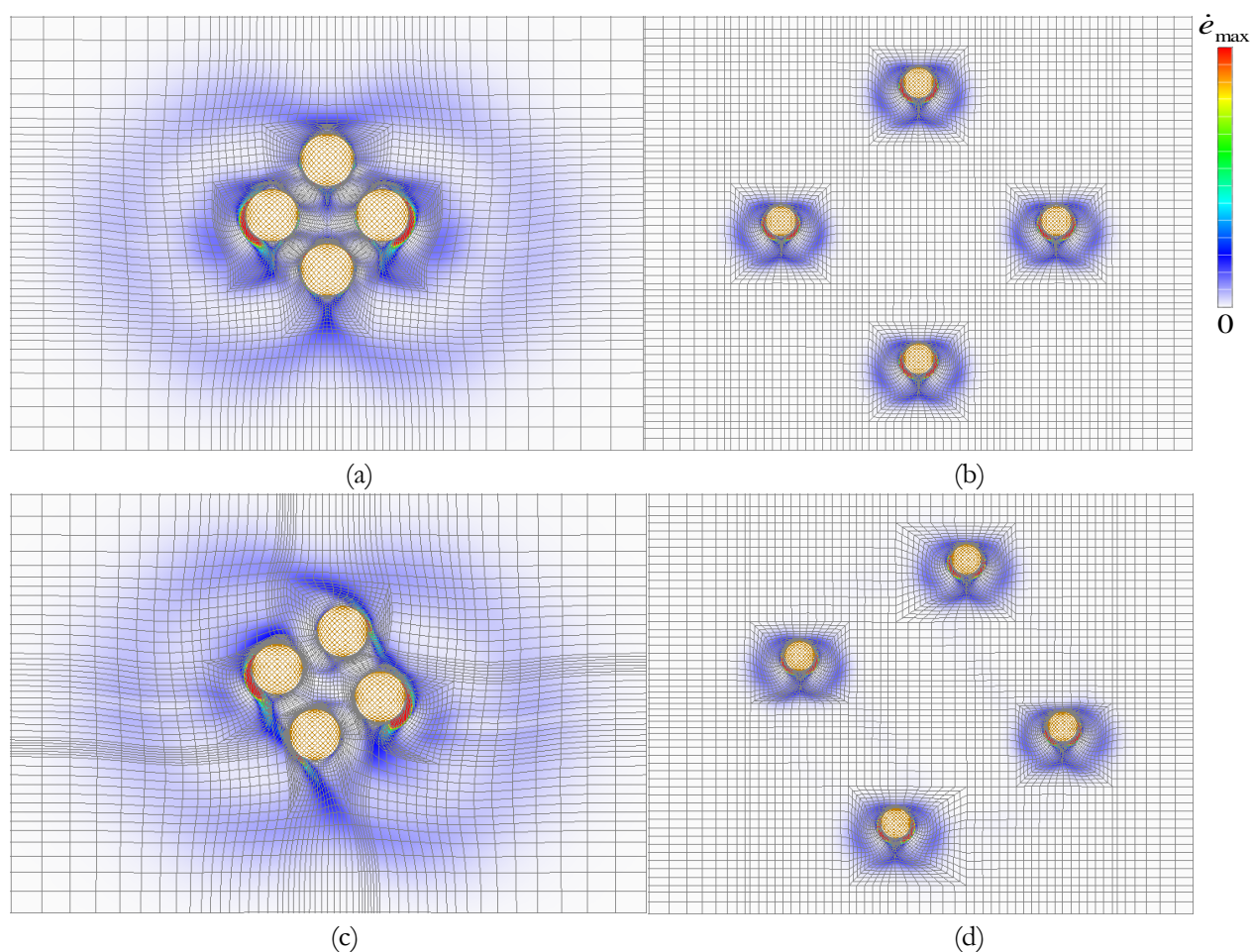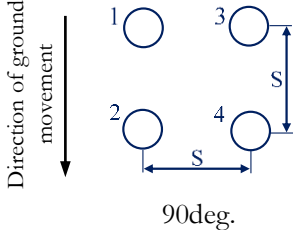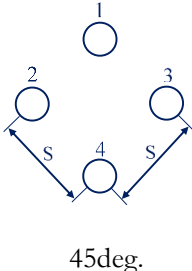
Figure 3.7. Deformation diagrams of 2x2 pile group: (a) s/D=1.5 and (b) s/D=6.0 in case of 45 degrees; (c) s/D=1.5 and (d) s/D=6.0 in case of 30 degrees

Moreover, to compare the performance of each pile in a group with that of a single pile, the lateral resistance of each pile in a group is calculated. The ratio of the lateral resistance of each pile to that of a single pile is defined as the load bearing ratio in this study. The ultimate lateral resistance of each pile was assessed by computing the reaction force at the center of each pile, where the fixed velocity boundary

condition is imposed. The results given in **Table 3.1** show that the load bearing ratio of each pile possessed two components of reaction, in which x and y components express the perpendicular and the parallel components to the direction of ground movement, respectively. The table indicates that the x component of reaction was generally very small in comparison to the y component of reaction, and that the total load bearing ratio of the pile almost coincided with that of the y component of reaction. The load bearing ratio of each pile tends to increase with the increase in pile spacing. In the case of 90 degrees, the load bearing ratio of the front pile was greater than that of the back pile in all cases of pile spacing. While the load bearing ratio of the front pile was slightly less than 1.0, a significant reduction in the load bearing ratio of the back pile was observed to be nearly 37% at a small pile spacing (s=1.5 D). When the pile spacing was about 6.0 D, the load bearing ratio of each pile was 1.0, which is identical to that of an isolated single pile. The failure mode was obtained as the single-pile mode, and the failure area of the ground around the pile reached 1.5 D~2.0 D from the pile center. In the case of 45 degrees, the load bearing ratios of the two side piles were significantly greater than those of the two middle piles at a small pile spacing. However, there was not much difference between the load bearing ratios of each pile for a pile spacing in the range of 4.0~6.0 D. In the two middle piles, the back pile may have been supported by the front pile and the two side piles so that the load bearing ratio of the back pile had the smallest value among them. The results showed that the effect of the direction of the ground movement on the load bearing ratio is considerable.

Table 3.1. Summary of load bearing ratios in 2x2 pile groups in case of 90 and 45 degrees

| Group size | s/D | Load bearing ratio | | | | | | | |
| | | 1st pile | | 2nd pile | | 3rd pile | | 4th pile | |
		x	y	x	y	x	y	x	y
	1.5	0.04	0.80	0.07	0.63	0.04	0.80	0.07	0.63
	2.0	0.02	0.86	0.05	0.73	0.02	0.86	0.05	0.73
	3.0	0.01	0.93	0.04	0.83	0.01	0.93	0.04	0.83
	4.0	0.01	0.98	0.03	0.91	0.01	0.98	0.03	0.91
	5.0	0	0.99	0.01	0.98	0	0.99	0.01	0.98
	6.0	0	1.00	0	1.00	0	1.00	0	1.00

1.5	0	0.72	0.12	0.91	0.12	0.91	0	0.42
2.0	0	0.79	0.07	0.95	0.07	0.95	0	0.54
3.0	0	0.92	0.04	0.96	0.04	0.96	0	0.71
4.0	0	0.96	0.01	0.97	0.01	0.97	0	0.90
5.0	0	0.98	0	1.00	0	1.00	0	0.97
6.0	0	1.00	0	1.00	0	1.00	0	1.00

45deg.

3.4 ULTIMATE LATERAL RESISTANCE OF LINE ALIGNMENT PILE GROUPS

3.4.1 Effect of direction of ground movement in case of pile group with few piles

This study considered groups of two, three, and four piles arranged in a row. The effect of the direction of the ground movement on the ultimate lateral resistance of the pile groups was widely investigated. Georgiadis et al. (2013b) reported a calculation for the ultimate lateral resistance of two piles in clay for various loading directions. Their results show that the ultimate lateral resistance of the pile group was changed significantly by the loading direction. However, the effect of the number of piles arranged in a row was not considered. In this study, the effect of the direction of the ground movement on the ultimate lateral resistance by an increase in the number of piles is addressed. The ultimate lateral resistance and the ground failure mechanism were found to depend on both the pile spacing and the pile number. An examination was conducted on two to four piles for the direction angle of the ground movement in the range of 0 to 90 degrees, in which the direction angle was defined as the angle between the direction of ground movement and the pile to pile axis. To discuss the effect of the direction of the ground movement for various numbers of piles, the average ultimate lateral resistance of pile in the pile group was computed by considering the pile number.
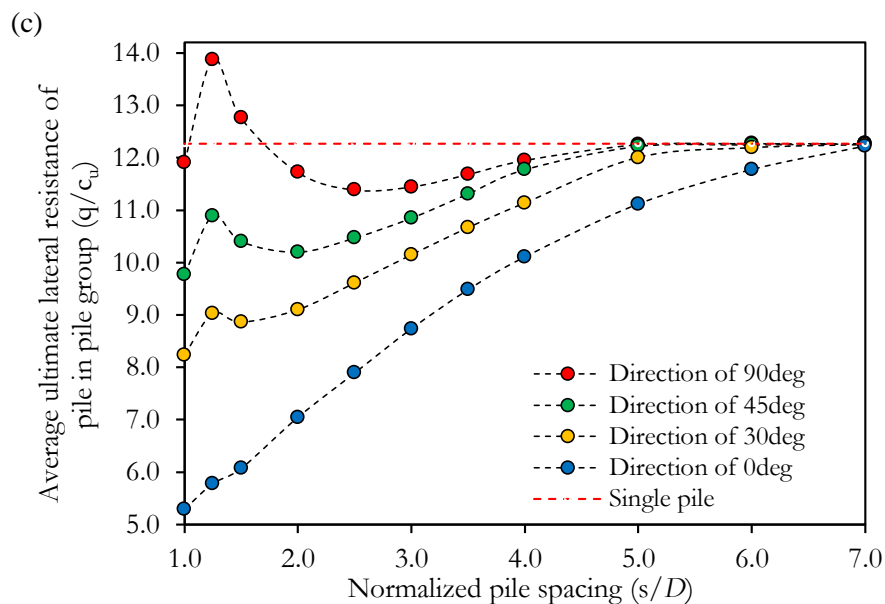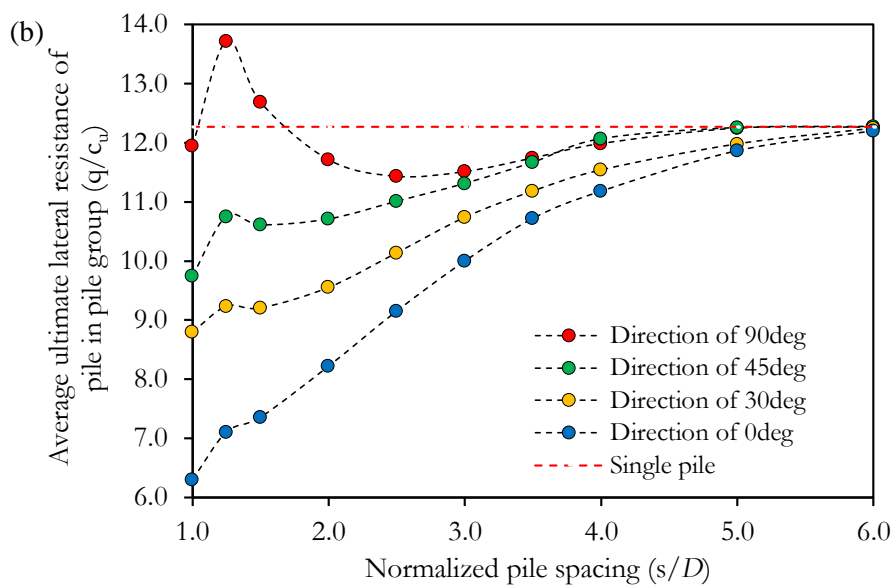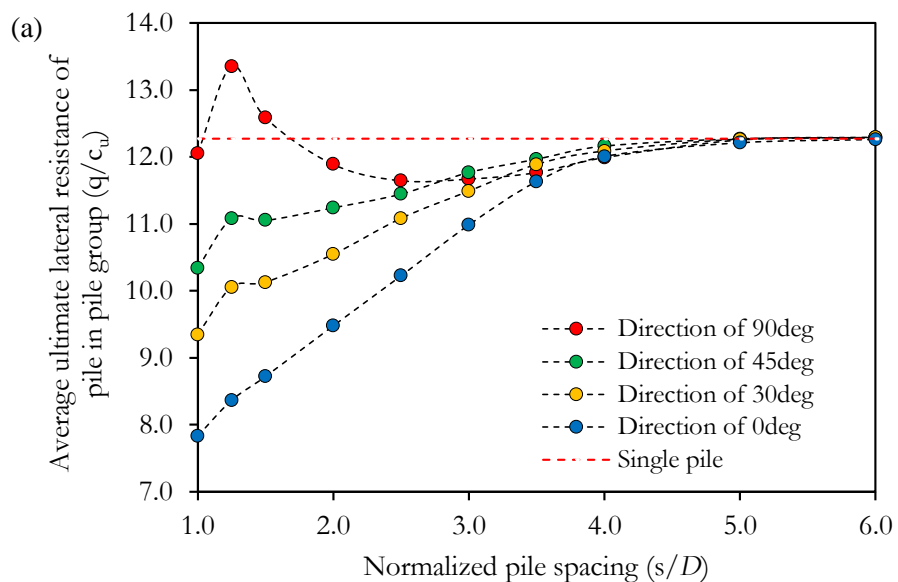
Figure 3.8. Average ultimate lateral resistance of pile in case (a) two-pile, (b) three-pile, and (c) four-pile groups

(a) Two-pile group

(b) Three-pile group

0°   45°

90°
c) Four-pile group
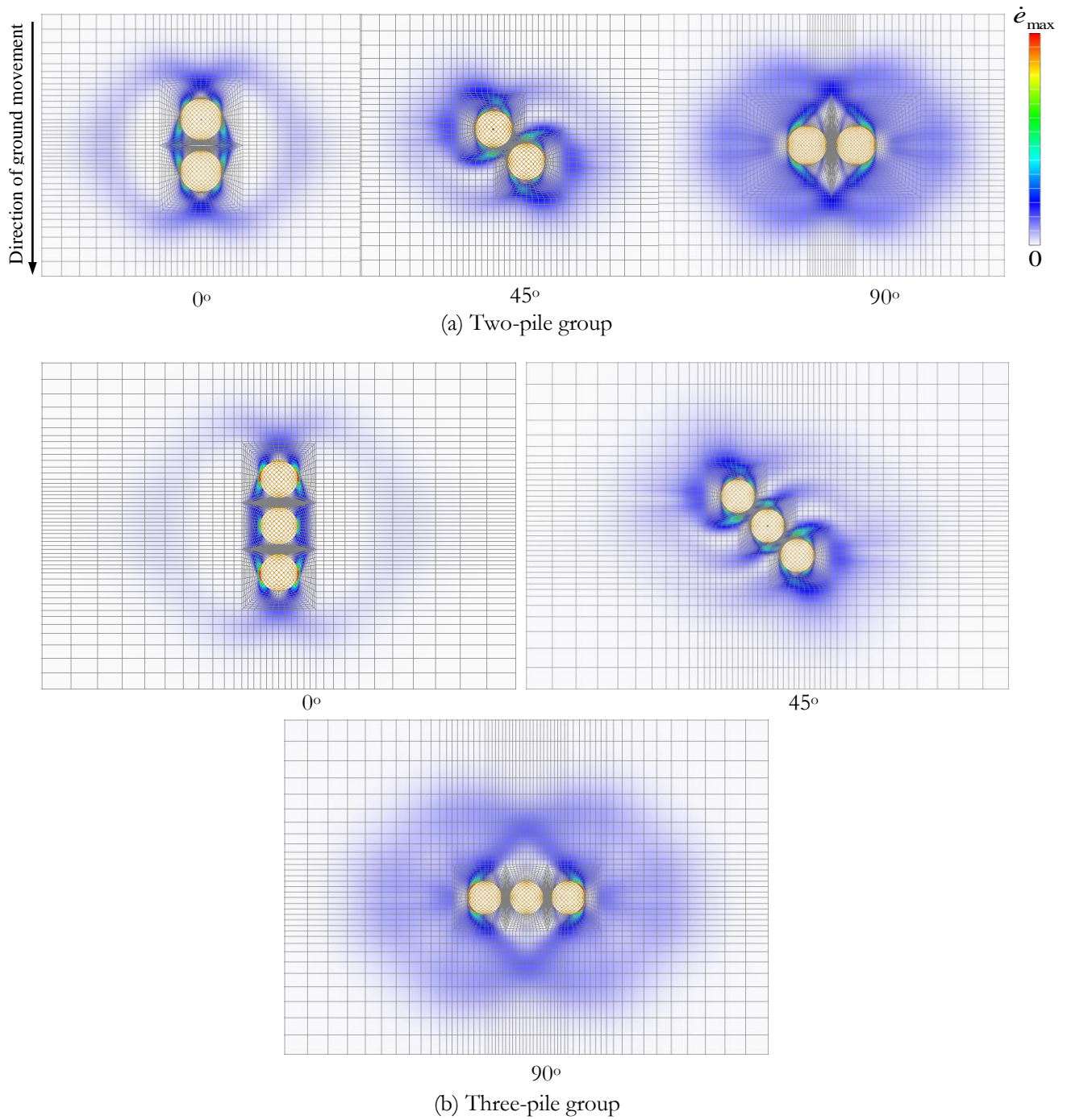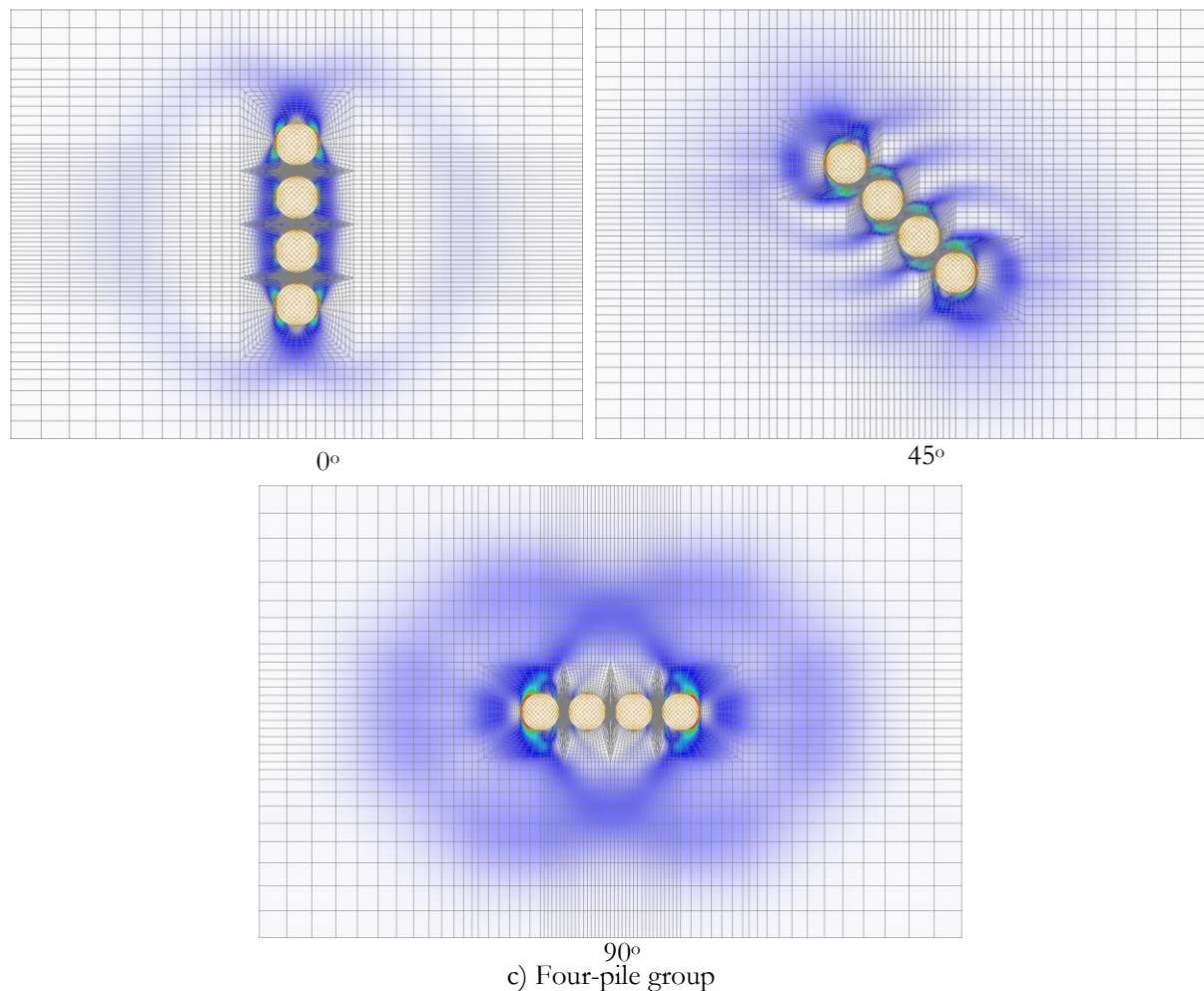
Figure 3.9. Failure modes of pile groups with normalized pile spacing s/*D*=1.25 in cases of 0, 45, and 90 degrees, respectively

Figure 3.8 shows the relationship between the average ultimate lateral resistance and the normalized pile spacing for an increase in pile number. Despite the number of piles, a similar trend was found in the computed relationship in the figure. In the case of two piles, the average ultimate lateral resistance decreased almost proportionally to the decrease in the direction angle of the ground movement in the range of 1.0 *D*-3.0 *D* spacing, and it coincided with that of a single pile with a range in pile spacing of 4.0 *D*-6.0 *D*, while the average ultimate lateral resistance increased non-linearly with an increase in pile spacing for all directions. In the case of 90 degrees, the average ultimate lateral resistance was slightly higher than that of a single pile in the range of nearly 1.0 *D*-1.75 *D*. This is because the two piles and the intermediate soil behaved as a rigid block, as shown in **Fig. 3.9(a)** of 90 degrees. Similar results can be found in the computational results in Georgiadis et al. (2013). However, the authors cannot find experimental data to verify them. It seems

appropriate that the average ultimate lateral resistance was the greatest in the case of 90 degrees, since the substantial distance of the pile spacing projected to the perpendicular plane against the ground movement was the largest even if the pile spacing was the same. However, as the failure mode of the pile-soil system varied depending on the pile spacing, the peak value for the average ultimate lateral resistance was obtained at a pile spacing of around 1.25 D. The trend to locally form the peak value was observed for other inclination angles at a pile spacing of around 1.25 D. In the cases of three-pile and four-pile groups, the obtained results also show a similar trend to that of the two-pile group in **Figs. 3.8(b)** and **(c)**. However, the difference in the average ultimate lateral resistance between the case of 90 degrees and that of 0 degrees increased with an increase in the number of piles. In the case of 90 degrees, the average ultimate lateral resistance of the pile group was the same for the pile spacing despite the number of piles. However, in the case of 0 degrees, the average ultimate lateral resistance was shown to vary with the number of piles and to decrease with an increase in the number of piles. The effect of the pile number on the trend in the ultimate lateral resistance against the pile spacing changed with the number of piles, where the range in pile spacing to vary the ultimate lateral resistance became wider. The other cases, varying from 0 to 90 degrees, were found to be in between those of 0 and 90 degrees.

As the preliminary analysis, discussed above, the effect of the direction of the ground movement was caused by changes in the failure mechanism of the ground around the piles. The typical failure modes of the two-pile, three-pile, and four-pile groups were influenced by the direction of the ground movement with a normalized pile spacing of s/D=1.25, as shown in **Fig. 3.9**. In the cases of 0 and 90 degrees, the intermediate ground of the piles did not yield any plastic deformation, whereas it clearly yielded plastic deformation in the case of 45 degrees. This indicates that shearing of the intermediate ground took place despite the same pile spacing in the cases of 0 and 90 degrees. It is interesting that the failure mode changed due to the direction of the ground movement in spite of the smaller pile spacing, and that the average ultimate lateral resistance continuously varied between the values of 0 and 90 degrees. It can be observed from **Fig. 3.9(a)** to **Fig. 3.9(c)** that the area of the failed ground became wider as the number of piles became greater due to the group effect. The failure zone of the ground around the piles was about 3.0 D-

3.5 *D* from the centers of the piles for the two-pile group, 4.5 *D*-5.0 *D* for the three-pile group, and 5.5 *D*-6.0 *D* for the four-pile group.

3.4.2 Effect of direction of ground movement in case of infinitely long row of piles

In practice, an infinite number of piles in a long row is sometimes employed to support structures. Chen (1994) and Bransby and Springman (1999) used a finite element analysis to evaluate the group effect of rows of closely spaced piles under lateral loading from ground movement. Geogiadis et al. (2013c) employed analytical upper bound plasticity methods to investigate the undrained limiting lateral resistance of piles in a row. However, no reports on the effect of the direction of the ground movement on an infinitely long row of piles can be found in the literature. Therefore, it is necessary to search for solutions that will give insight into this problem and to predict the effect in practice. In this study, an analysis was conducted for a unit cell by considering the symmetric property of the problem. It is noted that the width of the unit cell is dependent on the pile spacing and that the average ultimate lateral resistance of the piles is determined by the pile number per length. The ultimate lateral resistance of piles was computed against the horizontal movement in the same way as before. The typical finite mesh element and boundary condition of a unit cell on an infinitely long row of piles are shown in **Fig. 3.10(a)**. As seen in this figure, the unit cell is defined due to the symmetry of the geometry to consider the behavior of the infinitely long row of piles. The figure expresses the model of the half piles and the intermediate ground for the direction angle of 45 and 90 degrees between the direction of ground movement and the pile to pile axis. The setting of the boundary condition of the unit cell is similar to that of pile groups. The results of the failure modes for the intermediate ground between the piles varied significantly depending on the range in normalized pile spacing of 1.5-6.0, as shown in **Fig. 3.10(b)**. The calculated results for the ultimate lateral resistance of the unit cell are shown in **Fig. 3.11(a)**. The ultimate lateral resistance was the same as that of Geogiadis et al. (2013c). It is interesting to survey the failure mode of the ground when the ultimate lateral resistance of each pile is identical with that of a single pile at the pile spacing around 1.5 *D*. However, it is difficult to directly discuss since this numerical method cannot assess the ultimate lateral resistance in succession for

the change in pile spacing. The relationship between the ultimate lateral resistance and the failure mode has not been made clear, but it is apparent that the failure mode changed from the combined mode of two failure modes for piles to the isolated two single failure mode.

(a)   (b)
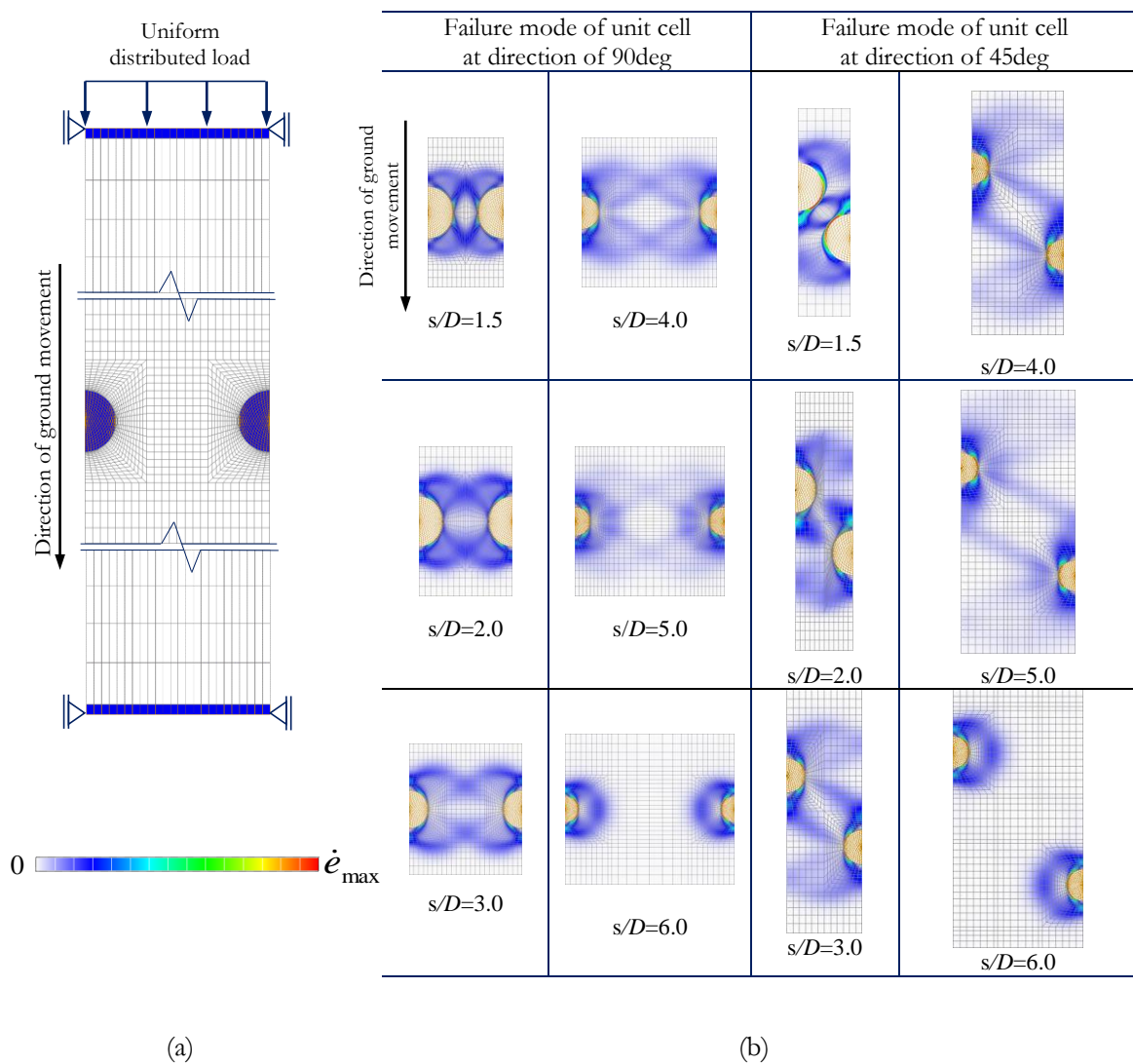
Figure 3.10 a) Typical finite element mesh and boundary conditions of unit cell in case of 90 degrees
b) Failure modes of unit cell for one row of infinite number of piles in case of 90 degrees and 45 degrees

Here, the ultimate lateral resistance of two and three rows of an infinite number of piles was also analyzed. However, the pile arrangement was limited to the lattice arrangement where the unit cell can be defined. It can be seen in **Fig. 3.11** that both the group effect and the effect of the direction of the ground movement on the average ultimate lateral resistance of the piles were the same as those of the one row of an infinite number of piles. In the case of 90 degrees, the average ultimate lateral resistance of the row of

piles was found to decrease with an increase in the number of rows. The same trend can be seen in the case of 45 degrees. On the other hand, the difference in average ultimate lateral resistance between the cases of 90 and 45 degrees decreased with an increase in the number of rows. It was found that the difference became almost zero in the case of the three rows of piles.
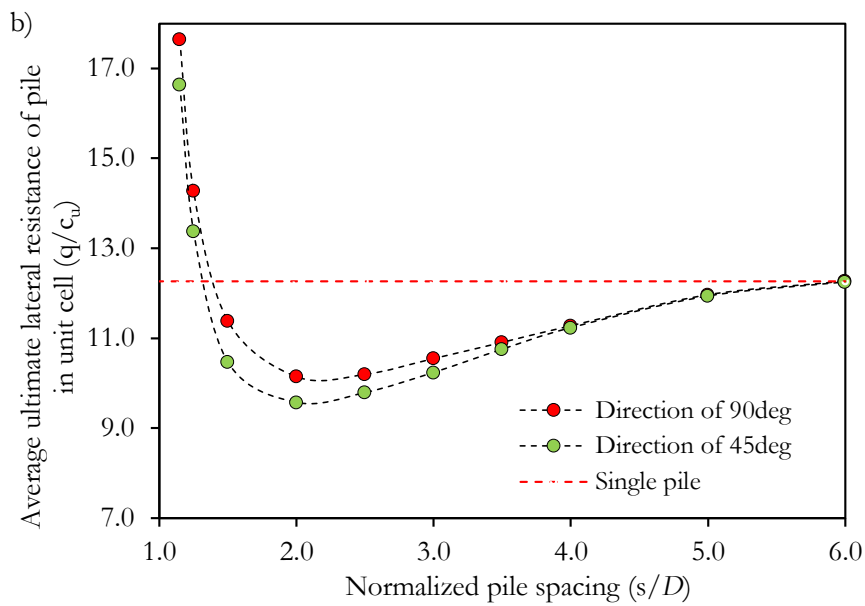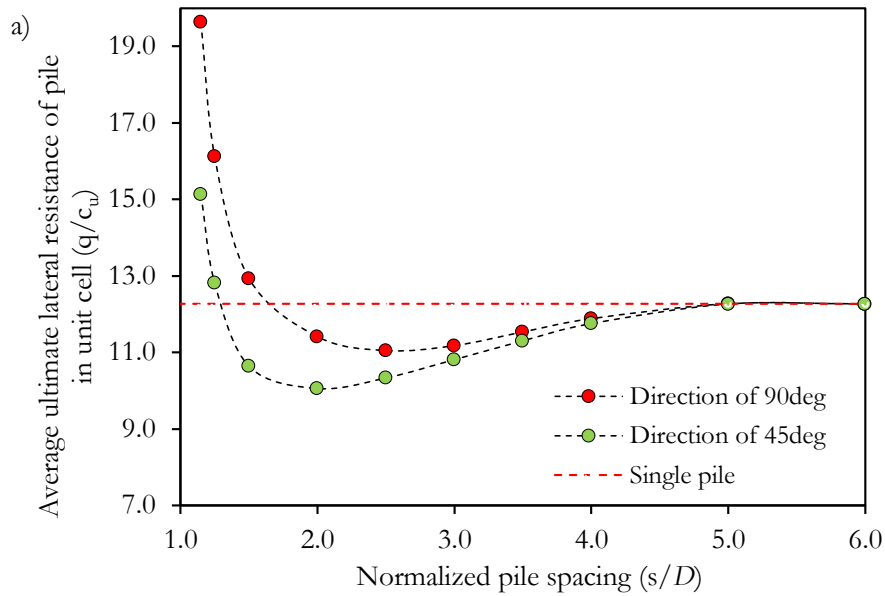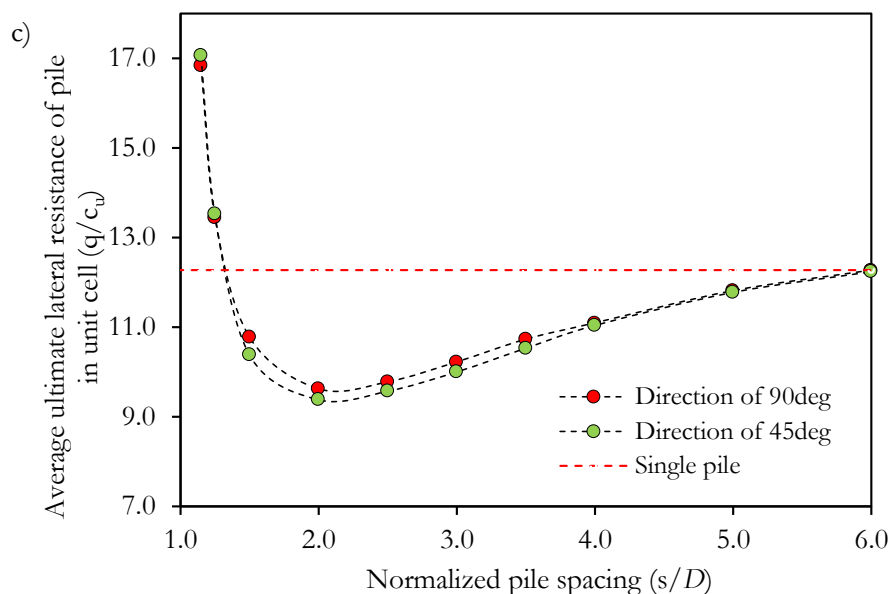
Figure 3.11 Average ultimate lateral resistance of pile in unit cell in case (a) one row; (b) two rows, and (c) three rows of piles

It is noted that the ultimate lateral resistance of multiple rows of piles was almost the same for various directions of ground movement. Since the staggered arrangement of piles is often employed in practice, it needs to be surveyed in the same way. However, it is difficult to set the unit cell to represent the resistance mechanism of a staggered arrangement of piles. Therefore, this problem will be addressed in a future study. The ultimate lateral resistance of piles in a staggered arrangement is thought to be higher than that in a lattice arrangement. However, the effect of the direction of the ground movement can be predicted as being the same for the staggered arrangement of piles as for the lattice arrangement of piles.
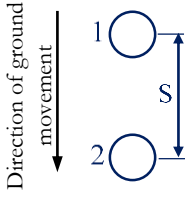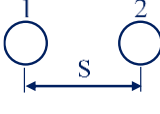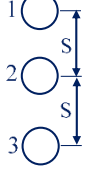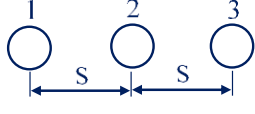
3.5. LOAD BEARING RATIO OF PILES IN PILE GROUPS

Significant differences in the piles were seen in the results for two piles, three piles, and an infinite number of piles in a row due to the group effect. **Tables 3.2** and **3.3** present summaries of the obtained results for the load bearing ratios of piles for a variety of spacing. The difference in load bearing ratios can be seen clearly for directions in ground movement. However, the load bearing ratios were generally less than 1.0 at a small pile spacing and increased with an increase in pile spacing to finally converge to 1.0.

In the case of a direction angle of 0 degrees, the two-pile and three-pile cases were compared. The load bearing ratio was greater for the front pile and less for the back pile. The difference in the load bearing
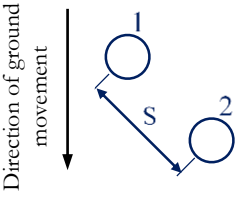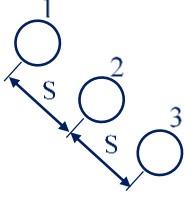
ratios of the piles were comparatively large. However, this trend was greatly seen at a small pile spacing and was seen less with an increase in the pile spacing. It is noted that the load bearing ratio of the middle pile was the smallest for the three-pile case as the pile spacing was small.

Table 3.2. Summary of load bearing ratios in case of 0 and 90 degrees

Group size	s/D	Load bearing ratio		
		1st pile	2nd pile	3rd pile
0deg.	1.5	0.76	0.67	
	2.0	0.81	0.73	
	3.0	0.93	0.86	
	4.0	0.99	0.96	
	5.0	1.00	0.99	
90deg.	1.5	1.03	1.03	
	2.0	0.97	0.97	
	3.0	0.95	0.95	
	4.0	0.98	0.98	
	5.0	1.00	1.00	
0deg.	1.5	0.72	0.52	0.57
	2.0	0.86	0.54	0.61
	3.0	0.94	0.75	0.76
	4.0	0.97	0.91	0.85
	5.0	1.00	0.98	0.92
90deg.	1.5	1.04	1.02	1.04
	2.0	0.98	0.90	0.98
	3.0	0.98	0.85	0.98
	4.0	1.00	0.94	1.00
	5.0	1.00	1.00	1.00
One row of infinite number of piles 90deg.	1.15	1.60		
	1.5	1.05		
	2.0	0.93		
	3.0	0.91		
	4.0	0.97		
	5.0	1.00		

Table 3.3 Summary of load bearing ratios in case of 45 degrees

| Group size | s/D | Load bearing ratio | | | | | |
| | | 1st pile | | 2nd pile | | 3rd pile | |
		x	y	x	y	x	y
Direction of ground movement (piles 1, 2 diagram)	1.5	0.04	0.93	0.05	0.87		
	2.0	0.03	0.94	0.04	0.90		
	3.0	0.03	0.97	0.03	0.95		
	4.0	0.02	1.00	0.03	0.99		
	5.0	0	1.00	0	1.00		
(piles 1, 2, 3 diagram)	1.5	0.02	0.92	0.07	0.79	0.03	0.89
	2.0	0.02	0.93	0.06	0.80	0.03	0.91
	3.0	0.01	0.96	0.04	0.87	0.01	0.93
	4.0	0	1.00	0.03	0.98	0	0.99
	5.0	0	1.00	0	1.00	0	1.00
One row of infinite number of piles	1.15	0.07	1.23				
	1.5	0.05	0.87				
	2.0	0.03	0.82				
	3.0	0.02	0.88				
	4.0	0	0.96				
	5.0	0	1.00				

In the case of a direction angle of 90 degrees, the cases of two piles, three piles, and an infinite number of piles were analyzed. The variance in the load bearing ratios was comparatively small among the piles despite the pile spacing. The general property of the load bearing ratios can be seen typically for the case of an infinite number of piles. It was greater than unity at a smaller pile spacing, but it decreased with an increase in pile spacing and became less than 1.0 around 2.0 D and 3.0 D. Beyond the pile spacing of 3.0 D, the load bearing ratio of the piles increased with the pile spacing and approached 1.0.

In the case of a direction angle of 45 degrees, the cases of two piles, three piles, and an infinite number of piles were analyzed. The same trend in load bearing ratios was obtained as in the case of 90 degrees, but the uniqueness of this case was that two orthogonal components existed in the reaction force. The component of the reaction force in the same direction as the ground movement was large, while that of the orthogonal direction was found to be comparatively small. Hence, the load applied to the piles almost

coincided with the reaction component for the same direction of ground movement.

3.6 CONCLUSIONS

This study has investigated the ultimate lateral resistance of pile groups against the horizontal ground movement of clayey soils using the rigid plastic finite element method. The group effect of the piles and the effect of the direction of the ground movement on the ultimate lateral resistance were analyzed for changes in pile spacing.

The conclusions of this study are as follows:

1. The ultimate lateral resistance of piles was analyzed against the horizontal ground movement by defining the displacement boundary value problem. The ultimate lateral resistance was obtained by computing the resultant reaction force of the piles. The advantage of this method is that it can assess the load bearing ratio of piles in a pile group at the limit state. The RPFEM provided the ultimate lateral resistance of an isolated single pile as 12.27 c_u for a perfectly rough pile in clayey soils where c_u is the undrained shear strength of clayey soil. The failure zone of the ground around the pile was found to be in the range of 1.5 D-2.0 D from the center of the pile. It was similar to the results reported by Broms (1964).

2. The group effect in the ultimate lateral resistance of piles was clarified by varying the pile spacing. Regarding the 2x2 arrangement of four piles, as well as the two, three, four, and infinite number of piles arranged in a row, the group effect was assessed by changing the direction of the ground movement. For each case, the load bearing ratio of the pile was examined.

3. The effect of the pile spacing on the ultimate lateral resistance was found to reflect the failure mode of the pile-soil system. When the pile spacing was large, the failure mode of the ground around each pile coincided with that of a single pile, but as the pile spacing decreased, the failure modes of the ground for the piles interfered with each other. The group effect on the ultimate lateral resistance appeared at this stage. The intermediate ground between the piles formed a rigid block in the failure mode of piles and a ground system when the pile spacing was even smaller.

4. In the case of the 2x2 piles, the ultimate lateral resistance of each pile was shown to be equal to that of a single pile when the pile spacing was large, and to decrease monotonically as the pile spacing decreased. Almost no difference was found in the average ultimate lateral resistance of pile for changes in the direction

of the ground movement. However, the load bearing ratio of the piles varied among the piles, and it was seen to be larger in the front pile with respect to the ground movement and smaller in the back pile. It varied with the direction of the ground movement.

5. In the case of the piles in a row, the ultimate lateral resistance was equal to that of a single pile when the pile spacing was large. It was obtained to vary greatly depending on the pile spacing and the direction of the ground movement. With the decrease in pile spacing, the ultimate lateral resistance of the piles decreased due to the group effect. However, when the pile spacing was less than about 2.0 D, the ultimate lateral resistance was found to increase greatly regardless of the direction of the ground movement. For the piles in a row orthogonal to the ground movement, the ultimate lateral resistance of each pile was larger than that of a single pile when the pile spacing was small. On the contrary, for the piles in a row in the same direction as the ground movement, the ultimate lateral resistance of each pile decreased monotonously as the pile spacing decreased. As for the group effect, the load bearing ratio of each pile was computed in detail with respect to the changes in the direction of the ground movement.

✧ **Publication:** Chapter 3 is published as article: **Pham, N. Quang**, Ohtsuka, S., Isobe, K. and Fukumoto, Y.: Group effect on ultimate lateral resistance of piles against uniform ground movement, **Soils and Foundations**, 59(1), 27-40, 2019. DOI: https://doi.org/10.1016/j.sandf.2018.08.013

References

Bauer, J., Kempfert, H.-G., and Reul, O. (2016). Lateral pressure on piles due to horizontal soil movement. International Journal of Physical Modelling in Geotechnics, 16 (4), 173-184.

Bransby, M.F. and Springman, S.M. (1999). Selection of load-transfer functions for passive lateral loading of pile groups. Computers and Geotechnics. 24 (3), 155-184.

Broms, B.B. (1964). Lateral Resistance of Piles in Cohesive Soils. Journal of the Soil Mechanics and Foundations Division. ASCE. 90 (2), 27-63.

Cox, W.R., Dixon, D.A. and Murphy, B.S. (1984). Lateral-Load Tests on 25.4mm (1-in.) Diameter Piles in Very Soft Clay in Side-by-Side and In-line Groups. Laterally Loaded Deep Foundations: Analysis and Performance. ASTM STP 835. Kansas City. Mo., 122-139.

Chen, L.T. (1994). Effect of lateral soil movements on pile foundation. PhD thesis, Univ. of Sydney, Sydney, Australia.

Chen, L.T. and Poulos, H.G. (1996). The behavior of piles subjected to lateral soil movements. Res. Rep. No. 731, Univ. of Sydney, Sydney, Australia.

Chen, L.T. and Poulos, H.G. (1997). Piles Subjected to Lateral Soil Movements. J. Geotech. Geotech. Eng. ASCE. 123 (9), 802-811.

Chen, L.T., Poulos, H.G. and Hull, T.S. (1997). Model test on pile groups subjected to lateral soil movement. Soils and Foundations. 37 (1), 1-12.

Georgiadis, K., Sloan, S. W. and Lyamin, A.V. (2013a). Ultimate lateral pressure of two side-by-side piles in clay. Géotechnique. 63 (9), 733-745.

Georgiadis, K., Sloan, S. W. and Lyamin, A.V. (2013b). Effect of loading direction on the ultimate lateral soil pressure of two piles in clay. Géotechnique. 63 (13), 1170-1175.

Georgiadis, K., Sloan, S. W. and Lyamin, A.V. (2013c). Undrained limiting lateral soil pressure on a row of piles. Computer and Geotechnics. 54, 175-184.

Goh, A. T. C., Tech, C.I. and Wong, K. S. (1997). Analysis of piles subjected to embankment induced lateral soil movements. Journal of Geotechnical and Geoenvironmental Engineering. ASCE. 123 (9), 792-801.

Hoshina, T., Ohtsuka, S. and Isobe, K. (2011). Ultimate bearing capacity of ground by rigid plastic finite element method taking account of stress dependent non-linear strength property. Journal of Applied Mechanics. 6, 191-200. (in Japanese)

Kashiwa, H., Kurata, T., Shoji, M., Hayashi, Y., Suita, K. and Tamura, S. (2007). Nonlinear behavior of pile group in dry sand based on lateral cyclic loading tests with large displacement amplitude. 4th Int. Conf. on Earthquake Geotechnical Engineering, Paper No. 1721, Thessaloniki, Greece.

Komura, S., Shiratori, Y., Ohtsuka, S. and Hoshina, T. (2016). Discussion on ultimate lateral resistance of pile in clayey ground during earthquake. Society of Civil Engineering. 72 (2), 48-61. (in Japanese)

Llyas, T., Leung, C.F., Chow, Y.K. and Budi, S.S. (2004). Centrifuge Model Study of Laterally Loaded Pile Groups in Clay. J. Geotech. Geoenviron. Eng. ASCE. 130 (3), 274-283.

Miao, L. (2005). Effects of lateral soil movements on piles. Ph.D. Thesis, Nanyang Technological University.

Miao, L.F., Goh A.T.C., Wong, K.S., and Teh, C.I. (2008). Ultimate soil pressure for pile groups in soft clay subjected to lateral soil movements. DFI Journal: The Journal of the Deep Foundations Institute 2(1): 42-51.

Nguyen, Du L., Ohtsuka, S., Hoshina, T. and Isobe, K. (2016). Discussion on size effect of footing in ultimate bearing capacity of sandy soil using rigid plastic finite element method. Soils and Foundations. 56 (1), 93-103.

Pan, J. L. (1998). Experimental and numerical study of the behavior of piles subjected to lateral soil movement. Ph.D. Thesis, Nanyang Technological University.

Pan, J.L., Goh, A. T. C., Wong, K.S. and Teh, C. I. (2000). Model tests on single pile in soft clay. Canadian Geotechnical Journal. 37, 890-897.

Pan, J.L., Goh, A. T. C., Wong, K.S. and Teh, C. I. (2002). Ultimate soil pressures for piles subjected to lateral soil movements. Journal of Geotechnical and Geonvironmental Engineering. ASCE. 128 (6), 530-535.

Randolph, M. F. and Houlsby, G. T. (1984). The limiting pressure on a circular pile loaded laterally in cohesive soil. Geotechnique. 34 (4), 613-623.

Stewart, D. P. (1992). Lateral loading of piled bridge abutments due to embankment construction. Ph.D. Thesis, The University of Western Australia.

Su, D. and Zhou, Y.G. (2015). Effect of loading direction on the response of laterally loaded pile groups in sand. International Journal of Geomechanics. ASCE. 16 (2), 1-12.

Tamura, T., Kobayashi, S. and Sumi, T. (1984). Limit analysis of soil structure by rigid plastic finite element method. Soils and Foundations. 24 (1), 34-42.

Tamura, T., Kobayashi, S. and Sumi, T. (1987). Rigid Plastic Finite Element Method for Frictional Materials. Soils and Foundations. 27 (3), 1-12.

Tamura, T., Kobayashi, S. and Sumi, T. (1990). Rigid Plastic Finite Element Method in Geotechnical Engineering Computational. Current Japanese Material Research, 15-23.

Zhao, Z., Li, D. and Zhang, F. (2017a). Ultimate lateral bearing capacity of tetrapod jacket foundation in clay. Computer and Geotechnics. 84, 164-173.

Zhao, Z., Kouretzis, G., Sloan, S. W. and Gao, Y. (2017b). Ultimate lateral resistance of tripod pile foundation in clay. Computer and Geotechnics. 92, 220-228.

Chapter 4

ULTIMATE BEARING CAPACITY OF RIGID FOOTING UNDER ECCENTRIC VERTICAL LOAD

4.1 INTRODUCTION

Calculating the ultimate bearing capacity is an important part of designing foundations in terms of examining the stability of the footing-soil system. The superposition formula proposed by Terzaghi (1943) has been widely employed to calculate the ultimate bearing capacity of the footing under a vertical load. It takes into account the effects of soil cohesion, surcharge and soil weight. The formula is typically expressed as follows:

$$q = cN_c + \frac{1}{2}\gamma B N_\gamma + \gamma D_f N_q \tag{1}$$

where N_c, N_q and N_γ are the bearing capacity factors, which show the effects of soil cohesion c (kN/m²), deep surcharge D_f (m) and soil unit weight γ (kN/m³). These factors are the functions of the internal friction angle of the soil, ϕ, under the footing. B is the width of the footing (m).

In geotechnical engineering, rigid footings have routinely been designed to withstand the complex loads that result from the combination of vertical and horizontal as well as moment loads. Typically, the vertical load stems from the weight of the superstructure, the horizontal load comes from wind and wave loads and the moment load comes from the eccentric vertical or horizontal loads. In practice, rigid footings often suffer under the eccentric vertical load. Based on the results of models test on sandy and clayey soils, Meyerhof (1953) reported the effect of the eccentric vertical load on the ultimate bearing capacity of footings. He introduced the concept of the effective footing width, $B' = B - 2e$, where e is the eccentricity length which is the length from the loading point to the center of the footing. The effective width formula using B' is often applied when designing foundations. The effect of the eccentric vertical load on the ultimate bearing capacity has been investigated by several researchers using numerical analyses and model tests. Georgiadis et al. (1988), Gottardi et al. (1993), Loukidis et al. (2008, 2009), Tang et al. (2014) and Yahia-Cherif et al. (2017) used numerical analyses to calculate the ultimate bearing capacity against the

eccentric vertical load on sandy soil. In recent years, Rao et al. (2015), Shen et al. (2016) and Khitas et al. (2017) reported the effect of the eccentric vertical load on the ultimate bearing capacity on clayey soil. The numerical results show that the ultimate bearing capacity was significantly changed by the increase in eccentricity length *e*. The same results were also obtained in model tests conducted by Meyerhof (1953), Prakash et al. (1971), Zadroga (1994) and Okamura et al. (2002). Although many works have been performed to investigate the ultimate bearing capacity against the eccentric vertical load, they were conducted independently under limited conditions for the soil material and the friction of the footing base. Therefore, a comprehensive understanding of both the ultimate bearing capacity formula and the failure envelope in vertical load and moment load planes has not yet been established.

In footing-soil systems, the ultimate bearing capacity of the footing depends on the friction condition between the footing and the soil. Although it depends on the footing material, such as wood, steel or concrete, it has been modeled under one of two extreme conditions, namely, perfectly rough or perfectly smooth. Tang et al. (2014) and Rao et al. (2015) studied the ultimate bearing capacity of footings subjected to an eccentric load by using an interface element. They found that the application of an interface element is effective for determining the ultimate bearing capacity of a rigid footing and the failure mechanism of the footing. In the present study, the rigid plastic finite element method (RPFEM) is employed with a two-dimensional analysis to determine the ultimate bearing capacity of a rigid footing placed on uniform layers of sandy and clayey soils subjected to an eccentric vertical load. The RPFEM has been employed in geotechnical engineering by Tamura et al. (1984, 1987, 1990) and Asaoka et al. (1986, 1987, 1990). Hoshina et al. (2011) introduced a new constitutive equation for the solid element, to simulate the footing and the soil, and the interface element, to simulate the interface plane between the footing and the soil, based on the upper bound theorem in the limit analysis. In this study, the applicability of the rigid plastic constitutive equation to the assessment of the ultimate bearing capacity of a footing under an eccentric vertical load is examined from the viewpoint of the interaction between the footing and the soil and the failure mode of the footing-soil system.

In addition, most of the previous studies on clayey soil, such as those by Bransby (2001), Gourvenec (2008) and Khitas et al. (2017), considered a fully bonded interface between the footing and the soil which is capable of transmitting full tension. However, the occurrence of tensile stress in the soil was not real.

Some literature is available on rigid footings under eccentric vertical loads with a zero-tension interface. Salencon et al. (1995) reported the ultimate bearing capacity of a shallow foundation under an eccentric load with a zero-tension interface on uniform soil based on a limit analysis of soil plasticity. Recently, Rao et al. (2015) and Shen et al. (2016) investigated the undrained ultimate bearing capacity of an eccentrically loaded footing with a zero-tension interface by the finite element method. Their findings raise the question of the effect of the footing-soil tensile stress on the ultimate bearing capacity and the failure mechanism in the presence of eccentric loading. In this study, a zero-tension analysis is introduced to widely consider the interaction between the footing and the soil in clayey soil. The study investigates the effect of the eccentric vertical load on the ultimate bearing capacity in the case of sandy and clayey soils under two extreme friction conditions of the footing base in the normalized form of V/V_{ult} and e/B, where V_{ult} indicates the ultimate bearing capacity under the centric vertical load. The failure envelope in the plane of V/V_{ult} and M/BV_{ult} is further investigated where M is the independently prescribed moment.

4.2. APPLICABILITY TO CENTRAL VERTICAL LOAD UNDER TWO CONTACT CONDITIONS

As was mentioned in the Introduction, the objective of this study is to introduce a two-dimensional model to analyze the behavior of the ground below the footing. **Figure 4.1 (a)** shows a typical finite element mesh and boundary condition for the rough condition to simulate the footing-soil system using an interface element at the footing-soil contact plane. The dimensions of the model were set to be large enough to ensure that the boundary would have no effect on either the failure mode of the ground around the footing or the calculated results. The load was applied at a central point of the footing with a width $B = 5.0$ m; it was simulated by concentrated loading. The footing was modeled as a solid element and the strength of the footing was set to be higher than that of the soil in order to simulate a rigid footing. The footing and the soil were modeled as rigid perfectly plastic material with the following properties: the unit weight of the footing and the soil was $\gamma_f = \gamma_{soil} = 18$ kN/m³, the shear strength of the footing material was $c_f = 50000$ kPa and the internal friction angle of the footing was $\phi_f = 0$ deg. For sandy soil, the internal friction angle was set at $\phi_{soil} = 30$ deg, but small cohesion was introduced to stabilize the computation process. $c = 0.5$ kPa was employed in the analysis, but the effect of cohesion on the ultimate bearing capacity was found to be small,

at less than 1%, through a numerical survey by changing the cohesion widely. The study was conducted under two friction conditions of the footing surface with the interface element properties shown in **Table 4.1.**

a) Typical finite element mesh and boundary condition (Rough condition, V_{ult}=3836 kN/m)

b) Smooth condition, V_{ult}=1981 kN/m
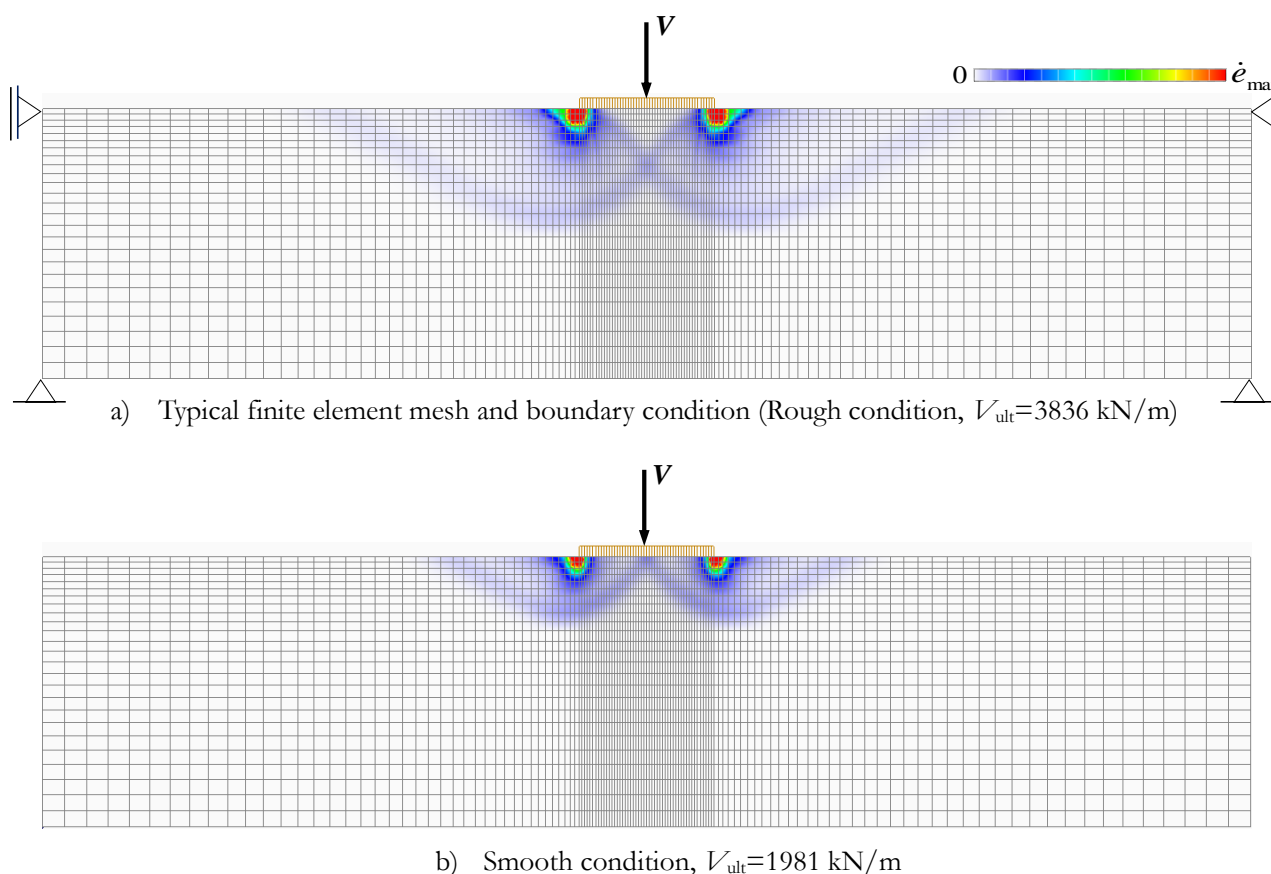
Figure 4.1 Typical finite element mesh, boundary conditions and failure modes of footing under centric vertical load with B=5.0 m in sandy soil of ϕ=30deg

Table 4.1. Interface element properties of sandy soil.

Parameter	Rough condition	Smooth condition
Internal friction angle ϕ_s (°)	30	0
Shear strength c_s (kPa)	0.5	0.5

The ultimate bearing capacity of the footing was generally achieved as a value close to 3836 kN/m for the rough condition and close to 1981 kN/m for the smooth condition which is 52% of that of the case for the rough condition. These results agree well with the 4069 kN/m of the superposition formula proposed by Terzaghi (1943) for the rough condition. The results obtained for the strain rate distribution of the footing under a centric vertical load are shown in **Fig. 4.1**. The norm of the strain rate, presented by

contour lines, is in the range of $\dot{e}_{max}$ to $\dot{e}_{min} (= 0)$. The distribution of $\dot{e}$ shows the failure mode of the ground and reflects the footing-soil contact condition. Figure 2 shows the failure mode of the footing-soil system under two friction conditions. The failure zones of the ground around the footing are observed to be in the range of 2.0 B to 2.5 B from the edge of the footing for the rough condition (**Fig. 4.1 (a)**) and 1.0 B to 1.5 B for the smooth condition (**Fig. 4.1 (b)**). The failure areas are different due to being affected by the friction condition of the footing surface. Furthermore, the rigid block that formed below the footing was apparently different between the two friction conditions. The obtained failure mode shows a good agreement with the slip line of the rough condition described by the FEM of Loukidis et al. (2008) and Nguyen et al. (2016) without the use of an interface element. The failure mechanism of the rough condition is divided into two parts in **Fig. 4.1 (a)**. In one part, the triangular wedge under the footing moves downward as a rigid block with the same velocity as the footing. In the other part, a log-spiral shear zone is seen in the two edges of the footing. For the smooth condition in **Fig. 4.1 (b)**, the failure mechanism is characterized by two rigid triangular wedges. The two rigid wedges tend to move towards the two edges of the footing. This is because the interface element between the footing and the soil allows for the horizontal movement of the wedges. The failure mechanism of the smooth footing also presents a log-spiral shear zone in the two edges of the footing in the same way as with the rough footing. The obtained results for the ultimate bearing capacity and the failure mechanism in this study were found to closely match those in past works.

4.3 INTERACTION OF FOOTING AND GROUND UNDER ECCENTRIC VERTICAL LOAD

4.3.1 Case studies for sandy soil under two contact conditions

In practice, rigid footings are often subjected to eccentric vertical loads. Loukidis et al. (2008) and Guetari et al. (2018) evaluated the ultimate bearing capacity of an eccentrically loaded footing on sandy soil at the interval 0.0 B to 0.4 B of eccentricity for a rough footing. In the results of their studies, a difference was found in the distribution of normal stress σ_n acting on the footing base corresponding to eccentricity length e. However, only a few researches have been conducted to evaluate the distribution of contact stress under two friction conditions of the footing-soil surface, namely, rough and smooth conditions.
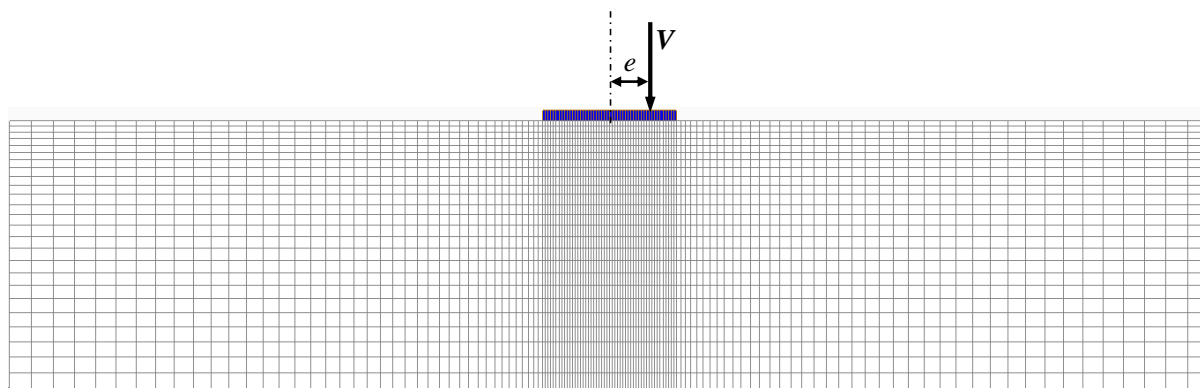
Figure 4.2. Sign convention of eccentric vertical load on a rigid footing

Figure 4.2 shows the sign convention of eccentricity length e for the applying load which is defined as the length from the loading point to the center of the footing. The distributions of contact normal stress σ_n and contact shear stress τ at the footing base, corresponding to normalized distance X/B for which X is the location in the footing from the center of the footing, are plotted in **Figs. 4.3** and **4.4**, respectively. The contact stress is assessed by calculating the interaction force at the nodes of the interface elements. It is seen that, when eccentricity length e increases, the normal stress distribution changes in size and shape for both rough and smooth conditions. It can be observed from **Figs. 4.3 (a)** and **4.3 (b)** that the normal stress for the rough condition is presented as circular shapes, while that for the smooth condition is presented as triangular shapes. In the case of the concentric load ($e= 0.0\ B$), the distribution of normal stress has a symmetric shape in respect to the center of the footing. It is observed that the maximum value is located under the center of the footing. For the eccentricity of $e \geq 0.1B$, part of the footing base achieved zero normal stress; consequently, no force transmission takes place between the contacted surface of the footing-soil. This area of zero normal stress reflects the detachment of the footing and the soil. However, even though the zero normal stress condition is satisfied, it is noted that the footing and the soil are kinematically connected; and therefore, the computed failure mode is slightly unsuitable in the area surrounding the detachment area. However, the shear strength in this area is very small due to the zero-normal-stress condition, and the error in the obtained ultimate bearing capacity is thought to be small. It can be seen that the distribution of normal stress along the footing completely depends on eccentricity length e and the friction condition of the footing-soil surface. Moreover, the distribution of contact shear stress τ, between the footing and the soil for the rough condition, is presented in **Fig. 4.4**. The distribution

of contact shear stress for the smooth condition is observed to be equal to zero stress at the footing base regardless of the change in eccentricity e. **Figure 4.4** shows that eccentricity e varies from 0.0 B to 0.4 B, and that the shear stress also significantly changes in magnitude and shape. The negative and positive signs express the working direction of the shear stress along the footing base. The distribution of shear stress is obtained as zero in the detachment zone and at one point in the part connecting the footing and the soil. The numerical results of the RPFEM show that the effect of the eccentric vertical load on the distribution of contact stress is considerable.

Figure 4.5 shows the failure modes of the ground in the case of normalized eccentricity $e/B = 0.3$ for the rough and smooth conditions. They are nearly similar in shape, but the deformation area in the case of the rough condition is larger and deeper than that in the case of the smooth condition. The failure mechanism was found to be composed of two different zones and similar to the mechanism assumed by Loukidis et al. (2008) and Tang et al. (2014) for the rough condition. From the failure modes, with respect to the friction conditions of the footing surface, the failure domain is concentrated on the edge of the footing as eccentricity length e increases. However, another failure mode forms slightly on the opposite side. It is partly due to the assumption of the small strain theory and no part exists where the normal stress is negative. The effects of the eccentric vertical load and the friction condition on the interaction between the footing and the soil have been clarified.
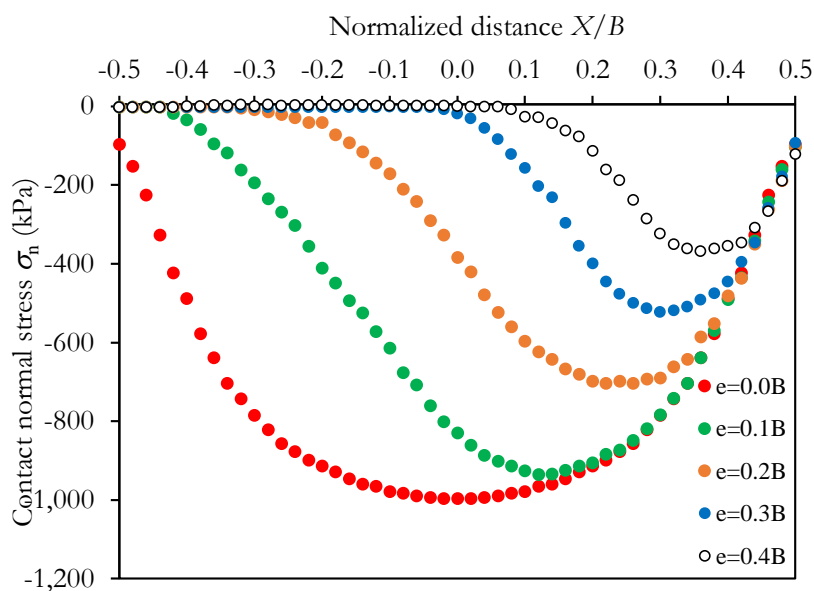
a) Rough condition
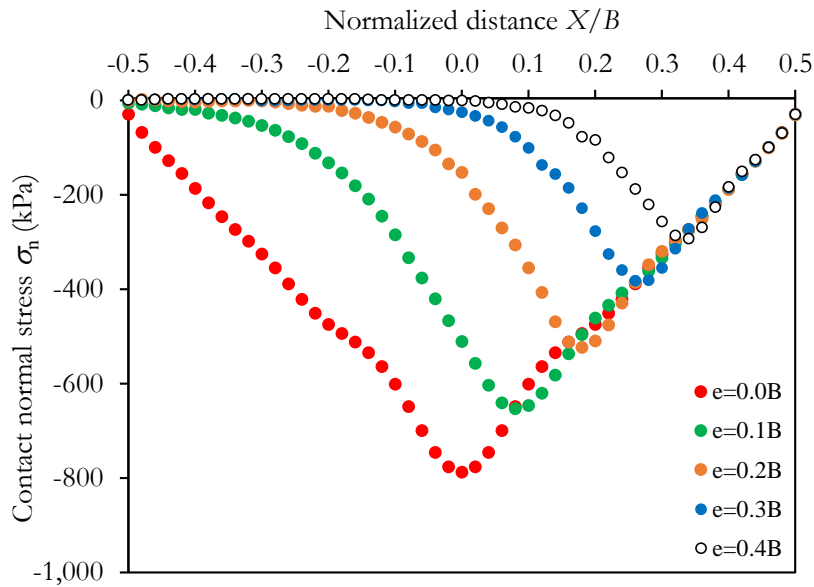
b) Smooth condition

Figure 4.3. Distributions of contact normal stress σ_n acting at footing base on sandy soil of ϕ=30 deg for: (a) rough condition and (b) smooth condition
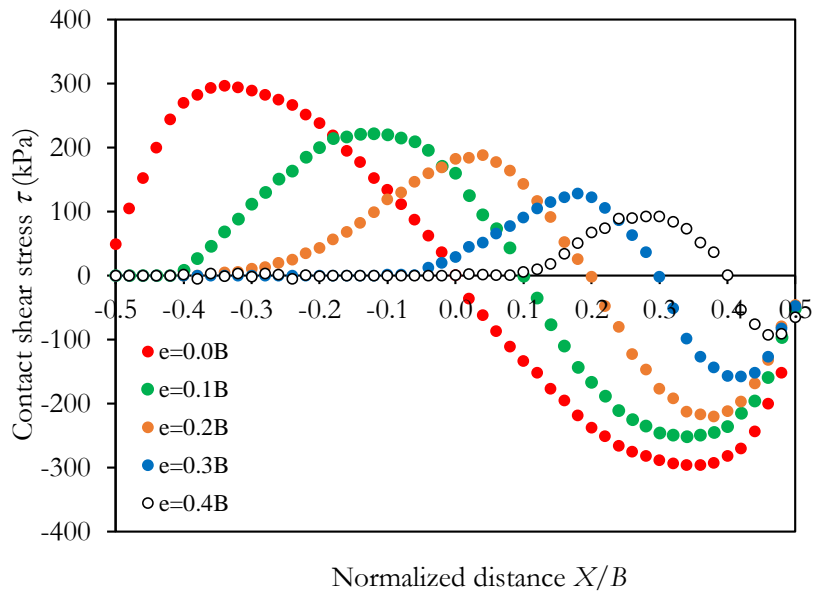
Figure 4.4. Distribution of contact shear stress τ acting at footing base for rough condition on sandy soil of ϕ=30deg.
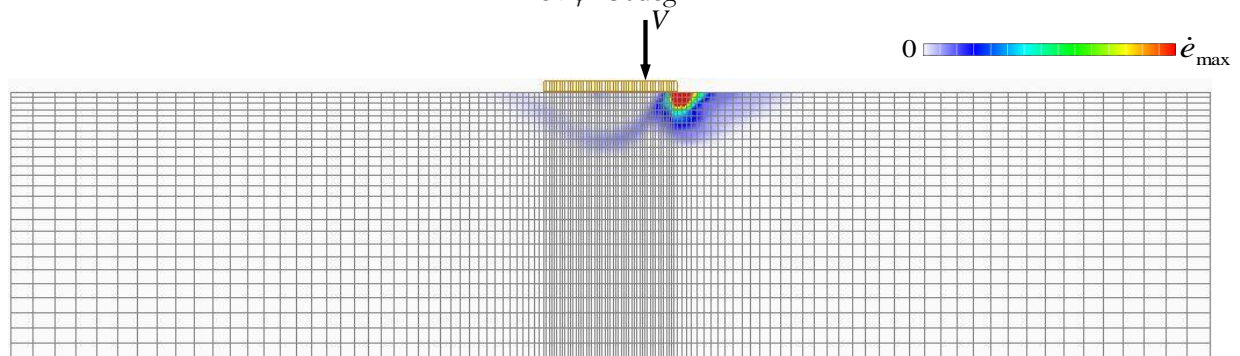
a) Rough condition, e/B=0.3, (V=764 kN/m)
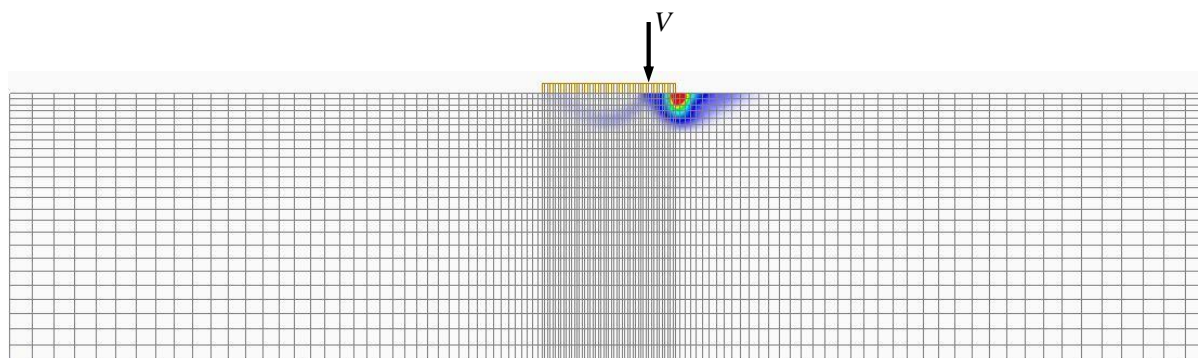
b) Smooth condition, e/B=0.3 (V=415 kN/m)

Figure 4.5. Failure modes of footing against eccentric load for rough and smooth conditions on sandy soil in case of e/B=0.3

4.3.2 Case studies for clayey soil under "rough" contact condition

In the literature on clayey soil, Bransby (2001), Gourvenec (2008) and Khitas et al. (2017) analyzed the ultimate bearing capacity of a footing subjected to an eccentric vertical load for the full tension interface using the finite element method. Their studies showed that the admissible condition is the tension stress occurring in the normal stress component within the limit of shear strength. However, Gourvenec (2007), Rao et al. (2015) and Shen et al. (2016) investigated the ultimate bearing capacity of an eccentrically loaded footing with the condition of zero tension by the finite element method. They reported zero tension stress in the normal stress component of the interaction between the footing and the soil. In this section, the applicability of the interface element to the assessment of the ultimate bearing capacity against the eccentric vertical load is examined in the case of clayey soil. Two friction conditions for the footing base are addressed in this study. One is the rough condition where the cohesive shear strength of the soil is employed as the shear stress of the interface element and the other is the smooth condition where the cohesive shear strength of the interface element is zero. However, another problem arises as to whether the tensile stress in the normal component is allowed in the interface element, as was discussed for sandy soil in the previous section. Thus, a simple case study is firstly conducted in which the rough condition is employed for the interface element. The undrained shear strengths of the soil and the interface element are set as c_u= 50 kPa, ϕ_u= 0 deg and c_s= 50 kPa, ϕ_s= 0 deg, respectively. To discuss the effect of the eccentric load, the distribution of normalized normal stress along the footing base, which is defined for the shear strength, was computed by considering the change in eccentricity length e.
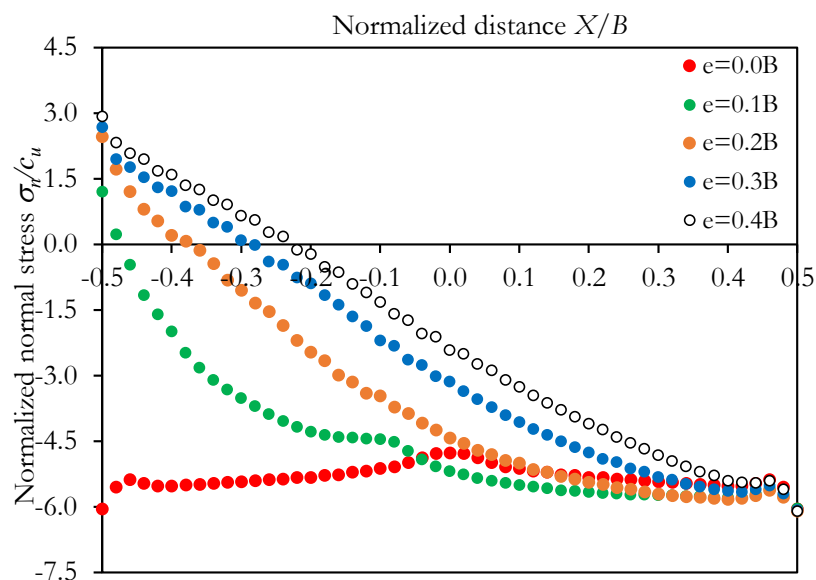
Figure 4.6. Distributions of normalized contact normal stress against eccentricity of load in clayey soils under rough condition of footing surface
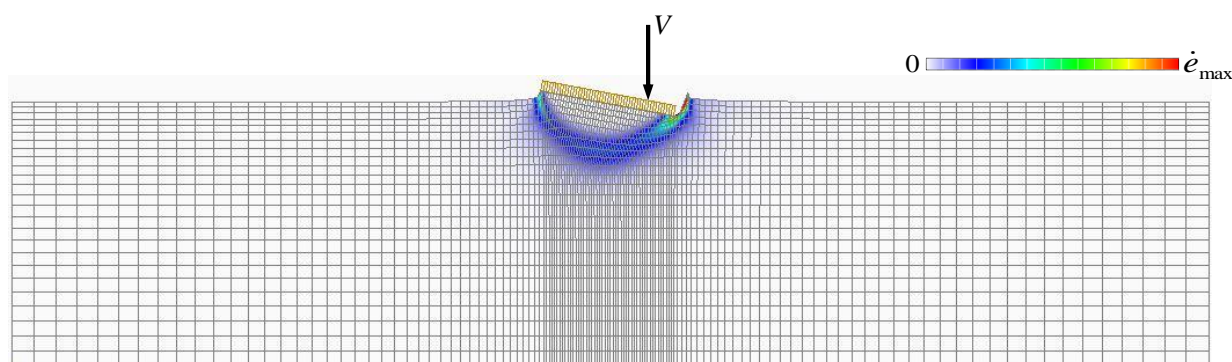
Figure 4.7. Deformation diagram of footing-soil for rough condition (e/B=0.3, clayey soils)

Figure 4.6 shows the distributions of normalized normal stress σ_n/c_u at the footing base for the eccentrcicty e in the range of 0.0 B to 0.4 B. As eccentricity e varies from 0.1 B to 0.4 B, the normal stress of the interface element becomes partly negative around the left edge of the footing. The zone of the interface element where the tension stress exists is seen to increase as eccentricity length e increases. **Figure 4.7** shows the failure mode obtained for e/B=0.3. It expresses the failure mode of a single circular arc slip in spite of the large eccentricity. It is likely to have formed by tension stress at the footing base. In the case of clayey soil, it is apparent that the employment of the interface element with cohesive strength is not effective in the zero-tension analysis for the interaction between the footing and the soil in comparison with the performance in the case of sandy soil.

4.3.3 Zero-tension analysis for clayey soil

The study introduces the zero-tension analysis to investigate the effect of the eccentric vertical load on the interaction between the footing and the soil in clay. The procedure for the zero-tension analysis of the footing-soil interface is shown in **Fig. 4.8**. Here, the detachment of the footing and the soil is introduced into the ultimate bearing capacity analysis. The concept of the detachment is illustrated in **Fig. 4.8 (a)**. In the part where the detachment occurs, the contact normal stress between the footing and the soil is zero, and tension stress is not sustained. In the figure, contact breaking point C expresses the separation point where the footing detaches from the soil surface. In the computation, double nodal points are introduced to the footing-soil interface to model the detached part to which the nodal forces are not transmitted. The analysis is performed according to the flowchart given in **Fig. 4.8 (b)** where the location of the contact breaking point is determined by an iterative process. A series of finite element analyses were conducted under the two friction conditions given in **Table 4.2**.

a) Breaking point for detachment of footing and soil   b) Flowchart for determining contact breaking point C
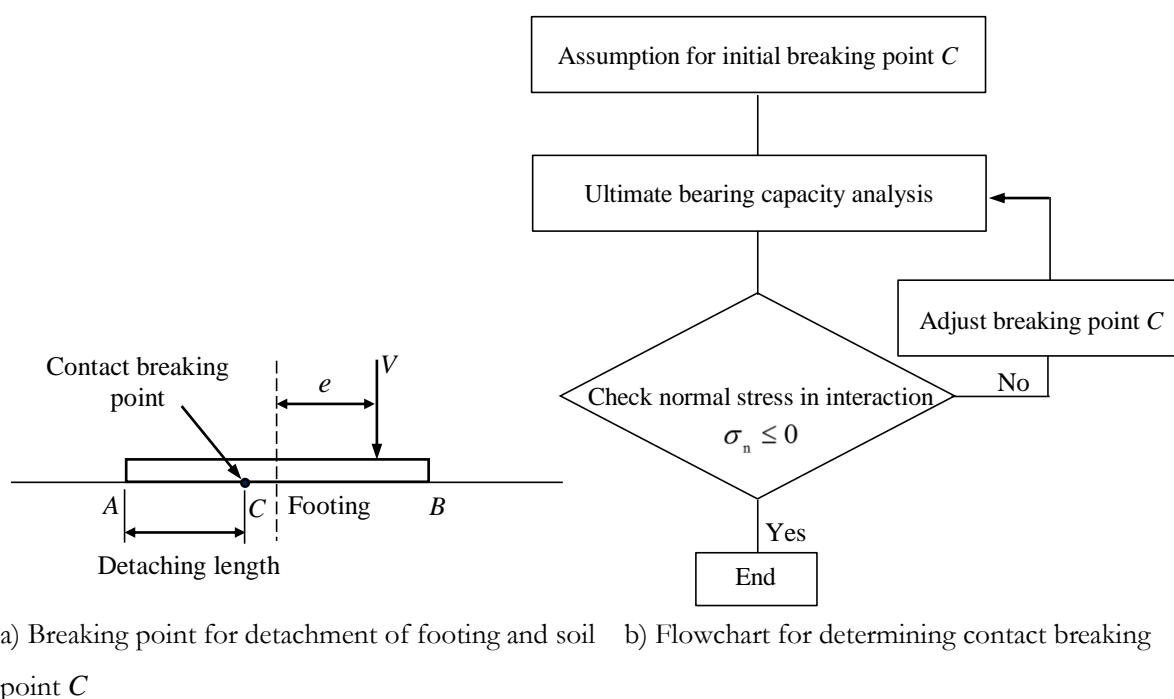
Figure 4.8. Procedure for zero tension analysis

Table 4.2. Interface element properties of clayey soil

Parameter	Rough condition	Smooth condition
Internal friction angle ϕ_s (°)	0	0
Shear strength c_s (kPa)	50	0.5

53
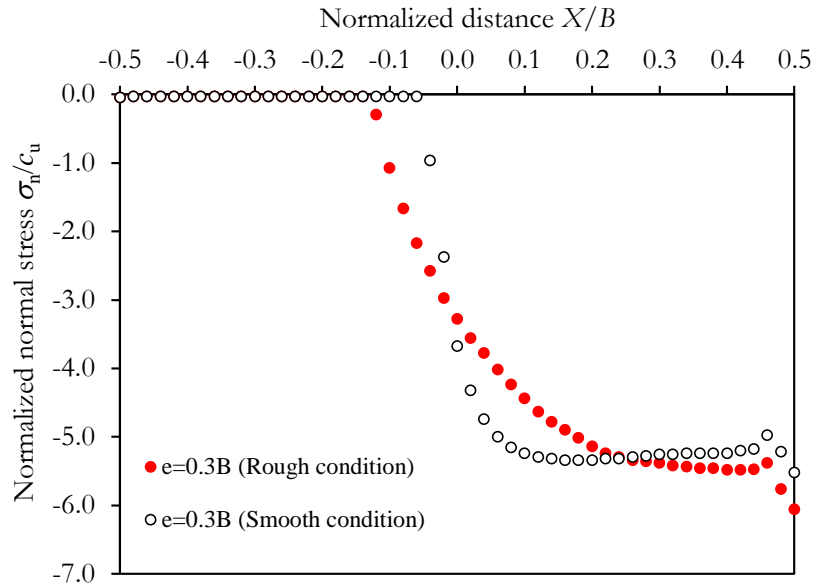
Figure 4.9. Distribution of normalized normal stress σ_n/c_u at footing base for rough and smooth condition in case of $e/B=0.3$

a) $e/B=0.3$, V=$2.39Bc_u$ for rough condition

b) $e/B=0.3$, V=$2.31Bc_u$ for smooth condition
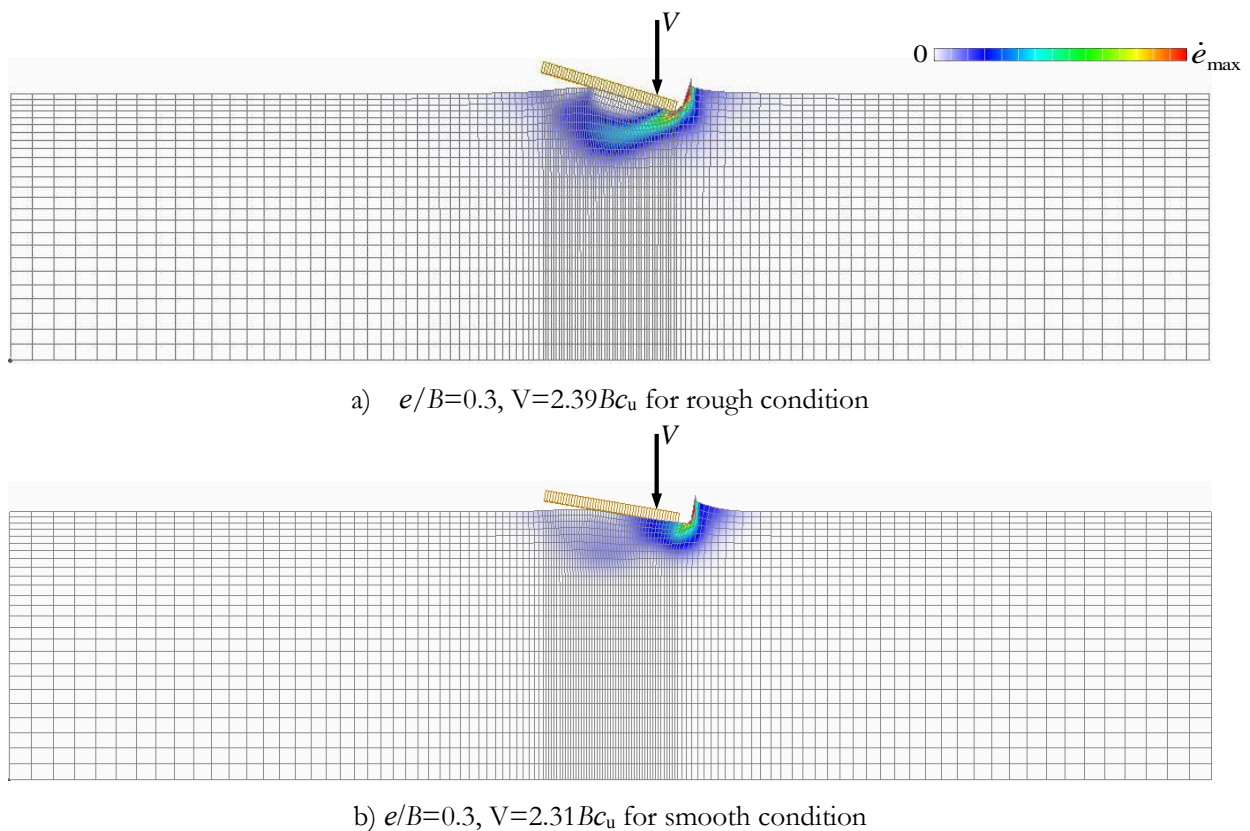
Figure 4.10. Failure modes of footing for rough and smooth condition in case of $e/B=0.3$

The ultimate bearing capacity of the centric vertical load was computed using the RPFEM, with 5.39 Bc_u for the rough condition and 5.22 Bc_u for the smooth condition, in which the ultimate bearing capacity is normalized by the footing width and the undrained shear strength of the soil. The obtained results are

close to the exact results of 5.14 Bc_u by Prandtl (1920), namely, the difference did not exceed 5% and 2% for the rough and smooth conditions, respectively. To obtain a closer solution, the treatment of the singularity in stress at the edge of the footing would be necessary. **Figure 4.9** shows the computation results for the distribution of normalized normal stress in the case of *e/B*=0.3. The figure expresses the distributions of the two friction conditions of the footing-soil interface. In the figure, the normal stress decreased to zero in the vicinity of the left edge of the footing, due to the detachment at the footing-soil interface. It can be seen that the detaching length in the case of the rough condition is shorter than that of the smooth condition. Moreover, the normal stress reaches the maximum value at the right edge of the footing, and the maximum normal stress for the rough condition is little more than that for the smooth condition. This is because the friction condition of the footing surface affects the maximum normal stress. The strain rate distributions of the footing-soil system in the case of *e/B*=0.3 are shown in **Fig. 4.10**. The figure indicates both the distribution of norm in the strain rate and the displacement pattern which is computed from the displacement velocity with arbitrary time increments. The figure expresses the detachment between the footing and the soil that occurred around the left-hand side of the footing. While the failure mode for the rough condition shows a single-sliding mode, that for the smooth condition shows a double-sliding mode reflecting the different footing base friction conditions. Moreover, the ultimate bearing capacity of the rigid footing was obtained as a value close to 2.39 Bc_u for the rough footing and 2.31 Bc_u for the smooth footing. The difference in ultimate bearing capacity due to the footing base friction is not so large. The distributions of normal stress σ_n and shear stress τ at the footing-soil interface for various eccentricity *e* are presented in **Figs. 4.11** and **4.12**, respectively. The distribution of contact normal stress for the rough friction condition is somewhat different from that for the smooth friction condition although the magnitude of the stress is almost the same. For eccentricity *e* varying from 0.1 *B* to 0.4 *B*, the detaching length is seen to increase with eccentricity *e* regardless of the friction condition of the footing surface. While the shear stress for the smooth friction condition is zero, the shear stress for the rough friction condition is symmetric to the center point for the connected part of the footing and the soil, in which the working direction of the shear stress is opposite. As shown by the above-obtained results, the analysis procedure for employing the interface element and the zero-tension analysis is found to be rational

and accurate for assessing both the ultimate bearing capacity and the failure mode of a footing-soil system under an eccentric vertical load.
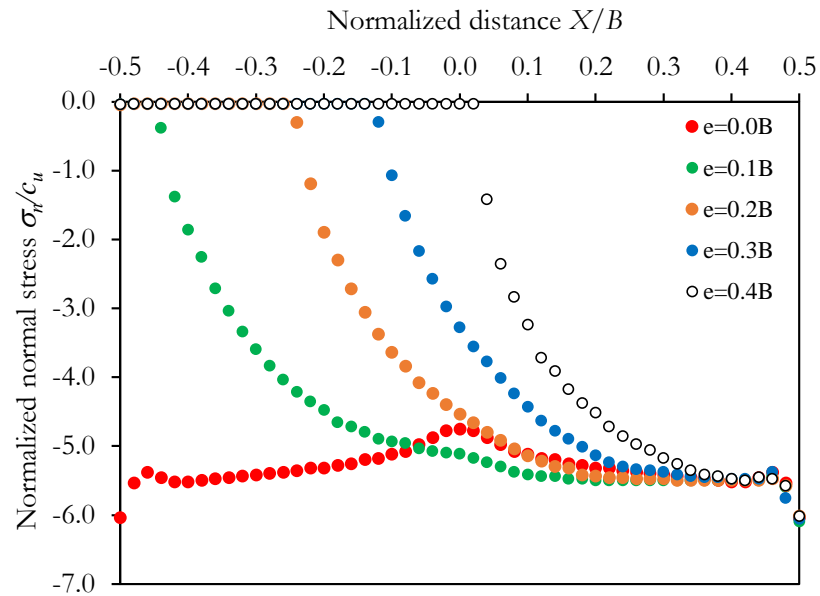
a) Rough condition with zero-tension analysis
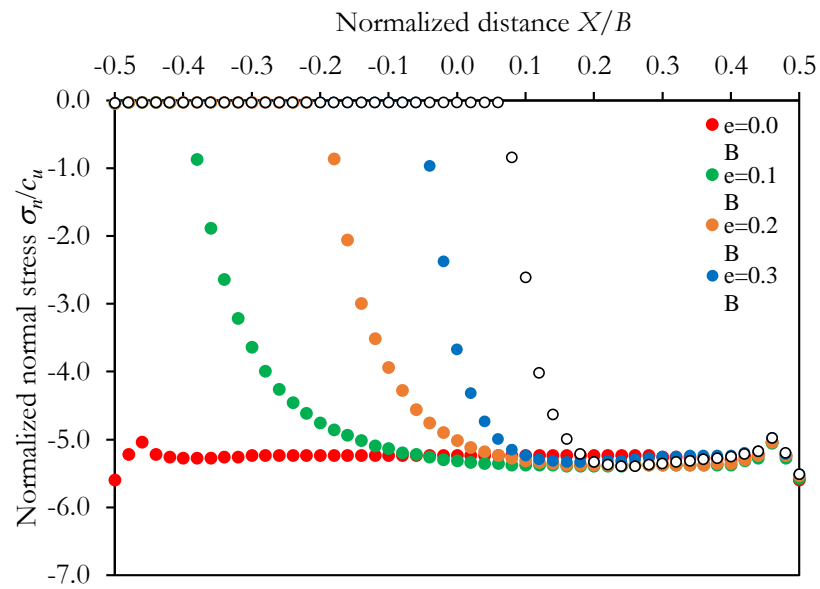
b) Smooth condition with zero-tension analysis

Figure 4.11. Distributions of normalized normal stress σ_n/c_u at footing base with zero-tension analysis for: a)rough condition and b) smooth condition
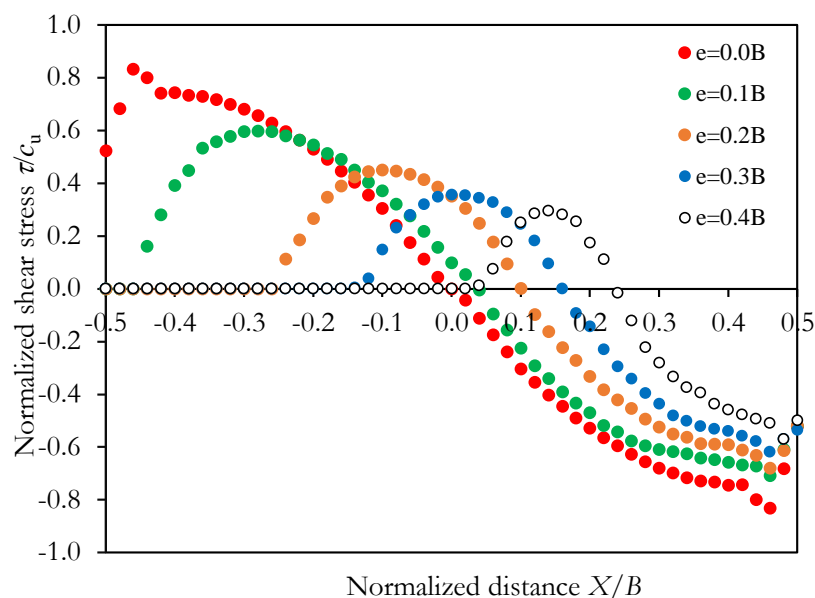
Figure 4.12. Distributions of normalized shear stress τ/c_u at footing base with zero-tension analysis for rough condition

4.4 ULTIMATE BEARING CAPACITY OF FOOTING UNDER ECCENTRIC VERTICAL LOAD

4.4.1 Normalized limit load space for sandy soil

Loukidis et al. (2008), Krabbenhoft et al. (2012) and Tang et al. (2014) analyzed the failure envelope in the V-M plane of a footing subjected to an eccentric vertical load using the finite element method. They reported the normalized limit load space in the V-M plane for the rough condition. The present study investigates this failure envelope in the V-M plane under two friction conditions on the footing base for various internal friction angles of the soil. As was mentioned in the previous chapter, the cohesion (c=0.5 kN/m²) is introduced into the shear strength parameter of the soil to stabilize the computation process, since it was determined not to greatly affect the ultimate bearing capacity.

Meyerhof (1953) proposed the effective width method to use the ultimate bearing capacity formula for assessing the ultimate bearing capacity of a footing under an eccentric vertical load based on his experimental study.

$$V = \frac{1}{2}\gamma B'^2 N_\gamma \quad \text{with} \left(B' = B - 2e \right) \tag{2}$$

Regarding the N_γ factor, several formulations have been proposed based mainly on either the theoretical methods or numerical computations. The formula proposed by Meyerhof (1963) is well known and

expressed as follows:

$$N_\gamma = \left(e^{\pi \tan\phi} \tan^2\left(\frac{\pi}{4} + \frac{\phi}{2}\right) - 1 \right) \tan\left(1.4\phi\right) \qquad (3)$$

where, B' is the effective width proposed by Meyerhof. It is widely used in practice, but its applicability has not been clarified. This is because the effective width method assumes similar interaction to that which is used for the centric vertical load, while the interaction for the eccentric vertical load is originally different due to the eccentricity shown in **Figs. 4.11** and **4.12** in spite of the fact that the focus is placed on the contact part. Although many studies have been conducted on this issue, a comprehensive understanding of the applicability of the effective width method has not been established yet based on a reliable analysis method. This study examines the applicability of the effective width method to the assessment of the ultimate bearing capacity of a footing under an eccentric vertical load and additionally examines the applicability of the failure envelope in the V-M plane to the assessment of the ultimate bearing capacity for complex loads in which V and M are independently varied.
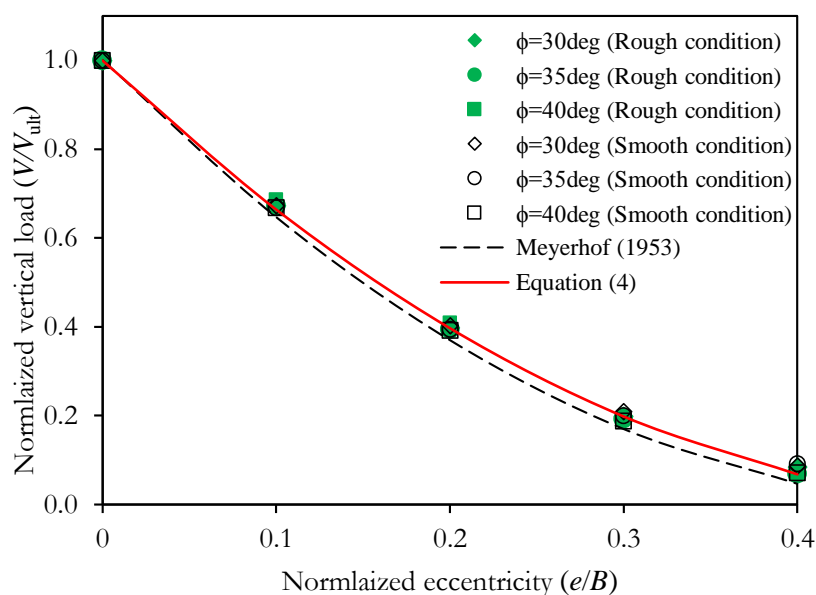
Figure 4.13. Effect of internal friction angle on relationship between normalized vertical load V/V_{ult} and normalized eccentricity e/B in case of rough condition and smooth condition
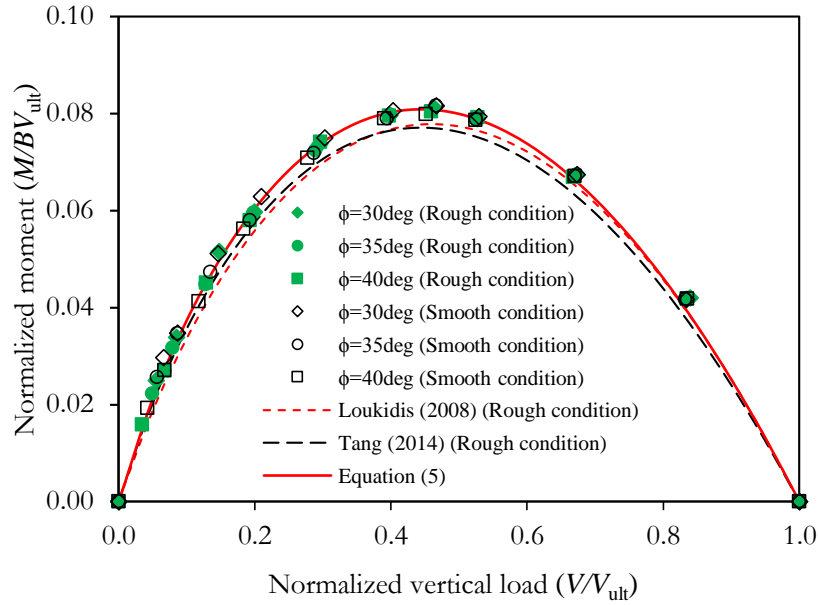
Figure 4.14. Effect of internal friction angle on failure envelope in *V-M* plane in case of rough condition and smooth condition

Figure 4.13 presents the effect of eccentricity *e* on normalized vertical load V/V_{ult}, where V_{ult} is the ultimate bearing capacity computed for the centric vertical load. In the figure, the friction angle of the soil is varied widely. The normalized vertical load is seen to decrease proportionally as normalized eccentricity *e/B* increases. It is interesting that the trend in the decrease in normalized ultimate bearing capacity V/V_{ult} against normalized eccentricity *e/B* is unique for any internal friction angle regardless of the rough or smooth condition. Loukidis et al. (2008) reported that the normalized ultimate bearing capacity in sandy soil subjected to an eccentric vertical load was almost the same as that of the effective width method up to normalized eccentricity of *e/B*= 0.3. However, the results obtained with the RPFEM are seen to closely match those obtained with the effective width method for any eccentricity length *e*. Thus, the normalized ultimate bearing capacity for the eccentric vertical load can be expressed by the following equation with any internal friction angle:

$$\frac{V}{V_{ult}} = \left(1 - 1.85 \frac{e}{B}\right)^2 \tag{4}$$

Figure 4.14 shows the failure envelope in the *V-M* plane for an increase in eccentricity *e*. It is interesting that the failure envelope in the *V-M* plane is also obtained uniquely for the internal friction angle of soil. For the rough condition, the M_{max} reached approximately 0.0807 BV_{ult} at a normalized eccentricity of

around $e/B = 0.165$. Similarly, Loukidis et al. (2008) reported that the M_{max} reached 0.078 BV_{ult}, while Tang et al. (2014) reported that it reached 0.076 BV_{ult} at e/B of around 1/6. Moreover, Georgiadis et al. (1988), Gottardi et al. (1993) and Okamura et al. (2002) conducted model tests and concluded that the value of M_{max} was in the range of 0.075 BV_{ult} to 0.1 BV_{ult}. From a comparison with past works, it can be concluded that the RPFEM generates good estimations under the rough condition of the footing base. For the smooth condition, the failure envelope in the V-M plane is obtained in a similar manner to that for the rough condition. It is also found to be unique for the internal friction angle, for which the M_{max} was approximately equal to 0.0811 BV_{ult} at the normalized eccentricity of around $e/B = 0.165$.

After the past works by Meyerhof (1953), Loukidis et al. (2008) and Tang et al. (2014), the failure envelope in the V-M plane is derived based on the results computed with the RPFEM, as seen in Fig. 15.

$$\frac{M}{BV_{ult}} = 0.55 \frac{V}{V_{ult}} \left(1 - \left(\frac{V}{V_{ult}} \right)^{0.49} \right) \tag{5}$$

4.4.2 Normalized limit load space for clayey soil using zero-tension analysis

Taiebat et al. (2002), Gourvenec (2007), Rao et al. (2015) and Shen et al. (2016) used the zero-tension interface to analyze the ultimate bearing capacity of a rigid footing subjected to eccentric loading for the rough condition. However, there are few works which have analyzed for the smooth condition. This study applied a zero-tension analysis to calculate the normalized limit load plane for two friction conditions of the footing base. The obtained results are also compared with those of the effective width method. The equation used with the effective width method for assessing the ultimate bearing capacity in clayey soil was expressed by Meyerhof as follows:

$$V = c_u N_c B' \qquad \text{with } \left(B' = B - 2e \right) \tag{6}$$

where, c_u is the undrained shear strength of the clayey soil. **Figure 4.15** shows the normalized vertical load V/V_{ult} and the normalized eccentricity e/B relationship for the rough and smooth conditions. The figure indicates that the friction conditions of the footing surface did not influence the V/V_{ult} and e/B relationship. Moreover, normalized vertical load V/V_{ult} shows a good agreement with the effective width method in the range of eccentricity e from 0.0 B to 0.2 B. However, when eccentricity e is more than 0.2 B,

the difference becomes greater. Michalowski and You (1998) examined the effective width method in cohesive soil using the kinematic approach of the limit analysis. They found that it overestimated by about 35% in comparison to the ultimate bearing capacity determined by Meyerhof's method at e/B = 0.25. This study proposes the following new equation to determine the normalized vertical load in clay:

$$\frac{V}{V_{\text{ult}}} = 1 - 1.85 \frac{e}{B} \tag{7}$$
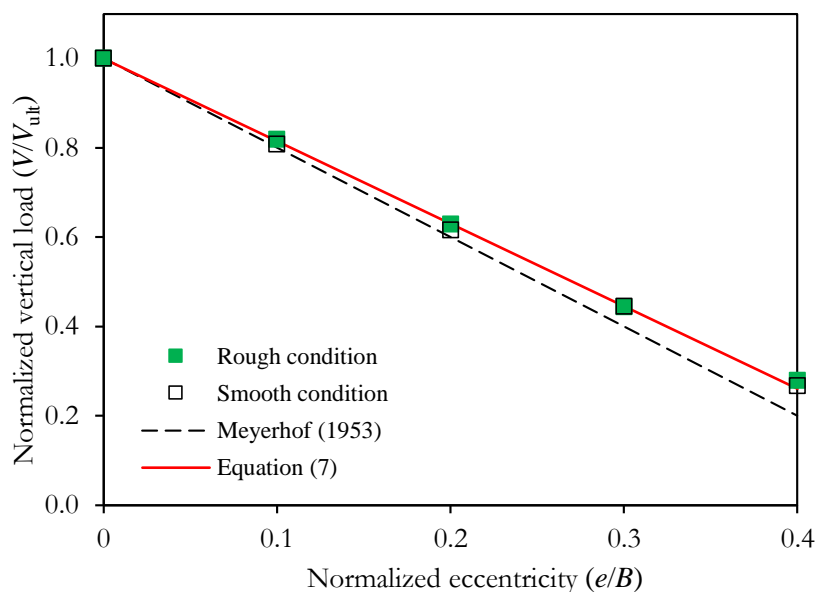
Figure 4.15. Relationship between normalized vertical load V/V_{ult} and normalized eccentricity e/B for rough and smooth conditions
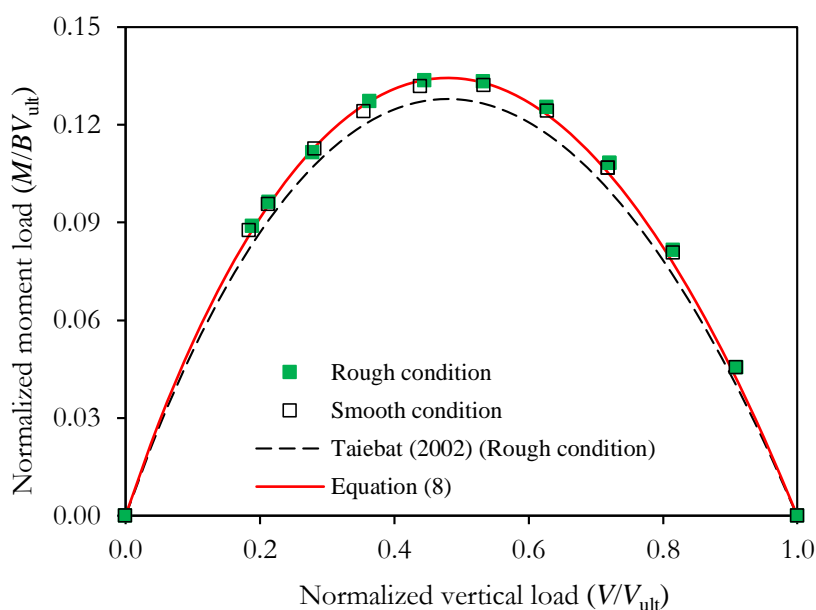
Figure 4.16. Failure envelope in V-M plane against eccentric vertical load on clayey soil

61

In addition, Taiebat et al. (2002), Rao et al. (2015), Shen et al. (2016) and Khitas et al. (2017) reported a calculation for the failure envelope in the V-M plane under the eccentric vertical load for the rough condition. **Figure 4.16** presents the failure envelope in the normalized form by M/BV_{ult} and V/V_{ult} for both rough and smooth conditions. At the limit of a zero vertical load, the moment load was not sustained. It can be seen that the failure envelope in the V-M plane in clay was independent of the friction condition of the footing surface in the same way as that for sandy soil. The maximum moment capacity reached nearly 0.132 BV_{ult} at $V/V_{ult} = 0.5$. The failure envelope by the RPFEM is in excellence accordance with that by Taiebet et al. (2002). This study proposes the following new equation for the normalized V-M failure envelope of the RPFEM for both rough and smooth conditions:

$$\frac{M}{BV_{ult}} = 0.63\frac{V}{V_{ult}}\left(1 - \left(\frac{V}{V_{ult}}\right)^{0.8}\right) \tag{8}$$

4.5 APPLICABILITY OF NORMALIZED LIMIT LOAD PLANE OF VERTICAL AND MOMENT LOADS

It is questionable whether the failure envelope in the V-M plane for the eccentric vertical load is applicable to combined loads of V and M which are independent variables. This is because once the failure envelope in the V-M plane is proposed, it is possible to apply it to the assessment of the ultimate bearing capacity for combined loads of V and M. However, the applicability of this failure envelope is not clear since it was originally developed for the eccentric vertical load which is connected to the moment load. In this study, the moment load is replaced by a triangular distributed load the summation of which is zero in vertical load, as shown in **Fig. 4.17**, in order to handle the vertical load and the moment load independently. Moment capacity M_{ult} is basically unknown and it was determined through a computation process under prescribed vertical load V. The failure envelope in the V-M plane for the combined load is systematically investigated under two friction conditions for the footing surface, namely, rough and smooth. In the study, a series of analyses was conducted for case of sandy soil of $\phi = 30$ deg and clayey soil of c_u=50 kPa with a zero-tension analysis. The properties of the interface element corresponding to the sandy and clayey soils are given in **Tables 4.1** and **4.2**, respectively.
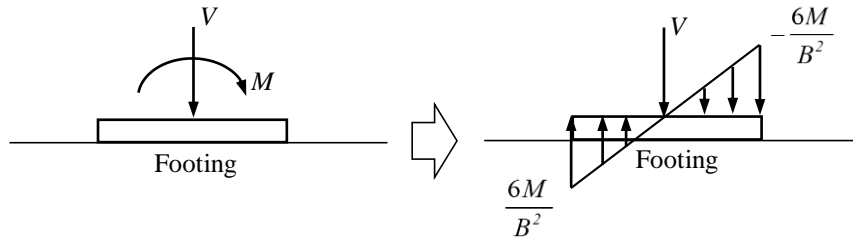
Figure 4.17. Initial load conditions for rigid plastic FEM

Figure 4.18 shows the ultimate bearing capacity of a footing in the normalized V-M plane on the sandy and clayey soils for rough and smooth conditions. The figure demonstrates that the failure envelope for the combined load is almost similar in shape and magnitude to the two friction conditions regardless of the different types of soil. For the sandy soil, maximum moment capacity M_{max}, reflecting the rough and smooth conditions, generally achieved a value of 0.081 BV_{ult} at a vertical load of around 0.46 V_{ult}. For the clayey soil, on the other hand, the failure envelope was observed symmetrically in respect to the vertical load of around 0.5 V_{ult} and the maximum moment capacity M_{max} achieved a value of nearly 0.133 BV_{ult}, which is equally 1.64 times the value for sandy soil. It is interesting that the envelope in the normalized V-M plane in the case of a combination of the centric vertical load and the moment load almost coincides with the equation for the V-M plane under the eccentric vertical load, as shown in **Fig. 4.18**.
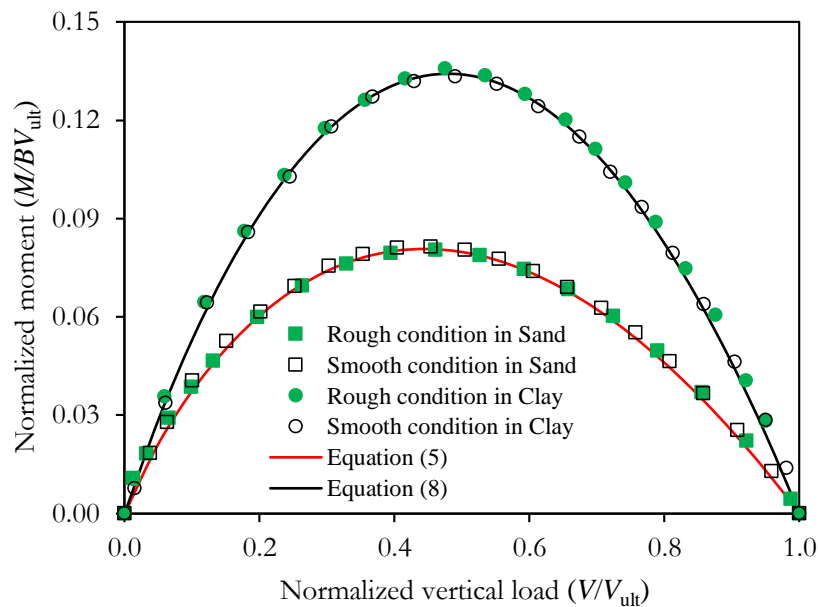
Figure 4.18. Failure envelope in V-M plane against combination of centric vertical and moment loads for sandy and clay soils under two friction conditions

63

4.5. CONCLUSION

This study has investigated the ultimate bearing capacity of an eccentrically loaded footing on sandy and clayey soils using the rigid plastic finite element method (RPFEM). The effect of the eccentric vertical load on the ultimate bearing capacity and the failure mechanism was analyzed for changes in the eccentricity length.

The conclusions of this study are as follows:

1. The ultimate bearing capacity of the rigid footing was analyzed against the eccentric vertical load using an interface element. A zero-tension analysis was employed to simulate the behavior of the contact footing-soil plane in clay validating that the method was effective for analyzing the interaction between the footing and the soil. The effect of the friction condition of the footing surface was found to reflect the failure mode of the footing-soil system. The failure mechanism of the footing generally changed depending on the different friction conditions. This failure mechanism has been verified with that discussed in past works.

2. The effect of the eccentricity length on the shape and size of the contact stress distribution between the footing and the soils was clarified. Regarding the sandy soil, as well as the clayey soil, the contact stress distribution was assessed by considering the friction condition of the footing surface. For each case, the detachment of the footing from the soil surface in the case of large eccentric loading was effectively captured.

3. The study examined the decrease in the normalized vertical load of the eccentrically loaded footing. The numerical results of the RPFEM showed a good agreement with the results obtained by the effective width method experimentally proposed by Meyerhof (1953) especially in the case of sandy soil. Some difference was observed at large eccentricity in the case of clayey soil. New equations were proposed to determine normalized vertical load V/V_{ult}.

4. Normalized vertical load V/V_{ult} and the failure envelope in the V-M plane of the eccentrically loaded footing were uniquely obtained in the case of sandy soil independent of the value of the internal friction angle. They were also observed to be unique in the case of clayey soil independent of the value of the cohesive strength. It is noted that they were coincident between two friction conditions of footing roughness in both sandy and clayey soils.

5. The study considered the impact of the combination of the centric vertical and moment loads on the failure envelope in the *V-M* plane. The results show that the shape and size of the failure envelope in the *V-M* plane in the case of a combined load was completely similar to the eccentric vertical load. In the numerical analysis, it was possible to simulate the eccentric vertical load by the combination of the centric vertical and moment loads.

✧ **Publication:** Chapter 4 is published as article: **Pham, N. Quang**, Ohtsuka, S., Isobe, K. and Fukumoto, Y., Hoshina, T.: Ultimate bearing capacity of rigid footing under eccentric vertical load, **Soils and Foundations**, 2019. 59 (6), 1980-1991. DOI: https://doi.org/10.1016/j.sandf.2019.09.004.

References

Asaoka, A., and Ohtsuka, S., 1986. The analysis of failure of a normally consolidated clay foundation under embankment loading. Soils and Foundations. 26(2), 47-59.

Asaoka, A., and Ohtsuka, S., 1987. Bearing capacity analysis of a normally consolidated clay foundation. Soils and Foundations. 27(3), 58-70.

Asaoka, A., Ohtsuka, S., and Matsuo, M., 1990. Coupling analyses of limiting equilibrium state for normally consolidated and lightly overconsolidated soils. Soils and Foundations. 30(3), 109-123.

Fraser Bransby, M., 2001. Failure envelopes and plastic potentials for eccentrically loaded surface footings on undrained soil. International Journal for Numerical and Analytical Methods in Geomechanics. 25(4), 329-346.

Georgiadis, M., and Butterfield, R., 1988. Displacements of footings on sand under eccentric and inclined loads. Canadian Geotechnical Journal. 25(2), 199-212.

Gottardi, G., and Butterfield, R., 1993. On the bearing capacity of surface footings on sand under general planar loads. Soils and Foundations. 33(3), 68-79.

Gourvenec, S., Randolph, M., & Kingsnorth, O., 2006. Undrained bearing capacity of square and rectangular footings. International Journal of Geomechanics. 6(3), 147-157.

Gourvenec, S., 2007. Failure envelopes for offshore shallow foundations under general loading. Géotechnique. 57(9), 715-728.

Gourvenec, S., 2008. Effect of embedment on the undrained capacity of shallow foundations under general loading. Géotechnique. 58(3), 177-186.

Guetari, A., Benmebarek, S. and Saddek, R.M., 2018. Effect of the eccentric load on the bearing capacity of a strip footing founded on sand. Journal of Applied Engineering Science & Technology. 4(2), 171-176.

Hoshina, T., Ohtsuka, S., and Isobe, K., 2011. Rigid plastic analysis for slope including thin weak layer. Geotechnical Journal. 6, 191-200 (in Japanese).

Krabbenhoft, S., Damkilde, L., and Krabbenhoft, K., 2012. Lower-bound calculations of the bearing capacity of eccentrically loaded footings in cohesionless soil. Canadian Geotechnical Journal. 49(3), 298-310.

Khitas, N.E.H., Benmeddour, D., Mellas, M. and Mabrouki, A., 2017. The undrained bearing capacity of strip footings under eccentric loading: effect of soil-footing interface tensile strength. International Journal of Geotechnical Engineering. 1-7.

Loukidis, D., Chakraborty, T. and Salgado, R., 2008. Bearing capacity of strip footings on purely frictional soil under eccentric and inclined loads. Canadian Geotechnical Journal. 45(6), 768-787.

Loukidis, D., and Salgado, R., 2009. Bearing capacity of strip and circular footings in sand using finite elements. Computers and Geotechnics. 36(5), 871-879.

Meyerhof, G.G., 1953. The bearing capacity of foundations under eccentric and inclined loads. In Proc. of the 3rd Int. Conf. on SMFE (Vol. 1, 440-445).

Meyerhof, G. G., 1963. Some recent research on the bearing capacity of foundations. Canadian Geotechnical Journal. 1(1), 16-26.

Michalowski, R.L. and You, L., 1998. Effective width rule in calculations of bearing capacity of shallow footings. Computers and Geotechnics. 23(4), 237-253.

Nguyen, D. L., Ohtsuka, S., Hoshina, T., and Isobe, K., 2016. Discussion on size effect of footing in ultimate bearing capacity of sandy soil using rigid plastic finite element method. Soils and Foundations. 56(1), 93-103.

Okamura, M., Mihara, A., Takemura, J., and Kuwano, J., 2002. Effects of footing size and aspect ratio on the bearing capacity of sand subjected to eccentric loading. Soils and Foundations. 42(4), 43-56.

Pham, Q. N., Ohtsuka, S., Isobe, K., & Fukumoto, Y., 2019. Group effect on ultimate lateral resistance of piles against uniform ground movement. Soils and Foundations. 59(1), 27-40.

Prakash, S. and Saran, S., 1971. Bearing capacity of eccentrically loaded footings. Journal of Soil Mechanics & Foundations Div. 97(1), 95-117.

Prandtl, L., 1920. Über die härte plastischer körper. Nachrichten von der Gesellschaft der Wissenschaften zu Göttingen, Mathematisch-Physikalische Klasse. 1920, 74-85.

Rao, P., Liu, Y. and Cui, J., 2015. Bearing capacity of strip footings on two-layered clay under combined loading. Computers and Geotechnics. 69, 210-218.

Salençon, J., Pecker, A., 1995. Ultimate bearing capacity of shallow foundations under inclined and eccentric loads. Part II: purely cohesive soils without tensile strength. Europ. J. Mechanics A/Solids. 14, 377-396

Shen, Z., Feng, X., and Gourvenec, S., 2016. Undrained capacity of surface foundations with zero-tension interface under planar VHM loading. Computers and Geotechnics. 73, 47-57.

Taiebat, H. A., & Carter, J. P., 2002. Bearing capacity of strip and circular foundations on undrained clay subjected to eccentric loads. Geotechnique. 52(1), 61-64.

Tamura, T., Kobayashi, S. and Sumi, T., 1984. Limit analysis of soil structure by rigid plastic finite element method. Soils and Foundations. 24 (1), 34-42.

Tamura, T., Kobayashi, S. and Sumi, T., 1987. Rigid Plastic Finite Element Method for Frictional Materials. Soils and Foundations. 27 (3), 1-12.

Tamura, T., Kobayashi, S. and Sumi, T., 1990. Rigid Plastic Finite Element Method in Geotechnical Engineering Computational. Current Japanese Material Research. 15-23.

Tang, C., Phoon, K. K., and Toh, K. C., 2014. Effect of footing width on Nγ and failure envelope of eccentrically and obliquely loaded strip footings on sand. Canadian Geotechnical Journal. 52(6), 694-707.

Terzaghi, K., 1943. Theoretical soil mechanics. Wiley, New York.

Yahia-Cherif, H., Mabrouki, A., Benmeddour, D., and Mellas, M., 2017. Bearing capacity of embedded strip footings on cohesionless soil under vertical and horizontal loads. Geotechnical and Geological Engineering. 35(2), 547-558.

Zadroga, B., 1994. Bearing capacity of shallow foundations on noncohesive soils. Journal of Geotechnical Engineering. 120(11), 1991-2008.

Chapter 5

LIMIT LOAD SPACE OF RIGID FOOTING UNDER ECCENTRICALLY INCLINED LOAD

5. 1 INTRODUCTION

The bearing capacity q of a rigid footing subjected to an inclined load is commonly calculated through the use of multiplicative modification factors. Meyerhof (1951, 1963) introduced some factors for a rigid footing under an inclined load, namely, semi-empirical inclination factors i_c, i_γ, and i_q. The ultimate bearing capacity formula is described as follows:

$$q = i_c c N_c + \frac{1}{2} i_\gamma \gamma B N_\gamma + i_q \gamma D_f N_q \tag{1}$$

where N_c, N_q, and N_γ are the bearing capacity factors which show the effects of soil cohesion c (kN/m²), deep surcharge D_f (m), and soil unit weight γ (kN/m³), respectively. These factors are the functions of the internal friction angle of the soil, ϕ, under the footing. B is the width of the footing (m). Load inclination factors i_c, i_γ, and i_q are also the functions of internal friction angle ϕ and inclination angle α, where α is the inclination angle of the load with respect to the vertical plane. Moreover, a division of both sides of Eq. (1) by soil cohesion c, the non-dimensionalized ultimate bearing capacity of the footing (q/c) depends on soil weight parameter $G=\gamma B/2c$. Chen (1975) mentioned that if G is small, the soil behaves essentially as a cohesive weightless medium. On the other hand, if G is large, the soil weight, rather than cohesion, is the principal source of the bearing strength. Numerical results are presented for G lying within the range of $0 \le G \le 10$.

In practice, rigid footings are subjected to eccentric-inclined coupled loads. Therefore, the stability of a rigid footing on the free surface of soils under complex loading is of practical interest. Meyerhof (1951, 1963), Hansen (1961, 1970), and Vesic (1973, 1975) produced series of model tests to propose empirical and semi-empirical inclination factors. However, the applicability of these inclination factors has not been clarified due to the lack of a systematic analysis based on a reliable stability method. Therefore, the validity of the current design methods needs to be verified by applying load inclination factor formulas for i_c and

i_γ. In recent years, the effect of eccentrically inclined loads on the ultimate bearing capacity has been investigated by several researchers using numerical analyses and model tests. Loukidis et al. (2008), Krabbenhoft et al. (2013), Tang et al. (2014), and Yahia-Cherif et al. (2017) used numerical analyses to calculate the ultimate bearing capacity under eccentrically inclined loads on sandy soil. Georgiadis (2010), Rao et al. (2015), and Shen et al. (2016) reported the effect of eccentrically inclined loads on clayey soil on the ultimate bearing capacity by the finite element method. From the numerical results, it was concluded that the ultimate bearing capacity was significantly changed by the increase in load inclination angle α. The same results were also obtained from model tests conducted by Patra et al. (2012a, 2012b), Ornek (2014), and Cocjin et al. (2013). Although many works have been performed to investigate the ultimate bearing capacity under eccentrically inclined loads, a comprehensive understanding of both the failure mechanism of the footing-soil system and the failure envelopes in the vertical load - horizontal load – moment (*V-H-M*) space has not yet been established.

In the footing-soil system, the ultimate bearing capacity of the footing depends exclusively on the friction condition of the footing base. This study models the footing base under rigid and rough conditions, as it most often exists in reality, especially in the case of horizontal loads. Pham et al. (2019) studied the effect of eccentric vertical loads on the ultimate bearing capacity of rigid footings on uniform sandy and clayey soils using the finite element method. For sandy soil, they introduced an interface element into the footing-soil system in order to properly evaluate the interaction between the footing and the soil. For clayey soil, in particular, they introduced a no tensile strength analysis into the footing-soil system to assess the ultimate bearing capacity of the eccentrically loaded footing. They found that the application of an interface element and a no tensile strength analysis were effective for determining the ultimate bearing capacity of a rigid footing and the failure mechanism of the footing. In the present study, the interface element and a no tensile strength analysis are employed to widely investigate the bearing capacity of an eccentrically inclined loaded footing. The footing-soil system with a two-dimensional analysis is simulated using the rigid plastic finite element method (RPFEM). The RPFEM has been applied in geotechnical engineering by Tamura et al. (1984, 1990) and Asaoka et al. (1986, 1987, and 1990), and was further developed by Tamura et al. (1987) for friction material. Hoshina et al. (2011) introduced a new constitutive equation for solid elements to simulate the footing and the soil, and for interface elements to simulate the interface plane between the

footing and the soil. This method is based on the upper bound theorem in the limit analysis.

a) Positive horizontal load (+H)   b) Negative horizontal load H (-H)
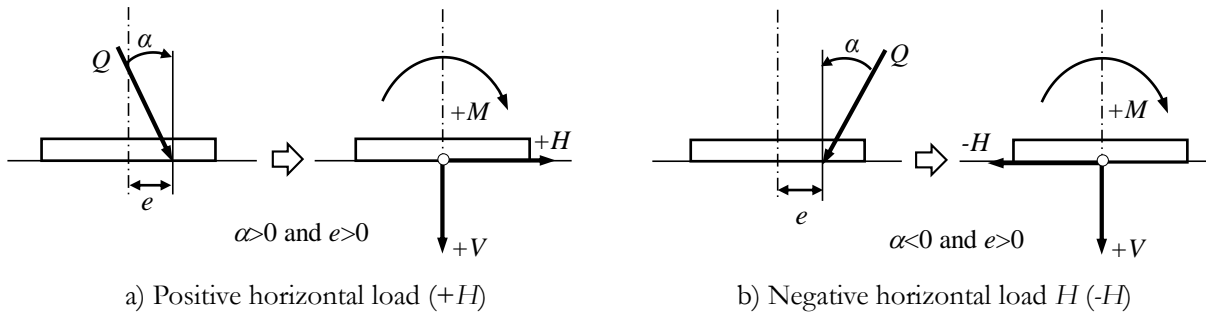
Figure 5.1. Sign convention for positive and negative combinations of H and M

In addition, most of the previous studies, such as those by Loukidis et al. (2008), Krabbenhoft et al. (2013), and Shen et al. (2016), investigated the bearing capacity of eccentrically inclined loaded footings without considering the effect of the direction of the horizontal loads on the failure envelopes in the V-H-M space or the failure mechanism of the footing-soil system. Their findings raise a question as to whether the direction of the horizontal loads has an effect on the ultimate bearing capacity and the failure mechanism in the presence of eccentrically inclined loading. The focus is placed here on the ultimate bearing capacity of a footing against the action of eccentric and inclined loading taking into account the direction of the horizontal loads. The sign convention for the eccentrically inclined loading in this study, based on the one suggested by Butterfield et al. (1997), is shown in **Fig. 5.1**. The combined loading on the rigid footing can be represented by a resultant load Q at eccentricity e and inclination angle α which is divided into three statically equivalent loads, namely, V, H, and M. Moment load M is positive when acting clockwise and horizontal load H is positive in the positive direction of the x-axis. Inclination angle α is positive when acting counterclockwise. The objective of this study is to determine the failure envelopes in the V-H-M space. As shown in **Fig. 5.1**, the failure envelope of (V, H, M) is similar to that of (V, -H, -M), and the failure envelope of (V, -H, M) is similar to that of (V, H, -M), due to the symmetry of the problem. Thus, this study only considers positive eccentricity e (corresponding to M>0), while the direction of the horizontal loads should be considered for both positive and negative loads. For these purposes, load inclination factor i_γ is reported in the results as a function of the friction angle of the soil, while the failure envelopes in the V-H-M space are reported as equations of an ellipse depending on the positive and negative directions of the horizontal loads. The failure envelopes in the V-H-M space are further investigated for

two problems in which the loading paths are different, and the moment component is the independently prescribed moment with vertical and horizontal loads.

5.2 ULTIMATE BEARING CAPACITY FOR INCLINED CENTRAL LOAD

5.2.1 Case studies for sandy soil

As was mentioned in the Introduction, this study introduces a two-dimensional model to investigate the behavior of a footing under an inclined load. **Figure 5.2** shows a typical finite element mesh and the boundary conditions of a footing under an inclined load at the center of the footing. Regarding the type of finite element, while a four-node 1st-order element is employed for the displacement velocity, a one-node 0-order element is employed for the stress component described by the penalty method. For the number of nodes and elements, a mesh with approximately 4000 four-node iso-parametric rectangular elements was used to model the footing and the soil. A finer density mesh was employed around the footing base. The dimensions of the domains were set to be large enough so as to ensure that the boundaries would have no effect on the calculated results. The footing was assumed to be perfectly rough such that the friction angle of the interface elements between the footing and the soil would be taken as equal to the friction angle of the soil ($\phi_s = \phi_{soil}$). The footing was modeled as a solid element, the strength of which was set to be extremely high in order to simulate a rigid footing. Nguyen et al. (2016) reported that the size effect of the footing width has been observed in the ultimate bearing capacity. In this study, a series of analyses was conducted for the inclined loaded footing with the footing width in the range of B=1.0 m to 10.0 m. However, it was found that the footing width had a negligible effect on the shapes and sizes of the failure envelopes in the *V-H-M* space. The greatest difference in the shapes and sizes of the failure envelopes among the various footing widths did not exceed 3%. These results agree well with the study of Tang et al. (2015). Thus, the footing width of B=5.0 m was used for all the analyses. The footing and the soil were modeled as rigid perfectly plastic materials with the following properties: the unit weight of both the footing and the soil was $\gamma_f = \gamma_{soil} = 18$ kN/m³, the shear strength of the footing material was c_f=50000 kPa, and the internal friction angle of the footing was $\phi_f = 0°$. Small cohesion of the soil of c=0.5 kPa was introduced to stabilize the computation process, and the effect of the cohesion on the bearing capacity was systematically surveyed by changing the value of c and estimating it to be within 1% of the exact value.
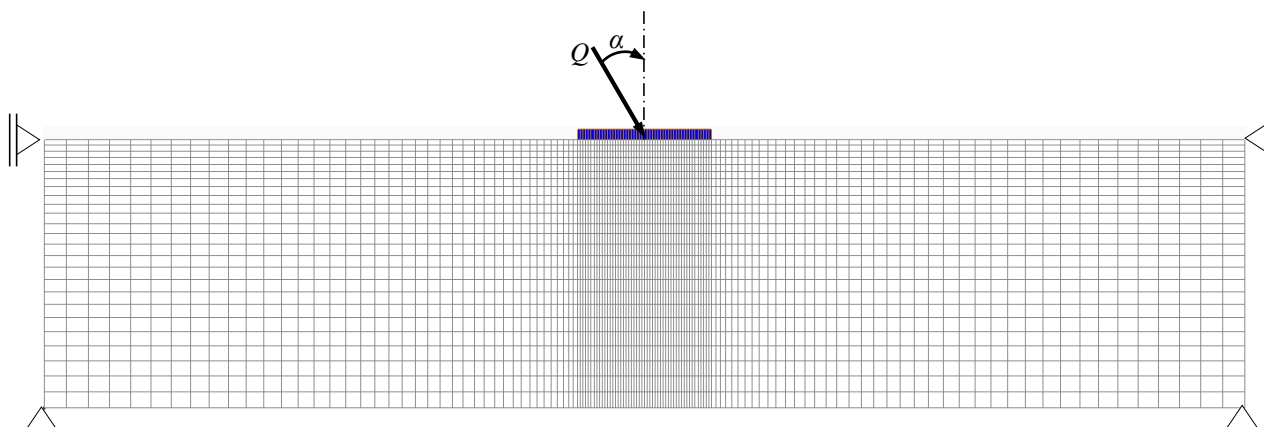
Figure 5.2. Typical finite element mesh and boundary conditions of rigid footing under inclined central load

Some expressions were adopted by different design codes for the load inclination factors providing a relatively wide range of results. The best known expressions have been suggested by Meyerhof (1963), Hansen (1970), Vesic (1975), and Loukidis et al. (2008)), as shown in **Table 5.1.** Although many studies have been conducted on this issue, no formula is totally accurate. This study examines the effect of the internal friction angle of the soil on load inclination factor i_γ and the failure envelope in the V-H plane in the case of a concentric load. The internal friction angle varies among the values of 30º, 35º, and 40º. In the computation process, horizontal capacity H_{ult} is basically unknown and it was determined under the prescribed vertical load V. The loading point is set on the bottom of the footing surface so as not to be affected by the moment component caused by the horizontal load.

Table 5.1. Summary of load inclination factor i_γ for bearing capacity of footing

Meyerhof (1963)	Hansen (1970)	Vesic (1975)	Loukidis (2008)
$i_\gamma = \left(1 - \dfrac{\alpha}{\phi}\right)^2$	$i_\gamma = \left(1 - 0.7\tan\alpha\right)^5$	$i_\gamma = \left(1 - \tan\alpha\right)^3$	$i_\gamma = \left(1 - 0.94\dfrac{\tan\alpha}{\tan\phi}\right)^{(1.5\tan\phi + 0.4)^2}$

Regarding the inclined central load on sandy soil, the inclination factor is commonly considered through a modification by the conventions of Terzaghi et al. (1943)'s bearing capacity equation. For a rigid footing placed on sandy soil with no embedment, the conventional bearing capacity equation is reduced to the following:

$$V = \frac{1}{2} i_\gamma \gamma B^2 N_\gamma \qquad (2)$$
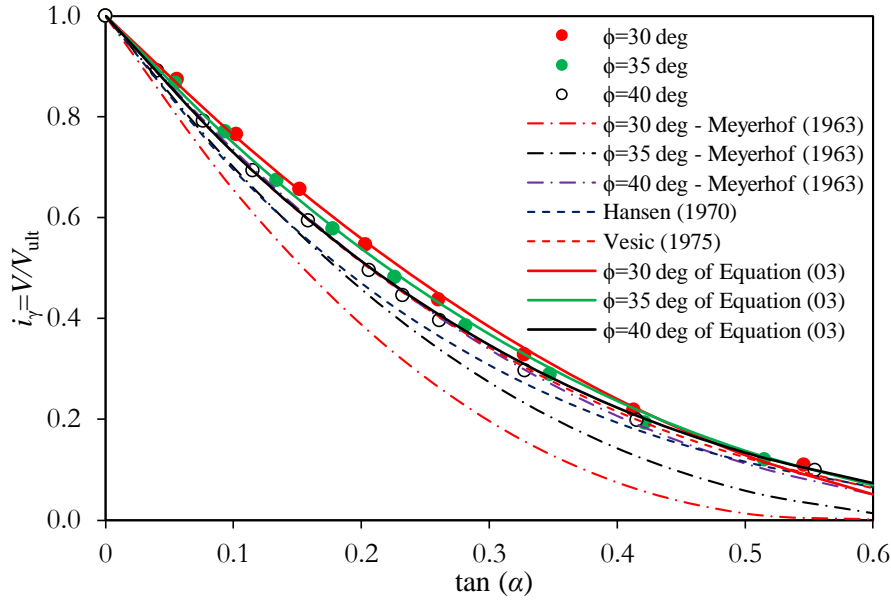
Figure 5.3. Effect of internal friction angle of soil on load inclination factor i_γ in sandy soil

Figure 5.3 shows load inclination factor i_γ for various internal friction angles of the soil in the case of an inclined central load. The figure demonstrates that load inclination factor i_γ depends greatly on the value of the internal friction angle, although Hansen (1961) and Vesic (1975) proposed inclination factors that do not depend on the value of the internal friction angle. Moreover, according to the Meyerhof (1963) solution, the curvature of the i_γ versus tan (α) line increases with an increasing ϕ, as shown in **Fig. 5.3**. While, Loukidis et al. (2008) and Zheng et al. (2019) analyzed load inclination factor i_γ subjected to the effect of the internal friction angle of soil using the finite element method. They reported that i_γ is a function of internal friction angle ϕ and inclination angle α, where i_γ decreases with an increasing ϕ. It is feasible to express the results seen in **Fig. 5.3** independent of the internal friction angle in the same way as that proposed by Hansen (1970) and Vesic (1975). Since differences are found among the obtained results, this study positively proposes inclination factor i_γ as a function of the internal friction angle, as seen in Loukidis et al. (2008) and Zheng et al. (2019).

$$i_\gamma = \left(1 - 0.76 \frac{\tan\alpha}{\tan\phi} \right)^{(1.7\tan\phi + 0.4)^2} \qquad (3)$$
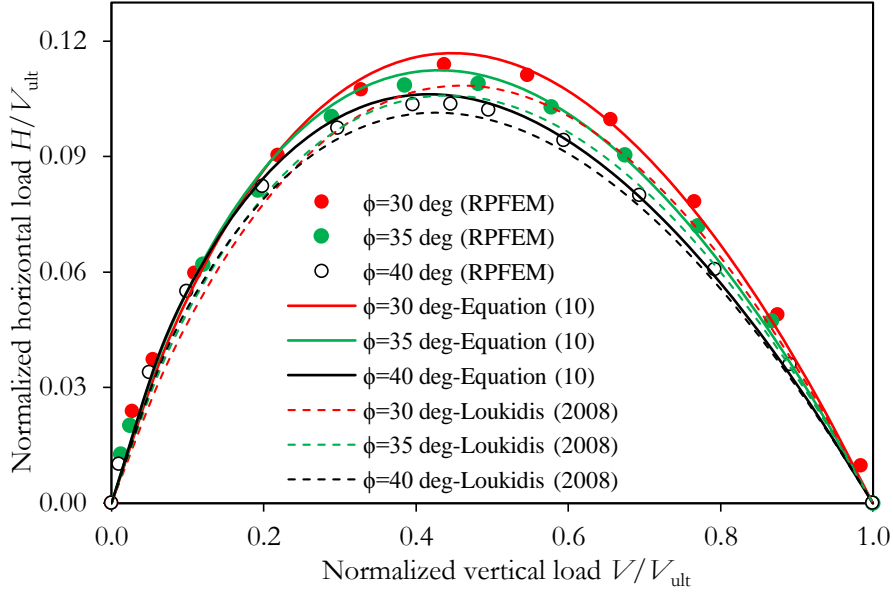
Figure 5.4. Effect of internal friction angle on failure envelopes in V-H plane in sandy soil

Figure 5.4 shows the results of the failure envelopes in the V-H plane obtained for case studies of ϕ=30°, 35°, and 40°. It shows that the sizes and shapes of the failure envelopes in the V-H plane seem to be dependent on the value of ϕ. The maximum horizontal loads, H_{max}, are approximately equal to 0.114 V_{ult} for ϕ=30°, 0.109 V_{ult} for ϕ=35°, and 0.104 V_{ult} for ϕ=40° at a value of vertical load V around 0.44 to 0.48 V_{ult}, in which, V_{ult} indicates the ultimate bearing capacity of the centric vertical load. Loukidis et al. (2008) suggested that the maximum H_{max} values fall in the range of 0.09 V_{ult} to 0.11 V_{ult} and occur at V in the range of 0.42 to 0.46 V_{ult} (α=11° to 15°). Moreover, Georgiadis et al. (1988) and Gottardi et al. (1993) conducted model tests and concluded that the values of H_{max} were in the order of 0.12 V_{ult}. From a comparison with past work, it can be concluded that the results of the RPFEM generate good estimations under the rough footing. From Eq. (3), the failure envelope in the V-H plane is derived based on the results computed with the RPFEM, as seen in **Fig. 5.4**.

$$\frac{H}{V_{ult}} = \frac{\tan\phi}{0.76}\frac{V}{V_{ult}}\left[1-\left(\frac{V}{V_{ult}}\right)^{1/(1.7\tan\phi+0.4)^2}\right] \tag{4}$$

a) e/B=0.0 and α=10º (Q=2232 kN/m)

b) e/B=0.0 and α=20º (Q=1077 kN/m)
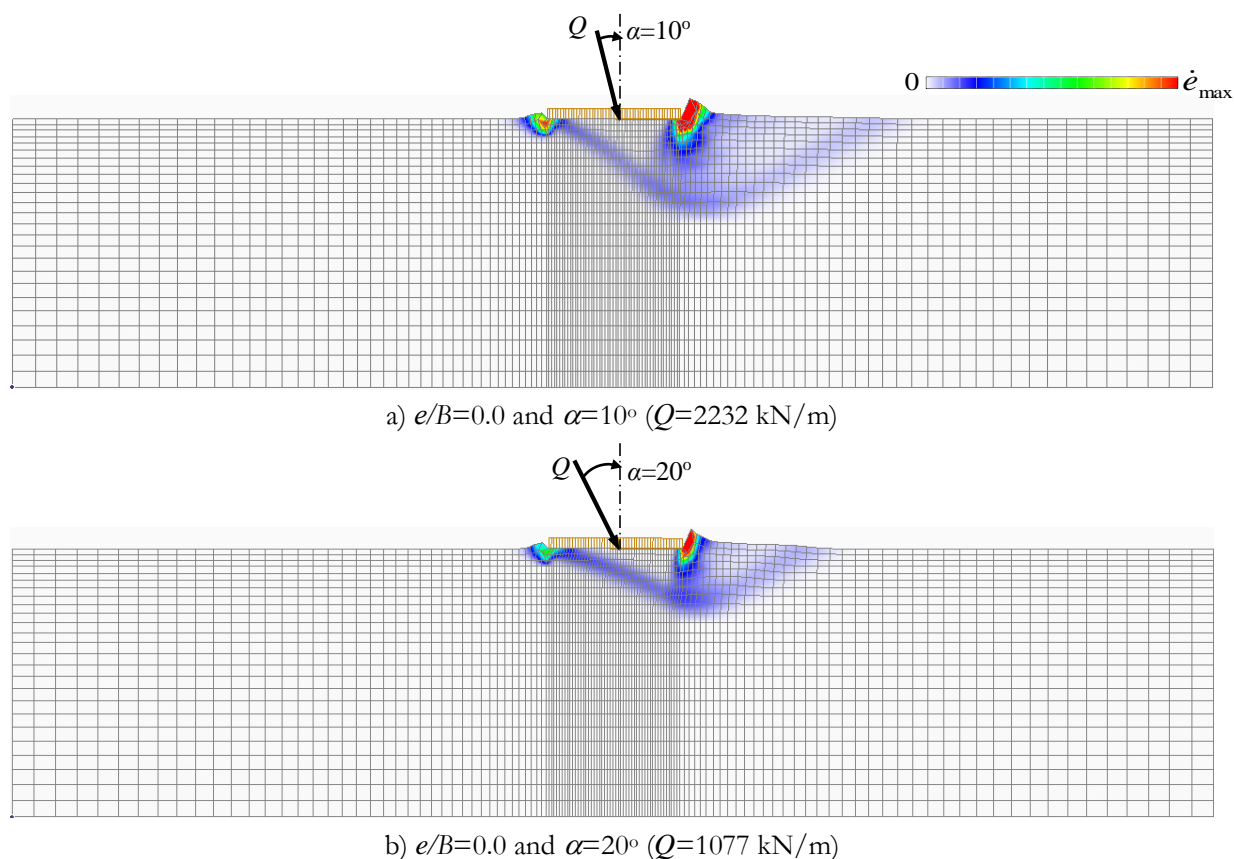
Figure 5.5. Deformation diagrams of footing-soil against inclined central load in case of sandy soil ϕ=30 deg

The obtained results for the strain rate distributions of the footing under an inclined central load on sandy soil of ϕ=30 deg at load inclination angles of α=10⁰ and 20⁰ are shown in **Fig. 5.5**. The norm of the strain rate, presented by contour lines, is in the range of $\dot{e}_{max}$ to $\dot{e}_{min}\left(=0\right)$. The distribution of $\dot{e}$ shows the failure mode of the ground and reflects the footing-soil interaction effect. **Figure 5.5(a)** indicates that the failure mode of the footing has an asymmetric shape and becomes largely one-sided as load inclination angle α increases, as seen in **Fig. 5.5(b)**. The observations of the failure mechanisms agree well with those in the results of Loukidis et al. (2008) using the finite element method. Moreover, the ultimate bearing capacity of the rigid footing was obtained at about Q=2232 kN/m for an inclination angle of α=10⁰, and was Q=1077 kN/m for an inclination angle of α=20⁰. The difference in ultimate bearing capacities due to the increase in load inclination angle α is seen to be very large. This is because the vertical and horizontal extents of the failure mechanism decrease with increasing load inclination α, which corresponds to a smaller

bearing capacity. It indicates that the RPFEM can provide reasonable predictions of the bearing capacity and the failure mode of a rigid footing on sandy soil under an inclined central load.

5.2.2 Case studies for clayey soil

The effect of inclined central loading on the undrained bearing capacity of a rigid footing is commonly taken into account through the application of load inclination factor i_c into the bearing capacity equation. For undrained conditions, the ultimate bearing capacity of a rigid surface footing can be expressed by

$$V = i_c c_u N_c B \tag{5}$$

where c_u is the undrained shear strength and i_c is the load inclination factor. There are various expressions for calculating the undrained inclination factor i_c proposed by Hansen (1961), Meyerhof (1963), and Vesic (1973), as shown in **Table 5.2**.

Table 5.2. Summary of load inclination factor i_c for bearing capacity of footing

Hansen (1961)	Meyerhof (1963)	Vesic (1973)
$i_c = 0.5 + 0.5\sqrt{1 - \dfrac{H}{Bc_u}}$	$i_c = \left(1 - \dfrac{\alpha}{90^\circ}\right)^2$	$i_c = 1 - \dfrac{2H}{Bc_u N_c}$

where H is the horizontal load, sliding failure along the footing base takes place when $H \leq Bc_u$, and α is the load inclination angle. Meyerhof (1963) reported that with values of α greater than 16.1°, the footing fails by sliding along its base. In Vesic's formula, N_c is the bearing capacity factor on clayey soil and the exact plasticity solution of N_c is 5.14.

In this section, an interface element is applied to assess the ultimate bearing capacity under an inclined load on clayey soil. The undrained shear strength of the soil and the interface element are set at c_u=100 kPa, ϕ_u=0 degrees and c_s=100 kPa, ϕ_s=0 degrees, respectively. To discuss the effect of the inclined load on load inclination factor i_c and the failure envelopes in the V-H plane, horizontal capacity H_{ult} was computed by considering the change in vertical load V varying in the range of 0.0 V_{ult} to 1.0 V_{ult}. **Figure 5.6** shows load inclination factor i_c with an increasing inclination angle tan (α). It can be seen that load inclination factor i_c significantly decreases as inclination angle α increases. The results obtained with the RPFEM are observed as being slightly higher than those of Hansen (1961) and Meyerhof (1963) at small inclination

angles for α. However, they show a good agreement with the above studies at large inclination angles for a. This is because horizontal capacity H_{ult} reached the constant value of $H_{ult}=B.c_u$. After the past work by Hansen (1961), Meyerhof (1963), and Vesic (1973), load inclination factor i_c is derived based on the results computed with the RPFEM, as seen in **Fig. 5.6**.

$$i_c = \left(1 - \frac{H}{Bc_u}\right)^{1/7.4} \tag{6}$$
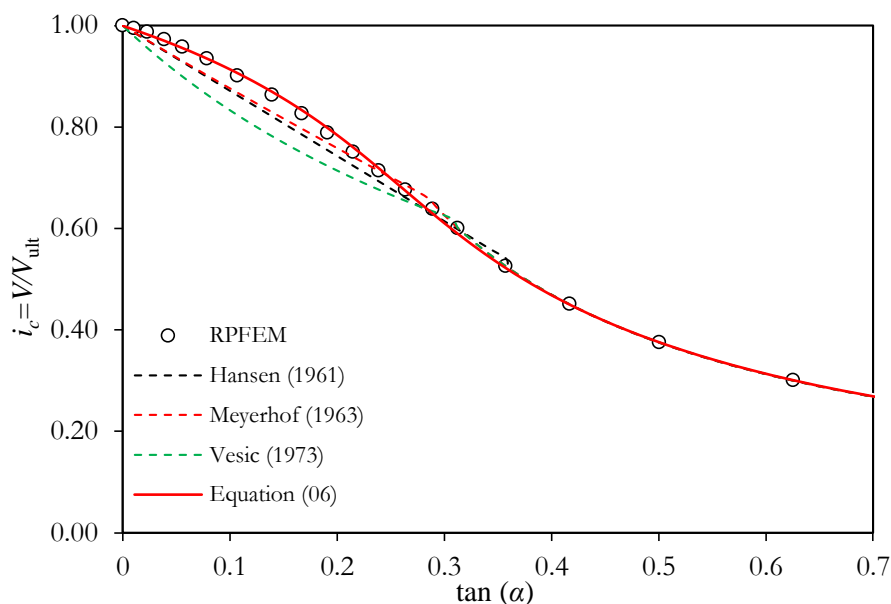
Figure 5.6. Relationship between inclination angle tan (α) and load inclination factor i_c

Figure 5.7 represents the failure envelope in the *V-H* plane obtained from the RPFEM for different load inclination angles α. It is noted that for vertical loads *V* with less than half the value of bearing capacity V_{ult}, the footing fails when the shear strength between the footing and the soil is fully mobilized, generating sliding failure at the value of constant horizontal capacity of $H_{ult}=B.c_u$. From the results of the RPFEM, it is concluded that the footing fails by sliding along its base at values of α greater than 16.4°. This is in excellent agreement with Meyerhof's solution, and smaller than the solutions of Hansen (1961) and Vesic (1973), and Kobayashi (2005) of 21.3°. From Eq. (06), the failure envelope in the *V-H* plane is derived based on the results computed with the RPFEM for clay, as seen in **Fig. 5.7**.

$$\frac{H}{V_{ult}} = \frac{1}{\pi+2}\left(1 - \left(\frac{V}{V_{ult}}\right)^{7.4}\right) \tag{07}$$
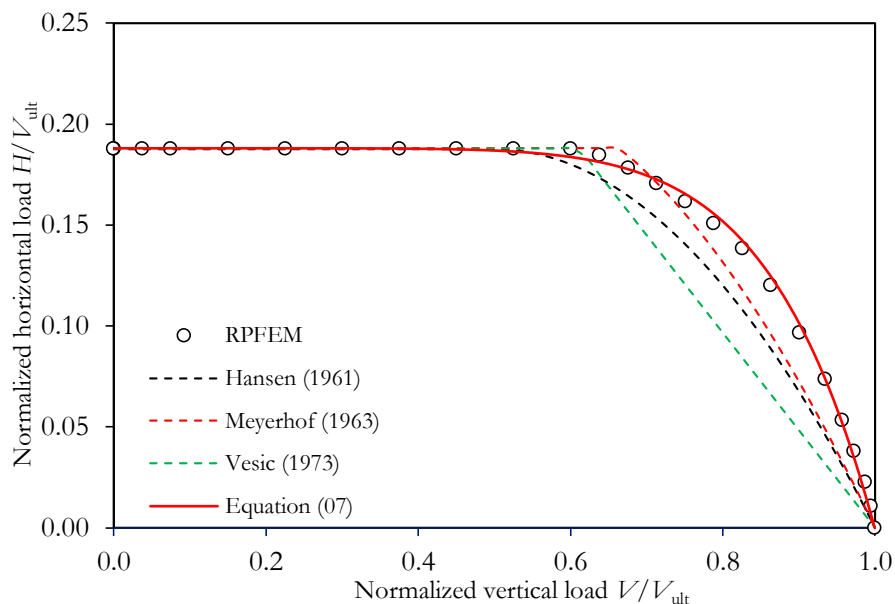
Figure 5.7. Comparison of failure envelopes in V-H plane on clayey soil

a) e/B=0.0 and α=10° (Q=4.33 Bc_u)

b) e/B=0.0 and α=20° (Q=2.93 Bc_u)
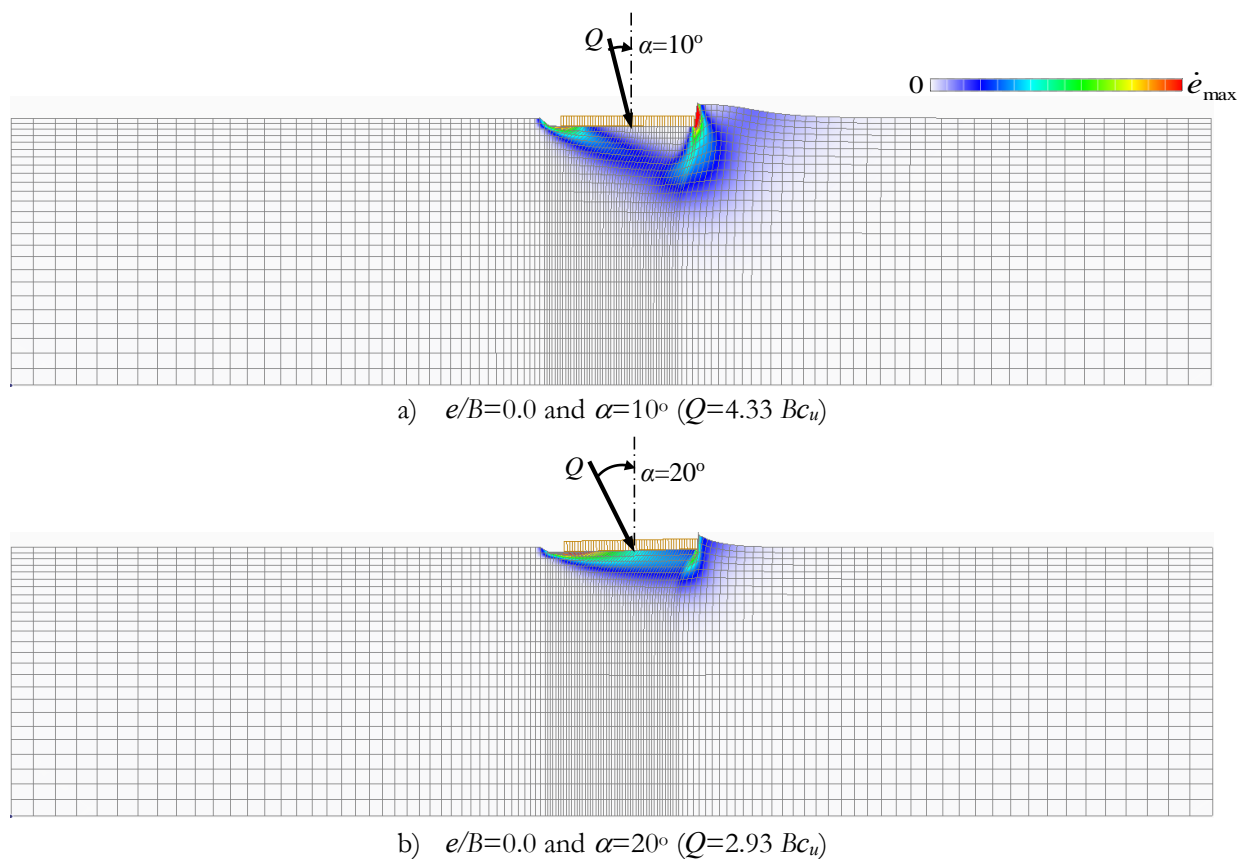
Figure 5.8. Deformation diagrams of footing-soil against inclined central load on clayey soil of c_u=100

kPa

Figure 5.8 shows the failure mode of a rigid footing obtained for various values of inclination angle

α=10° and 20°. They are completely different in shape; the failure mechanism of inclination angle α=10° is

presented as the scoop-wedge shear zone on the right-hand side of the footing, while the failure mechanism

79

of inclination angle α=20° is presented as the sliding mode and the deformation area becomes smaller and shallower than that of α=10°. Moreover, the ultimate bearing capacity of a rigid footing achieved about Q=4.33 Bc_u for the case of α=10°, and Q=2.93 Bc_u for the case of α=20°. As expected, in the same way as that for sandy soil, combinations of vertical and horizontal loadings led to a decrease in the bearing capacity with an increasing inclination angle α. From the results obtained by the RPFEM, the effect of the inclined central load on the failure envelopes in the *V-H* plane and the failure modes of the footing on clayey soil have been clarified.

5.3 ULTIMATE BEARING CAPACITY FOR ECCENTRICALLY INCLINED LOAD

5.3.1 Case study for sandy soil

In practice, rigid footings are often subjected to eccentric-inclined coupled loads. Loukidis et al. (2008) evaluated the ultimate bearing capacity of a footing against an eccentrically inclined load on sandy soil. However, they ignored the effect of the horizontal load direction on the bearing capacity of the footing and the failure envelopes in the *V-H-M* space. Only a few researches have been conducted to evaluate the bearing capacity of a rigid footing for two directions of horizontal load, namely, positive and negative loads. In this study, a series of analyses was conducted for the case of sandy soil of ϕ=30 deg taking into account the direction of the horizontal load. In particular, the study investigates three different loading paths, in which the values for the vertical load *V*, the load inclination angle tan (α), and eccentricity length *e* are controlled as constant, respectively. In each path, horizontal capacity H_{ult} is basically unknown, and it was determined under the designated condition of vertical load *V* and eccentricity length *e*, which are varied to widely survey the limit load space in the *V-H-M* space.

Figure 5.9 shows the failure envelopes in the *V-H* plane for several values of eccentricity length *e*. At the limit of a zero vertical load, the horizontal load was not sustained. It is seen that, when eccentricity length *e* increases, the size of the failure envelopes in the *V-H* plane decrease for both positive and negative horizontal loads. This is because the bearing capacity of the rigid footing decreases with an increase in eccentricity *e* regardless of the direction of the horizontal loads. It can be observed from **Fig. 5.9** that the shapes of the failure envelopes for the positive horizontal load are presented as nearly symmetric shapes, while those for the negative horizontal load are presented as asymmetric shapes. The maximum value of

normalized horizontal load H/V_{ult} for the positive horizontal load is seen to be smaller than that of the negative horizontal load corresponding to each value of e. The difference is caused by the fact that the direction of the horizontal load affected the failure envelopes in the V-H plane. **Figure 5.10** shows the failure modes obtained for e/B=0.3 and α=10° in two cases of positive and negative horizontal loads. The figure shows that the detachment between the footing and the soil occurred around the left-hand side of the footing for the positive horizontal load, while the detachment did not occur for the negative horizontal load at large eccentricity e. The failure domain is concentrated most largely on the right edge of the footing where the eccentric vertical load is placed. However, the failure mode forms more deeply and is larger along one side of the footing in the same direction as the horizontal load. The ultimate bearing capacity of the footing was computed using the RPFEM, as Q=545 kN/m for the positive horizontal load and Q=709 kN/m for the negative horizontal load. This can be easily understood with the failure mode presented in **Fig. 5.10(b)** which represents an extended failure mechanism in both horizontal and vertical directions compared with the failure mode presented in **Fig. 5.10(a)**. The numerical results of the RPFEM showed that the effects of the horizontal load direction on the failure envelopes in the V-H plane and the failure mode of the footing-soil system are considerable.
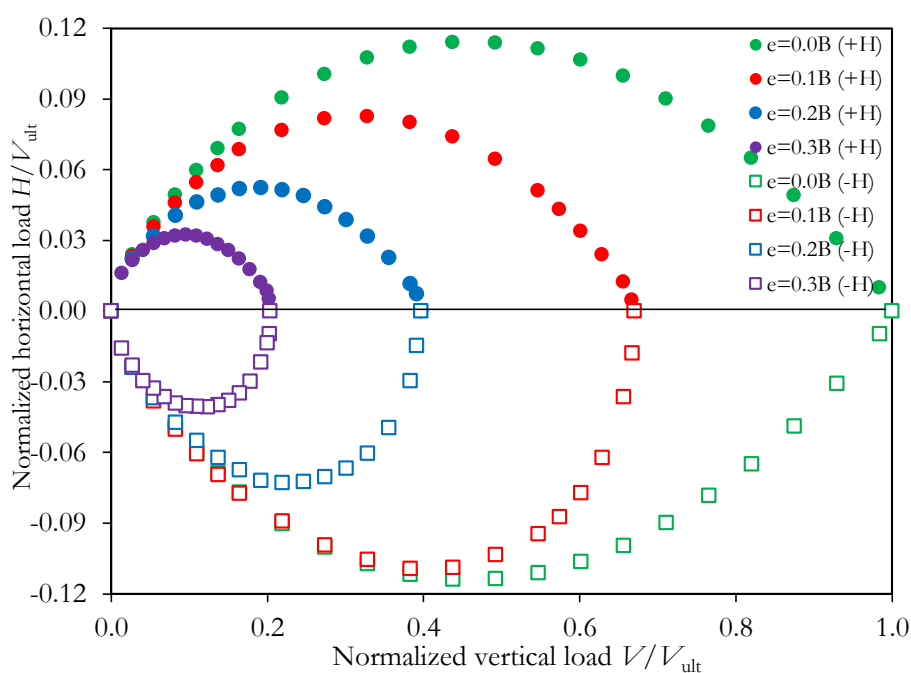
Figure 5.9. Failure envelopes in V-H plane taking into account direction of horizontal load H in case of sandy soil of ϕ = 30 deg
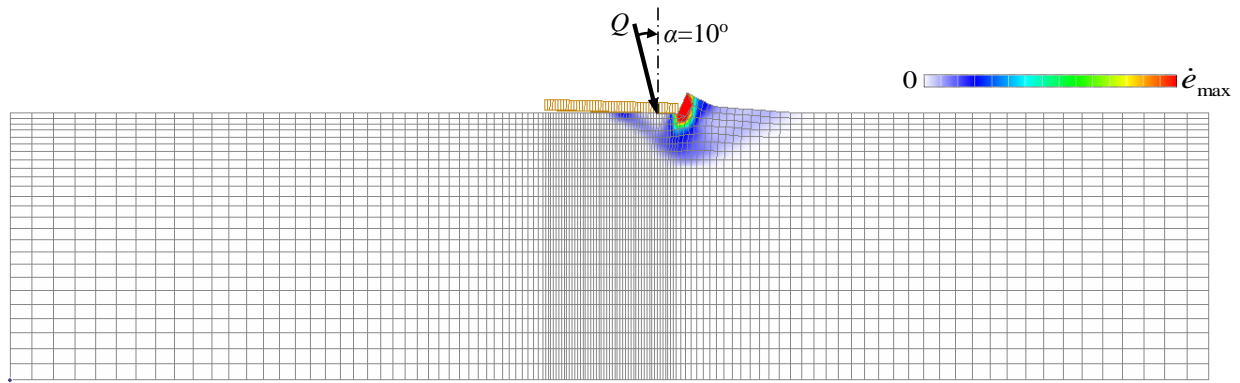
a) e/B=0.3 and α=10° (Q=545 kN/m) – Positive horizontal load (+H)
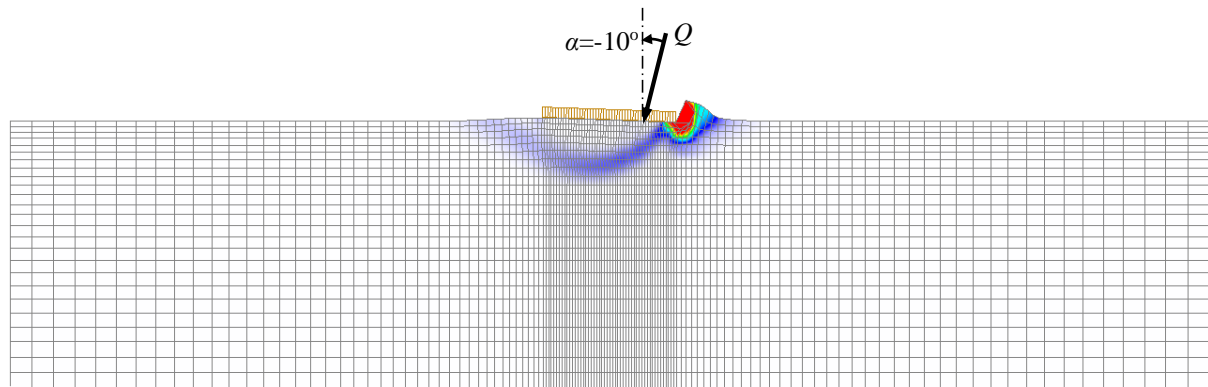
b) e/B=0.3 and α=-10° (Q=709 kN/m) - Negative horizontal load (-H)

Figure 5.10. Deformation diagrams of footing-soil against eccentric inclined load taking into account direction of horizontal load (e/B=0.3, sandy soil of ϕ=30 deg)
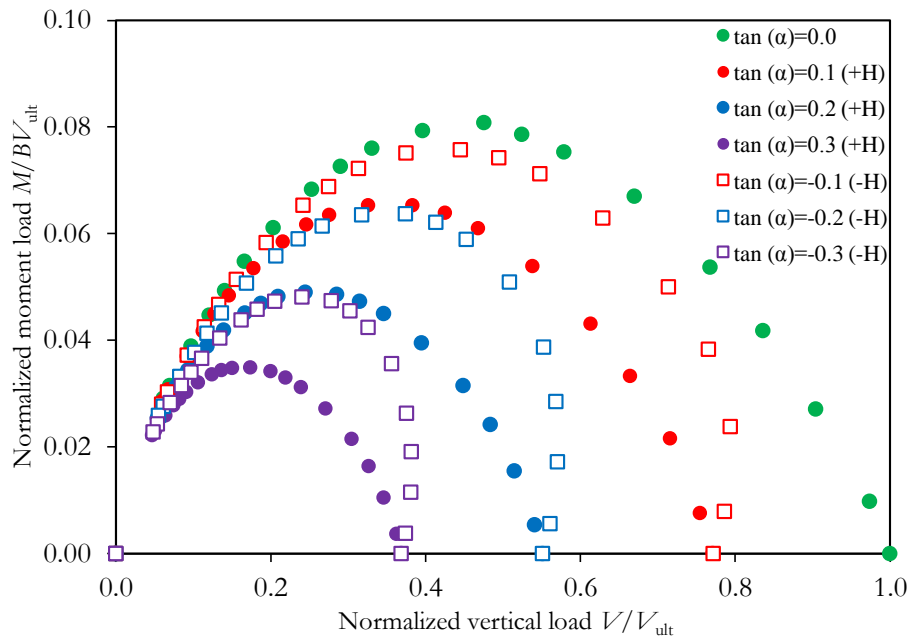
Figure 5.11. Failure envelopes in V-M plane for various values of inclination angle tan (α) taking into account direction of horizontal load in sandy soil (ϕ = 30 deg)

The failure envelopes in the V-M plane for both positive and negative horizontal loads are plotted in **Fig. 5.11**. It is interesting that the failure envelopes in the V-M plane are seen to be totally affected by the direction of the horizontal load. At the limit of a zero vertical load, the moment load was not sustained. For the positive horizontal load, the M_{max} reached approximately 0.065 BV_{ult} and 0.049 BV_{ult} for eccentricity lengths of e=0.1 B and e=0.2 B, respectively, while for the negative horizontal load, the M_{max} was approximately 0.076 BV_{ult} and 0.064 BV_{ult} at e =0.1 B and e=0.2 B, respectively, which are equally 1.17 to 1.30 times the value of the positive horizontal load. It can be seen that giving consideration to the direction of the horizontal load leads to an increase in moment capacity M_{ult} in the case of the negative horizontal load. The rigid footing can support a higher applied load at the negative horizontal load. The effects of the eccentrically inclined load and the direction of the horizontal load on the failure envelopes in the V-H and V-M planes and on the failure mode of the rigid footing have been clarified.

5.3.2 Case study for clayey soil using no tensile strength analysis

Pham et al. (2019) introduced a no tensile strength analysis into the footing-soil system to assess the ultimate bearing capacity of the eccentrically loaded footing. They reported that the application of a no tensile strength analysis was effective for analyzing the interaction between the footing and the clay. The study employed a no tensile strength analysis to calculate the undrained bearing capacity against the eccentrically inclined loading on clayey soil. The focus was placed on the ultimate bearing capacity of a footing subjected to the effect of the direction of the horizontal load. This section investigates two different loading paths, namely, normalized eccentricity e/B and inclination angle tan (α), which vary stepwise from 0.0 to 0.3. A series of analyses was conducted for the case study of clayey soil of c_u=100 kPa.

Figure 5.12 shows the failure envelopes in the V-H plane for various values of eccentricity length e. It can be seen that the shapes of the failure envelopes are similar for all values of eccentricity length e. However, the sizes of the failure envelopes decrease with increasing eccentricity length e regardless of the direction of the horizontal load. For each value of eccentricity length e, the sizes of the failure envelopes in the V-H plane for the negative horizontal load were observed to be slightly greater than those for the positive horizontal load. It was found that the direction of the horizontal load had a negligible effect on the failure envelopes in the V-H plane. The strain rate distributions of the footing in the case of e/B=0.3

and $\alpha=10^\circ$ for the positive and negative horizontal loads are shown in **Figs. 5.13(a)** and **(b)**, respectively. It is noted that the failure mechanism of the footing is typically one-sided. This is because the detachment between the footing and the soil occurred around the left-hand side of the footing regardless of the direction of the horizontal load. The failure mode for the positive horizontal load shows a slipping mode, while the failure mode for the negative horizontal load shows a single circular arc slip. Moreover, the ultimate bearing capacity of the rigid footing was obtained as a value close to 2.12 Bc_u for the positive horizontal load and 2.15Bc_u for the negative horizontal load. The difference in ultimate bearing capacities due to the direction of the horizontal load is not so large. However, it can be seen that the circular arc slip mode is more dominant with a slightly larger bearing capacity than that of the slipping mode. **Figure 5.14** shows the failure envelopes in the V-M plane for the positive and negative horizontal loads with various values for the load inclination angle tan (α). At the limit of a zero vertical load, the moment load is observed as being equal to zero. The figure indicates that the direction of the horizontal load has almost no influence on the failure envelopes in the V-M plane. Moreover, the sizes of the failure envelopes become smaller than those in the case of a decreasing load inclination angle tan (α). This is due to the decreasing vertical capacity corresponding to an increasing load inclination angle α. Finally, it can be observed from **Figs. 5.12** and **5.14** that the failure envelopes in the V-H and V-M planes are slightly affected by the direction of the horizontal load. The results for clayey soil are observed as being completely opposite those for sandy soil.
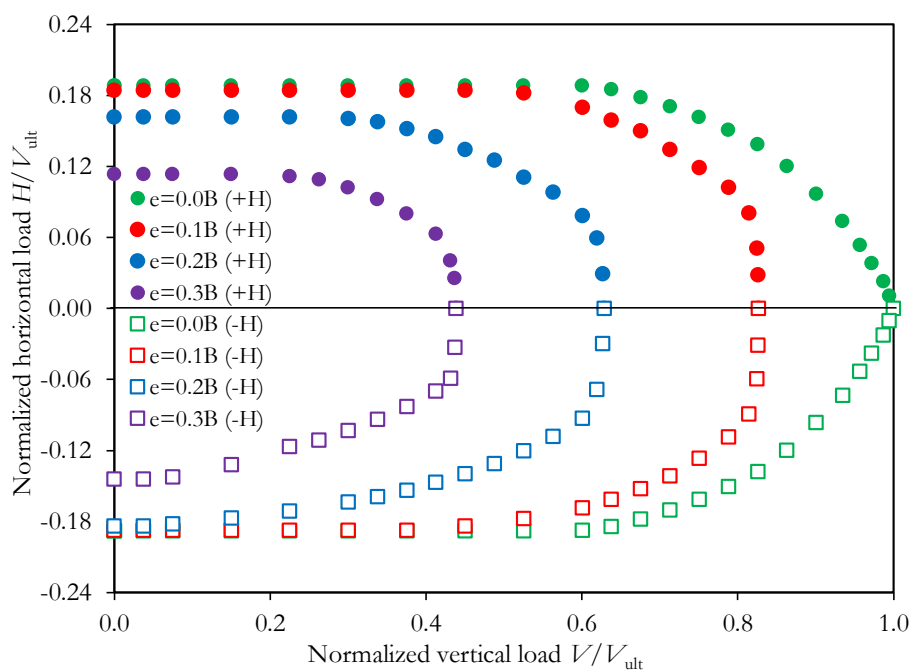
Figure 5.12. Failure envelopes in V-H plane for various values of eccentricity length e taking into account direction of horizontal load on clayey soil

a) e/B=0.3 and α=10° (Q=2.12Bc_u) – Positive horizontal load

b) e/B=0.3 and α=-10° (Q=2.15Bc_u) – Negative horizontal load
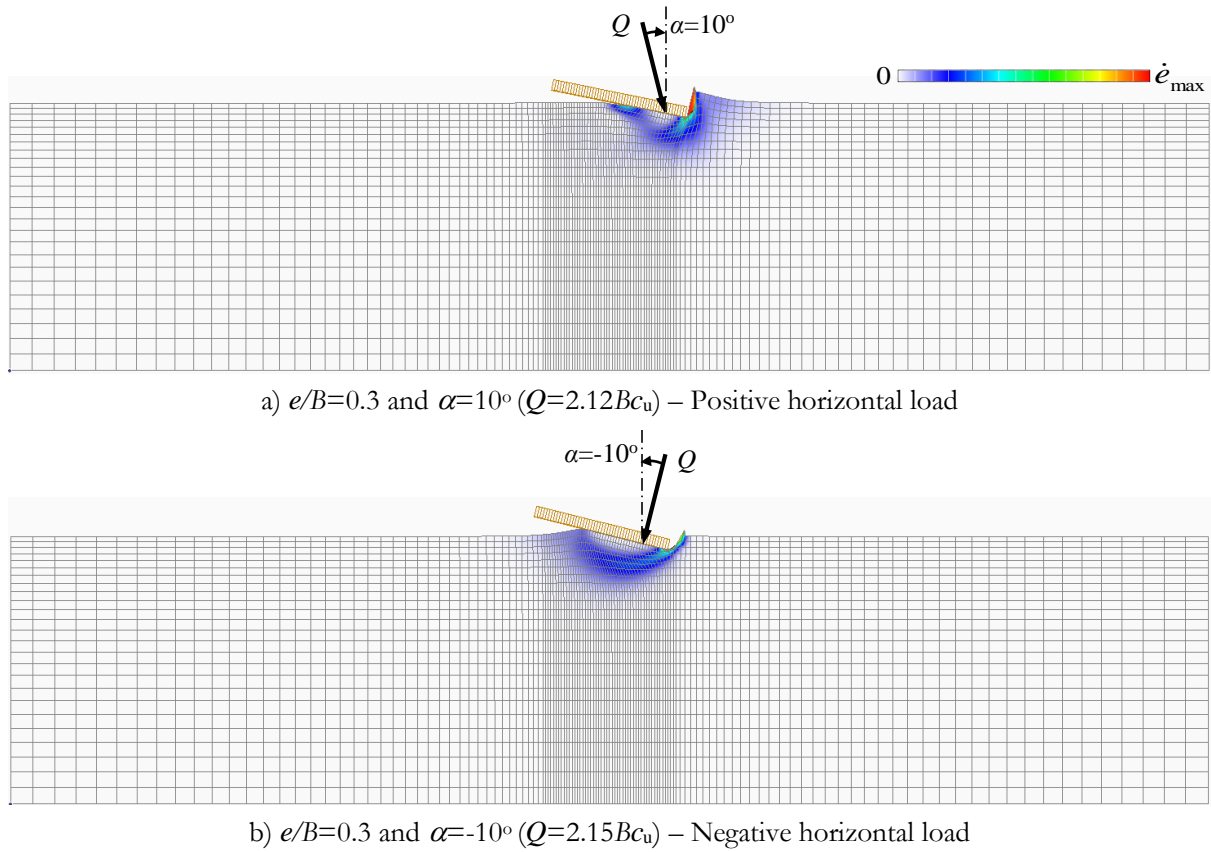
Figure 5.13. Deformation diagrams of footing-soil against eccentric inclined load taking into account direction of horizontal load (e/B=0.3, clayey soil)

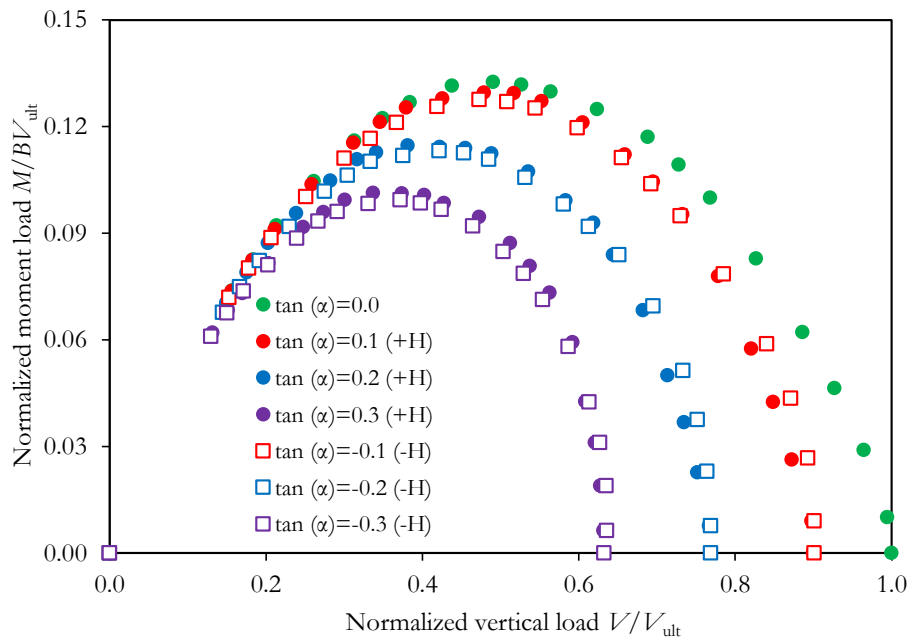
Figure 5.14. Failure envelopes in V-M plane for various values of tan (α) taking into account direction of horizontal load in clayey soil

85

5.4 FAILURE ENVELOPES FOR ULTIMATE BEARING CAPACITY IN *V-H-M* SPACE

5.4.1 Limit load space for sandy soil

The failure envelopes in the *V-H-M* space for the effect of eccentric-inclined coupled loads have relatively complex geometries. In most of the previous studies on sandy soil, such as those by Loukidis et al. (2008), Krabbenhoft et al. (2013) and Tang et al. (2014), only the effect of the eccentric-inclined coupled load on each failure envelope in the *V-H*, *V-M*, and *H-M* planes was reported; the overall failure envelopes in the *V-H-M* space were not considered. The present study investigates the failure envelopes in the *V-H-M* space for various loading paths of eccentricity length *e*, inclination angle of tan (α), and normalized vertical load V/V_{ult}. Pham et al. (2019) studied the bearing capacity of an eccentrically loaded footing on sandy soil, for which the moment load reached maximum moment M_{max} at a normalized vertical load of around V/V_{ult}=0.46 regardless of the internal friction angle. A series of analyses was conducted in the case of sandy soil of ϕ=30 deg with various values for V/V_{ult}.

Figure 5.15 shows the failure envelopes in the *H-M* plane under eccentric-inclined coupled loads at V/V_{ult}=0.25, 0.46, and 0.75. It can be seen that the sizes and shapes of the failure envelopes are dependent on the level of normalized vertical load V/V_{ult}. Moreover, these diagrams clearly show that the rigid footing can support a higher applied load with the combination of negative horizontal and positive moment loads. This is because the direction of the horizontal load affects the failure envelopes in the *H-M* plane. Similar findings were also observed by Loukidis et al. (2008), Krabbenhoft et al. (2013), and Tang et al. (2014). Most of the past works modeled the failure envelopes in the *H-M* plane by considering the equation for an ellipse by Buttterfield et al. (1994). This study proposes fitting parameter *C*=0.195 for the failure envelopes in the *H-M* plane of the RPFEM on sandy soil, as follows:

$$\left(\frac{H}{H_o}\right)^2 + \left(\frac{M}{M_o}\right)^2 + 2.C\left(\frac{H}{H_o}\right)\left(\frac{M}{M_o}\right) = 1 \tag{8}$$

where H_o is equal to the *H* values yielded by Eq. (4) and M_o is equal to the *M* values yielded by Eq. (9), which were proposed by Pham et al. (2019) and correspond to the specific value of V_o. According to the work of Loukidis et al. (2008), parameter *C* is equal to 0.267, and H_o and M_o are given by Loukidis's equations. The failure envelope by the RPFEM is in excellent accordance with that by Loukidis et al. (2008) at V_o=0.46 V_{ult}, as seen in **Fig. 5.15**.

$$\frac{M}{BV_{ult}} = 0.55 \frac{V}{V_{ult}} \left(1 - \left(\frac{V}{V_{ult}} \right)^{0.49} \right) \tag{9}$$
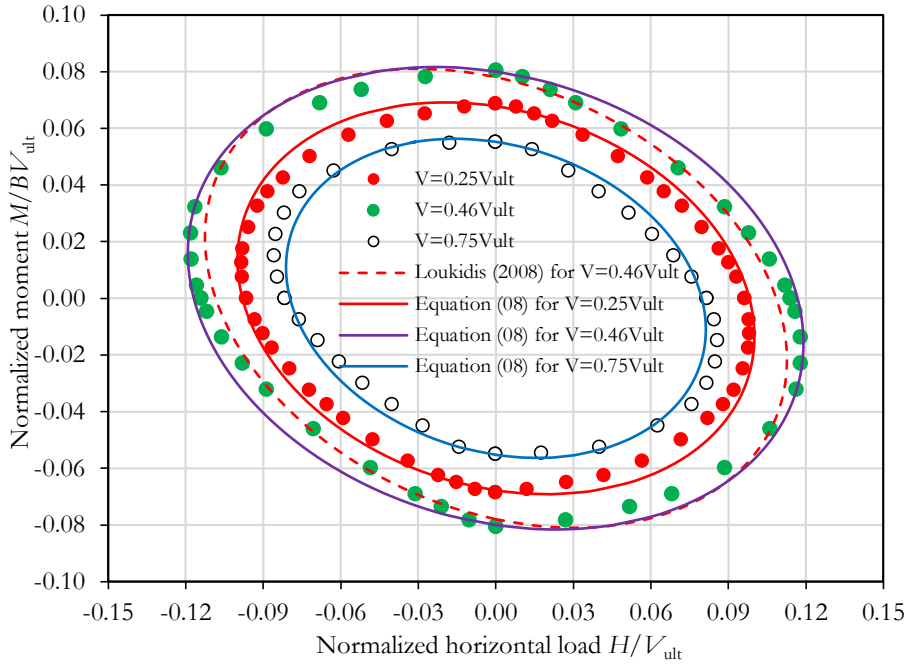
Figure 5.15. Failure envelopes in *H-M* plane for different values of normalized vertical load V/V_{ult} for case of sandy soil of ϕ = 30 deg

In addition, once the failure envelope in the *V-H-M* space of a rigid footing under an eccentrically inclined load is proposed, the question is raised as to whether it can be applied for different loading paths. Almost none of the previous studies considered the uniqueness of the limit load space. The present study widely investigates the intersecting points in the three-dimensional failure envelopes in the *V-H-M* space with three different loading paths, namely, eccentricity length *e*, the inclination angle tan (α), and normalized vertical load V/V_{ult}. A three-dimensional image of the limit load space under an eccentrically inclined load is presented in **Fig. 5.16**. The representations of the failure envelopes in the *V-H-M* space are shown as contour plots. The bold red plots denote the intersecting points calculated from the RPFEM. The figure shows some intersecting points among the contour plots of *e/B*=0.1, 0.2, and 0.3, of tan (α)=0.1, 0.2, and 0.3, and of V/V_{ult}=0.25, 0.46, and 0.75. It can be seen that the failure envelopes in the *V-H-M* space for the different loading paths are almost coincidental for the same limit surface. From the numerical results of the RPFEM, it can be concluded that the failure envelope in the *V-H-M* space is unique for each value of internal friction angle on sandy soil. The three-dimensional representation of the limit load space

provides a convenient way to explore the safety of any specific loading paths, or the consequences of any changes in the loading.
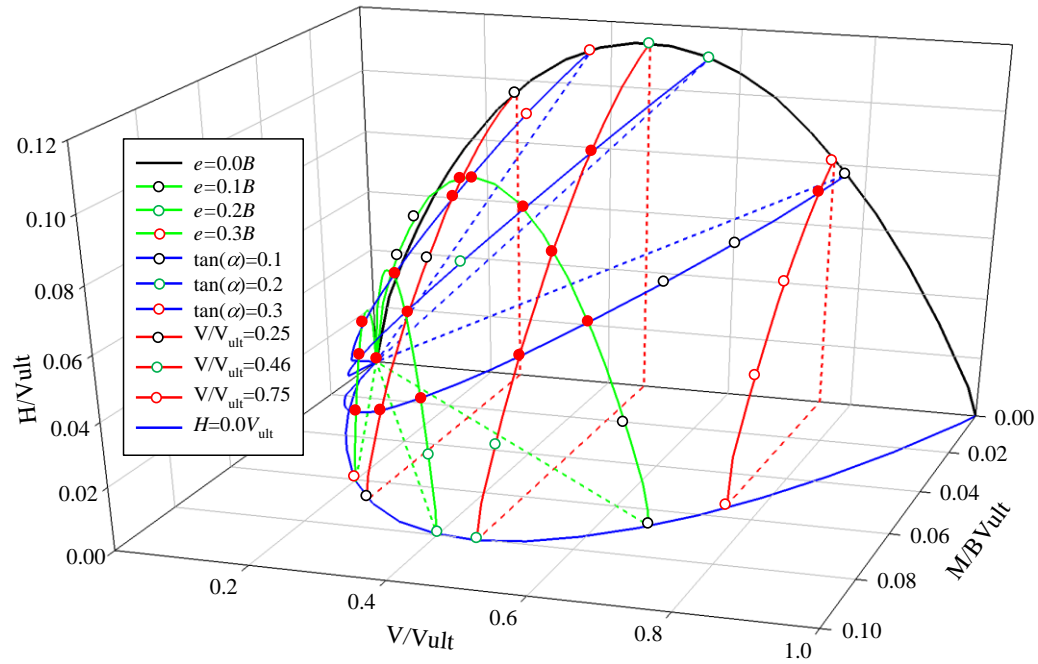
a) Case study for positive horizontal load (+H)
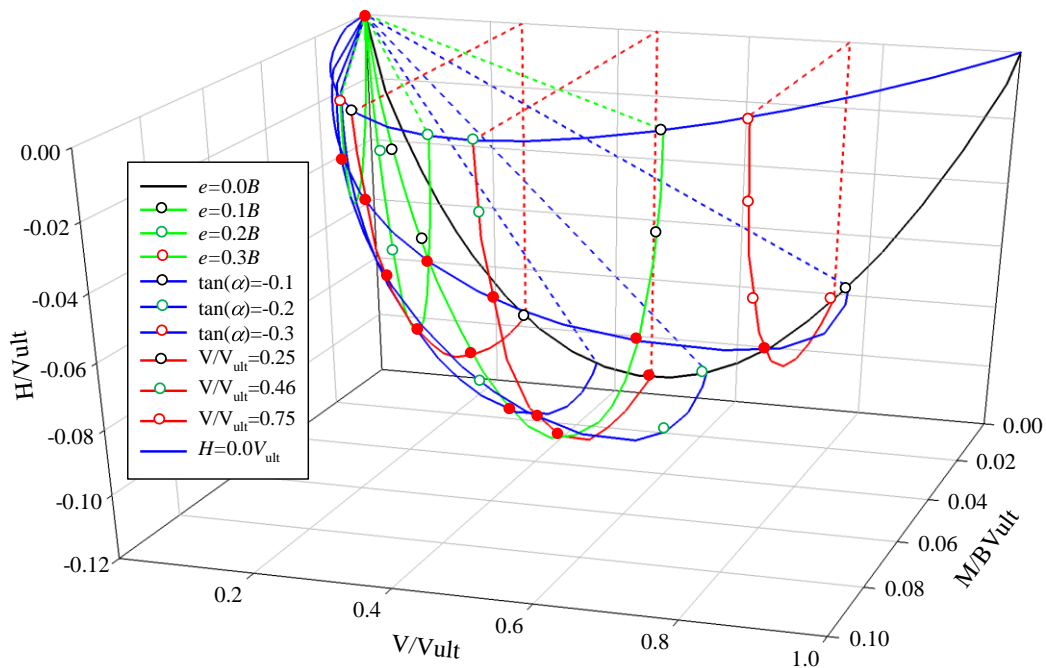
b) Case study for negative horizontal load (-H)

Figure 5.16. Limit load space of V-H-M for various values of eccentricity length e, inclination angle tan (α) and normalized vertical load V/V_{ult} for sandy soil (ϕ=30 deg)

5.4.2 Limit load space for clayey soil using no tensile strength analysis

Rao et al. (2015) and Shen et al. (2016) used the zero-tension interface to analyze the ultimate bearing capacity of a rigid footing subjected to eccentrically inclined loading. However, there are few works which have analyzed the failure envelopes in the V-H-M space for clayey soil. This study applied a no tensile strength analysis to calculate the three-dimensional failure envelopes in the V-H-M space. A series of analyses was also conducted for the case of clayey soil of c_u=100 kPa, and the obtained results were compared with those of past works.

Figure 5.17 shows the failure envelopes in the H-M plane at intervals of normalized vertical load of V/V_{ult}=0.25, 0.50, and 0.75. It can be seen that the sizes and shapes of the failure envelopes in the H-M plane also completely depend on the level of V/V_{ult}. The size of the failure envelope in the H-M plane is the maximum size at normalized vertical V/V_{ult} =0.50. Moreover, these diagrams clearly show that the direction of the horizontal load has a negligible effect on the failure envelopes. These results are completely in contrast to those for sandy soil. The obtained failure envelope in the H-M plane shows a good agreement with the failure envelope described by the FEM of Shen et al. (2016) at V/V_{ult}=0.50. The failure envelopes in the H-M plane for the rigid footing can be described by the circular ellipse expression proposed by Gourvenec (2007) to approximate the shapes of the failure envelopes in the H-M plane. Thus, this study proposes the following new equation to determine the failure envelopes in the H-M plane at various values for V/V_{ult} in clay.

$$\left(\frac{H}{H_0}\right)^2 + \left(\frac{M}{M_0}\right)^2 = 1 \tag{10}$$

where H_o and M_o are the maximum horizontal load and moment, respectively, corresponding to the specific value of V_o. H_o is equal to the H value given by Eq. (7) and M_o is equal to the M value given by Eq. (11) of Pham et al. (2019). The symmetrical elliptical failure envelope defined by Eq. 10 does not capture the asymmetry observed in the results obtained with the RPFEM. Nonetheless, it properly reflects that the effect of the direction of the horizontal load is not very large.

$$\frac{M}{BV_{ult}} = 0.63\frac{V}{V_{ult}}\left(1-\left(\frac{V}{V_{ult}}\right)^{0.80}\right) \tag{11}$$

For clayey soil, a question arises as to whether the failure envelopes in the V-H-M space are unique for

any value of undrained shear strength c_u. This study widely investigates the relationship of the three-dimensional failure envelopes in the *V-H-M* space at various values under different loading paths, which are eccentricity length e, inclination angle α, and normalized vertical load V/V_{ult}. **Figure 5.18** shows the failure envelopes in the *V-H-M* space for various values of e, tan (α), and V/V_{ult}. When the moment load is converted to the vertical stress distribution in positive and negative triangular shapes applied to the footing, the total vertical load obviously equals to zero. However, the limit load space in the *V-H-M* space of the rigid footing is made by considering the no tensile strength analysis for the footing-soil interface. The vertical stress in the tensile zone is arranged to zero stress, and the vertical load working on the footing becomes positive. The magnitude of the moment component M is correlated the vertical load, V obtained by the computation. In addition, when the eccentricity length is zero, moment M becomes zero. In this case, the failure envelope in the *V-H* is drawn for the inclination angle tan (α) of the applying load. Although it is predicted to be non-linear, horizontal load H_{ult} is obtained as constant in the range of a large inclination angle tan(α) since the shear stress at the interface between the footing and the ground attains the shear strength of the cohesive soils. Thus, the shape of the limit load space with the no tensile strength analysis is observed as being completely opposite that of sandy soil. The bold red plots denote the intersecting points calculated from the RPFEM. The figure clearly shows some intersecting points among the contour plots for eccentricity length e, the inclination angle tan (α), and normalized vertical load V/V_{ult}. From **Fig. 5.18**, it is seen that the failure envelopes in the *V-H-M* space almost coincide for all the different loading paths, and that these contour plots coexist on the same limit load surface. It can be concluded that the failure envelopes in the *V-H-M* space are unique with any value of undrained shear strength c_u.
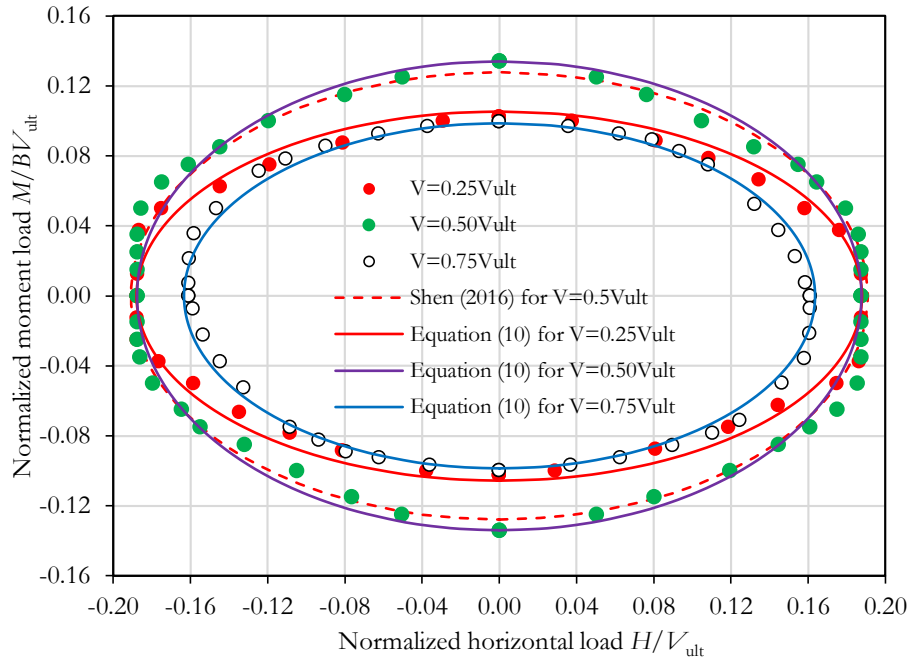
Figure 5.17. Failure envelopes in *H-M* plane for different values of normalized vertical load V/V_{ult} for clayey soil case.
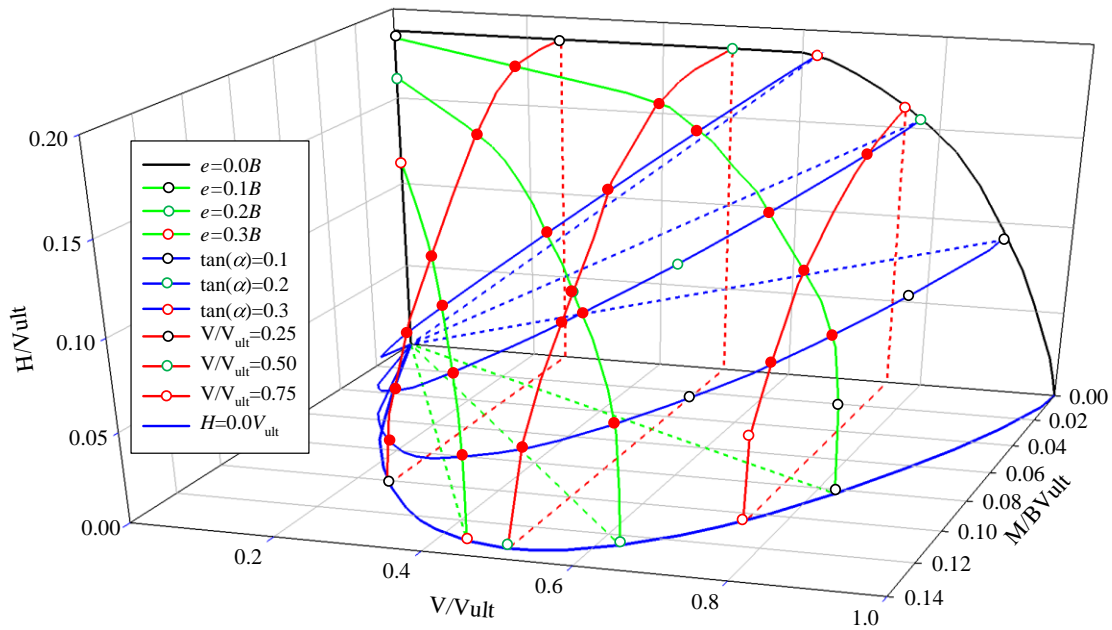
a)   Case study for positive horizontal load (+*H*)
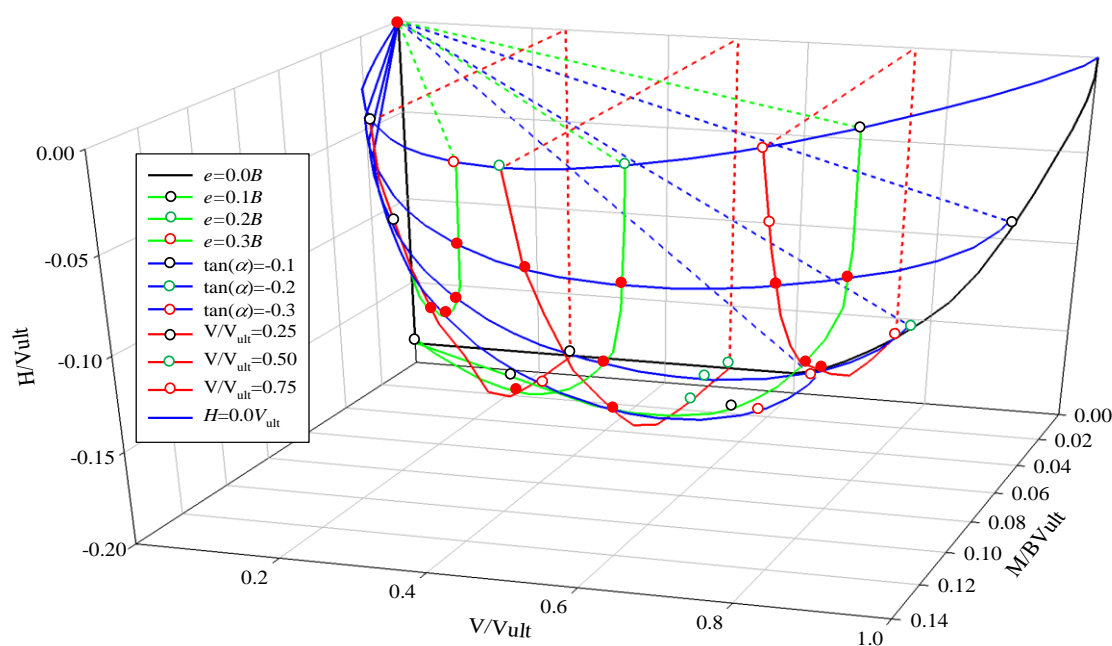
b) Case study for negative horizontal load (-H)

Figure 5.18. Limit load space of *V-H-M* for various values of eccentricity length *e,* inclination angle tan (α), and normalized vertical load V/V_{ult} for clayey soil case

5.5 DISCUSSION ON FAILURE ENVELOPES FOR ULTIMATE BEARING CAPACITY IN *V-H-M* SPACE

A question arises with the failure envelopes in the *V-H-M* space for eccentrically inclined loads as to whether or not they are applicable to combinations of the *V*, *H*, and *M* independent variables. This is because once the failure envelopes in the *V-H-M* space are proposed, it is possible to apply them to the assessment of the ultimate bearing capacity for combined loads of *V*, *H*, and *M*. However, the application of this limit load space is not clear since it was originally developed for eccentric vertical loads which are related to moment loads. Pham et al. (2019) studied the impact of combinations of centric vertical and moment loads on the failure envelopes in the *V-M* plane using the RPFEM. They reported that the sizes and shapes of the failure envelopes in the *V-M* plane in the case of combined loads were completely similar to those of eccentric vertical loads. However, most of the previous works did not consider the above question on the failure envelopes in the *V-H-M* space. This study introduces a computation process for combining the centric vertical, horizontal, and moment loads. The moment load is replaced by a triangular distributed load, the summation of which is zero in the vertical load, as shown in **Fig. 5.19**, in order to

simulate the vertical load, the horizontal load, and the moment load independently. In this computation process, moment capacity M_{ult} is basically unknown and it was determined through the prescribed horizontal load H and the specific vertical load V_o. The failure envelopes in the V-H-M space for the combined loads are symmetrically investigated for sandy and clayey soils under the rough condition of the footing surface. A series of analyses was performed for sandy soil of ϕ=30 deg at the specific value of V =0.46V_{ult} and clayey soil of c_u=100 kPa at the specific value of V=0.50V_{ult}. The properties of the interface elements employed in the analyses are similar to the soil properties of sand and clay, respectively.
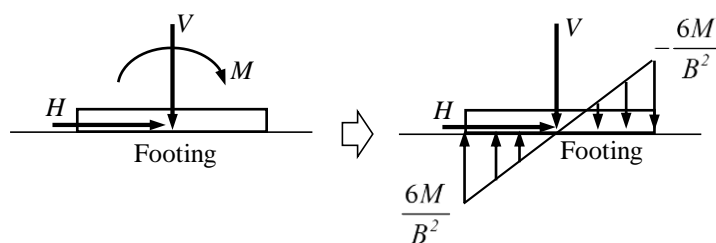
Figure 5.19. Initial load conditions for rigid plastic FEM
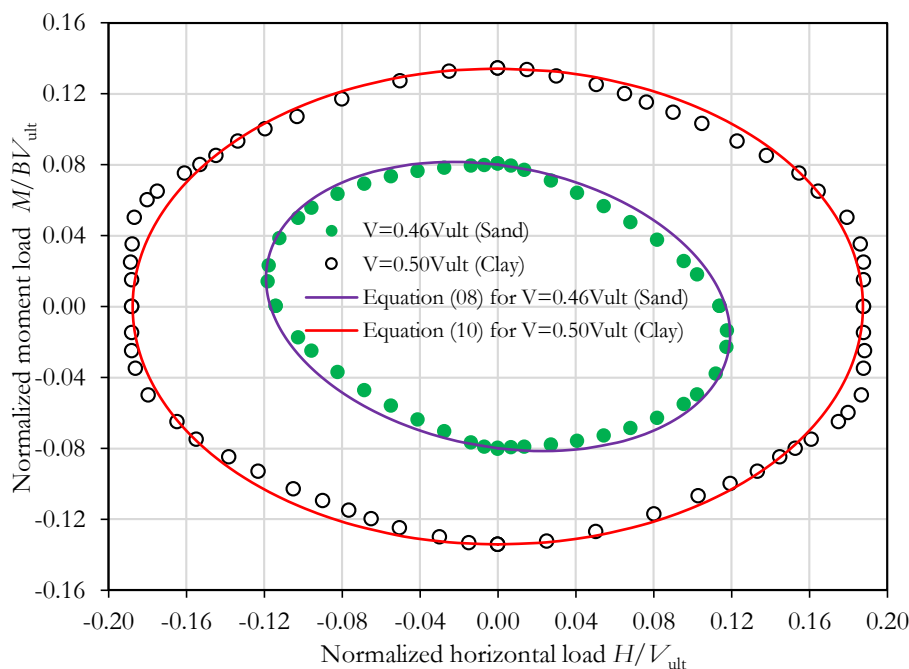
Figure 5.20. Failure envelopes in *H-M* plane against combinations of centric vertical, horizontal, and moment loads for sandy and clayey soils

Figure 5.20 shows the failure envelopes in the *H-M* plane for sandy and clayey soils subjected to combined loads. The figure demonstrates that the shape of the failure envelopes in the *H-M* plane is presented as an ellipse for both sandy and clayey soils. However, the size of the failure envelope for the

combined loads on the clayey soil is observed as being larger than that on the sandy soil. For the sandy soil of ϕ=30 deg, the failure envelope shows an asymmetric ellipse and maximum moment capacity M_{max} generally achieved a value of $0.081BV_{ult}$ at a horizontal load of H=0.0V_{ult}. For the clayey soil, the failure envelope shows a nearly symmetric ellipse and maximum moment capacity M_{max} achieved a value of nearly $0.133BV_{ult}$. It is interesting that the failure envelope in the H-M plane in the case of a combination of the centric vertical load, the horizontal load, and the moment load almost coincides with the envelopes in Eqs. 8 and 10 for the H-M plane under eccentrically inclined loads on sandy and clayey soils, respectively. It is shown in **Fig. 5.20**. These results are preferable from the simulation viewpoint because the behavior of the eccentrically inclined loads can be simulated by the combined vertical-horizontal-moment loads.

5.6 CONCLUSION.

This study has investigated the ultimate bearing capacity of a rigid footing subjected to eccentric-inclined coupled loads on sandy and clayey soils using the RPFEM. The effect of the eccentrically inclined loads on the ultimate bearing capacity and the failure mechanism of the rigid footing were analyzed by taking into account the direction of the horizontal load.

The conclusions of this study are as follows:

1. Under inclined central loading, this study examined the effect of the soil properties on load inclination factors i_γ and i_c. The numerical results of the RPFEM showed that load inclination factor i_γ needs to account for the observed dependence on the value of internal friction angle ϕ in the case of sandy soil, while load inclination factor i_c was observed to be unique in the case of clayey soil independent of the value of the cohesive strength. New equations for the RPFEM were proposed to determine load inclination factors i_γ and i_c for applications to the current design methods.

2. Under eccentrically inclined loading, the failure mechanism of a rigid footing was observed to depend on both the eccentric-inclined coupled loads and the direction of the horizontal load. For sandy soil, the failure domain was concentrated on the edge of the footing as the eccentricity length increased, but the failure zone became larger and deeper on the opposite side in the same direction as the direction of the horizontal load. On the contrary, for clayey soil, the failure mechanism was only largely one-sided due to the detachment of the footing from the soil surface on the opposite side regardless of the direction of the

horizontal load.

3. The effect of the direction of the horizontal load on the failure envelopes in the *V-H, V-M*, and *H-M* planes were clarified in a series of different loading paths. For sandy soil, the sizes and shapes of the failure envelopes in the *V-H, V-M*, and *H-M* planes were significantly affected by the direction of the horizontal load. The rigid footing was able to support a higher applied load at the negative horizontal load. However, it was almost negligible for clayey soil. New equations were proposed to determine the failure envelopes in the *V-H-M* space taking into account the direction of the horizontal load.

4. This study widely investigated the failure envelopes in the *V-H-M* space under eccentrically inclined loading on sandy and clayey soils with different loading paths. The diagrams indicated visual intersecting points between the contour plots of the *V-H, V-M*, and *H-M* planes in the three-dimensional failure envelopes in the *V-H-M* space. From the numerical results of the RPFEM, it was concluded that the failure envelope in the *V-H-M* space is unique for each value of internal friction angle in sand, and that it is also unique for any value of undrained shear strength in clay. Moreover, a negligible effect of the footing width on the failure envelopes in the *V-H-M* space was observed.

5. The study considered the impact of the combination of the centric vertical, horizontal, and moment loads on the envelopes in the *H-M* plane. The results showed that the sizes and shapes of the failure envelopes in the *H-M* plane in the case of combined loads were completely similar to those of eccentrically inclined loads. In the numerical analysis, it was possible to simulate the eccentrically inclined loads by combinations of the centric vertical load, the horizontal load, and the moment load.

References

Asaoka, A., and Ohtsuka, S., 1986. The analysis of failure of a normally consolidated clay foundation under embankment loading. Soils and Foundations. 26(2), 47-59.

Asaoka, A., and Ohtsuka, S., 1987. Bearing capacity analysis of a normally consolidated clay foundation. Soils and Foundations. 27(3), 58-70.

Asaoka, A., Ohtsuka, S., and Matsuo, M., 1990. Coupling analyses of limiting equilibrium state for normally consolidated and lightly overconsolidated soils. Soils and Foundations. 30(3), 109-123.

Butterfield, R., & Gottardi, G. 1994. A complete three-dimensional failure envelope for shallow footings on sand. Géotechnique, 44(1), 181-184.

Butterfield, R., Houlsby, G. T., & Gottardi, G. 1997. Standardized sign conventions and notation for generally loaded foundations. Géotechnique, 47(5), 1051-1054.

Cocjin, M., & Kusakabe, O. 2013. Centrifuge observations on combined loading of a strip footing on dense sand. Géotechnique, 63(5), 427-433.

Georgiadis, K. 2010. The influence of load inclination on the undrained bearing capacity of strip footings on slopes. Computers and Geotechnics, 37(3), 311-322.

Gourvenec, S. (2007). Shape effects on the capacity of rectangular footings under general loading. Géotechnique, 57(8), 637-646.

Hansen, J. B. 1961. A general formula for bearing capacity. Danish Geotechnical Institute, Bulletin No. 11, 38-46.

Hansen, J. B. 1970. A revised and extended formula for bearing capacity. Danish Geotechnical Institute, Bulletin No. 28, 5-11.

Hoshina, T., Ohtsuka, S., and Isobe, K., 2011. Rigid plastic analysis for slope including thin weak layer. Geotechnical Journal. 6, 191-200 (in Japanese).

Kobayashi, S. I. (2005). Hybrid type rigid plastic finite element analysis for bearing capacity characteristics of surface uniform loading. Soils and Foundations, 45(2), 17-27.

Krabbenhoft, S., Damkilde, L., and Krabbenhoft, K. 2013. Bearing capacity of strip footings in cohesionless soil subject to eccentric and inclined loads. International Journal of Geomechanics, 14(3), 04014003.

Loukidis, D., Chakraborty, T. and Salgado, R., 2008. Bearing capacity of strip footings on purely frictional soil under eccentric and inclined loads. Canadian Geotechnical Journal. 45(6), 768-787.

Meyerhof, G.G., 1953. The bearing capacity of foundations under eccentric and inclined loads. In Proc. of the 3rd Int. Conf. on SMFE (Vol. 1, 440-445).

Meyerhof, G. G., 1963. Some recent research on the bearing capacity of foundations. Canadian Geotechnical Journal. 1(1), 16-26.

Nguyen, D. L., Ohtsuka, S., Hoshina, T., and Isobe, K., 2016. Discussion on size effect of footing in ultimate bearing capacity of sandy soil using rigid plastic finite element method. Soils and Foundations. 56(1), 93-103.

Okamura, M., Mihara, A., Takemura, J., and Kuwano, J., 2002. Effects of footing size and aspect ratio on the bearing capacity of sand subjected to eccentric loading. Soils and Foundations. 42(4), 43-56.

Ornek, M. 2014. Estimation of ultimate loads of eccentric-inclined loaded strip footings rested on sandy soils. Neural Computing and Applications, 25(1), 39-54.

Pham, Q. N., Ohtsuka, S., Isobe, K., & Fukumoto, Y., 2019. Group effect on ultimate lateral resistance of piles against uniform ground movement. Soils and Foundations. 59(1), 27-40.

Pham, Q. N., Ohtsuka, S., Isobe, K., & Fukumoto, Y., and Hoshina, T., 2019. Ultimate bearing capacity of rigid footing under eccentric vertical load. Soils and Foundations. In press.

Rao, P., Liu, Y. and Cui, J., 2015. Bearing capacity of strip footings on two-layered clay under combined loading. Computers and Geotechnics. 69, 210-218.

Shen, Z., Feng, X., and Gourvenec, S., 2016. Undrained capacity of surface foundations with zero-tension interface under planar V-H-M loading. Computers and Geotechnics. 73, 47-57.

Tamura, T., Kobayashi, S. and Sumi, T., 1984. Limit analysis of soil structure by rigid plastic finite element method. Soils and Foundations. 24 (1), 34-42.

Tamura, T., Kobayashi, S. and Sumi, T., 1987. Rigid Plastic Finite Element Method for Frictional Materials. Soils and Foundations. 27 (3), 1-12.

Tamura, T., Kobayashi, S. and Sumi, T., 1990. Rigid Plastic Finite Element Method in Geotechnical Engineering Computational. Current Japanese Material Research. 15-23.

Tang, C., Phoon, K. K., and Toh, K. C., 2014. Effect of footing width on Nγ and failure envelope of eccentrically and obliquely loaded strip footings on sand. Canadian Geotechnical Journal. 52(6), 694-707.

Terzaghi, K., 1943. Theoretical soil mechanics. Wiley, New York.

Vesic, A. S. 1973. Analysis of ultimate loads of shallow foundations. Journal of Soil Mechanics and Foundations Division, ASCE, 99(1), 45-73.

Vesic, A.S. 1975. Bearing capacity of shallow foundations. In Foundation engineering handbook. Edited by H.F. Winterkorn and H.-Y. Fang. Van Nostrand Reinhold, New York, 121-147.

Patra, C., Behara, R., Sivakugan, N., & Das, B. 2012. Ultimate bearing capacity of shallow strip foundation under eccentrically inclined load, Part I. International Journal of Geotechnical Engineering, 6(3), 343-352.

Patra, C., Behara, R., Sivakugan, N., & Das, B. 2012. Ultimate bearing capacity of shallow strip foundation under eccentrically inclined load, Part II. International Journal of Geotechnical Engineering, 6(4), 507-514.

Yahia-Cherif, H., Mabrouki, A., Benmeddour, D., and Mellas, M., 2017. Bearing capacity of embedded strip footings on cohesionless soil under vertical and horizontal loads. Geotechnical and Geological Engineering. 35(2), 547-558.

Zheng, G., Zhao, J., Zhou, H., & Zhang, T. 2019. Ultimate bearing capacity of strip footings on sand overlying clay under inclined loading. Computers and Geotechnics, 106, 266-273.

Chapter 6

FURTHER RESEARCH:
ULTIMATE BEARING CAPACITY OF RIGID FOOTING RESTING ON SAND LAYER OVER CLAY

6.1. INTRODUCTION

In engineering practice, the bearing capacity of a rigid footing on a sand layer over clay soil is commonly calculated through the use of bearing capacity models. The best known expressions have been suggested by the projected area model of Terzaghi et al. (1948) and the punching shear model of Meyerhof (1974) and Okamura et al. (1998). The model of Terzaghi et al. (1948) was based on the assumption that the pressure is distributed uniformly on the sand layer surface, having an equivalent footing with an effective footing width B' resting on the clay layer, but the shear resistance of the sand layer was ignored. On the contrary, the models of Meyerhof (1974) and Hanna and Meyerhof (1980) assumed that punching shear failure occurred in the sand layer as a rigid sand block and general shear failure occurred in the clay layer. The shear resistance was considered via the punching shear coefficient (K_s), which was determined by a design chart. However, this method ignored the effect of the shear strength of two-layered soils on the shape of the rigid sand block. Okamura et al. (1998) also assumed the formation of a rigid sand block during punching shear failure to calculate the bearing capacity of the footing on two layers consisting of sand and clay. They proposed a new equation to calculate the shear angle of the rigid sand block based on the soil properties of the two layers. Recently, Eshkevari et al. (2019) introduced a new bearing capacity model based on the limit equilibrium condition of a rigid sand block during punching shear failure in the sand layer to directly estimate the ultimate bearing capacity. They reported that the shear angle of the rigid sand block may be positive or negative depending on the relative strength of the two-layered soil. However, the applicability of these bearing capacity models has not been clarified due to the lack of a systematic analysis based on a reliable stability method. Therefore, the validity of the current design methods needs to be verified by applying bearing capacity models. In recent years, the ultimate bearing capacity of rigid footings on sand overlying clay has been investigated by several researchers using numerical analyses and model

tests. Shiau et al. (2003), Yamamoto et al. (2005), Rajaei et al. (2017), Zheng et al. (2019), and Eshkevari et al. (2019) used numerical analyses to calculate the bearing capacity under vertical loading on a sand layer over clay soil. From the numerical results, it was concluded that the ultimate bearing capacity was significantly affected by the soil properties of the two-layered soil and the geometric conditions of the sand layer. The same results were also obtained from model tests conducted by Okamura et al. (1997), Teh et al. (2010), and Hossain et al. (2014). Although many works have been performed to investigate the bearing capacity of vertically loaded footings on sand overlying clay, a comprehensive understanding of the failure mechanism of the footing-soil system and the bearing capacity model has not yet been established.

In footing-soil systems, the ultimate bearing capacity of the footing depends exclusively on the friction condition between the footing and the soil. The footing surface has been modeled under two extreme conditions, namely, either perfectly smooth or perfectly rough. Most of the previous studies, such as Yamamoto et al. (2005), Rajaei et al. (2017), Zheng et al. (2019), and Eshkevari et al. (2019), only considered the rough condition of the footing surface and did not consider the smooth condition. Pham et al. (2019b) studied the ultimate bearing capacity subjected to central and eccentric vertical loading on uniform layers of sand and clay using an interface element. They found that the application of an interface element was effective for determining the ultimate bearing capacity and the failure mechanism of a rigid footing. In the present study, the interface element is employed to widely investigate the distribution of contact stress along the footing base and the failure mechanism reflecting the two different friction conditions. The footing-soil system with a two-dimensional analysis is simulated with the rigid plastic finite element method (RPFEM). The RPFEM has been applied in geotechnical engineering by Tamura et al. (1984, 1990), Asaoka and Ohtsuka (1986, 1987), and Asaoka et al. (1990), and was further developed by Tamura et al. (1987) for friction material. The method was originally developed based on the upper bound theorem in the limit analysis, but was shown to have been derived directly from the rigid plastic constitutive equation by Tamura et al. (1984). The study introduced a new constitutive equation for solid elements to simulate the footing and the soil, and for interface elements to simulate the interface plane between the footing and the soil. The applicability of the rigid plastic constitutive equation to the assessment of the ultimate bearing capacity of a vertically loaded footing on sand overlying clay is examined from the viewpoints of the interaction between the footing and the soil and the failure mechanism of the footing-soil system.

In addition, the failure mechanisms of two-layered soils are complex because the failure mode may break through the upper sand layer into the lower clay layer or the failure may only be within the sand layer. The focus here is placed on an investigation of the bearing capacity and the failure mechanism of a rigid footing located on sand overlying clay by increasing thickness D and the internal friction angle ϕ of the sand layer for two extreme friction conditions, for which two cases are considered for the shear strength of the clay layer, namely, a weak layer and a stiff layer. Moreover, the study introduces a new equation based on the limit equilibrium condition of a rigid sand block during punching shear failure to determine the ultimate bearing capacity. The proposed equation provides results in close agreement with those given in the literature, while remaining simple and efficient enough to be used in practice.

## 6.2. APPLICABILITY TO VERTICAL LOAD ON UNIFORM SANDY SOIL UNDER TWO CONTACT CONDITONS.

Figure 6.1(a) shows a typical finite element mesh and boundary condition of a footing-soil system on uniform sandy soil using an interface element at the footing base. A uniform distributed load q was employed at all node surfaces of the footing element to define the prescribed load and the load coefficient, for which the ultimate bearing capacity was assessed by computing the limit value for this load coefficient. Analyses were performed for a footing width of B=5.0 m. The footing and the soil were modeled as a solid element and rigid perfectly plastic materials with the following properties: the unit weight of both the footing and the soil was $\gamma_f=\gamma_{soil}$=18 kN/m³, the shear strength of the footing material was c_f=50000 kPa, and the internal friction angle of the footing material was ϕ_f=0°. In computation process, small cohesion of the soil, c=0.5 kPa, was applied to stabilize the computation process, but the effect of cohesion on the ultimate bearing capacity was found to be small. Two friction conditions were considered for the footing surface by using the interface element properties in the case of ϕ_{soil}=30 deg, as shown in **Table 6.1**.

Table 6.1. Interface element properties of the footing-sand layer.

Parameter	Rough condition	Smooth condition
Internal friction angle ϕ_s (º)	$\phi_s=\phi_{soil}$=30	0
Shear strength c_s (kPa)	0.5	0.5

The ultimate bearing capacity q of the footing was generally achieved as a value close to 8.47 γB for

the rough condition and a value close to 4.42 γB for the smooth condition. These values are generally 52% of those for the rough condition, in which the bearing capacity is normalized by the soil unit weight and the footing width. As a result, since the setting of the soil unit weight and the footing width does not affect the ultimate bearing capacity, the ultimate bearing capacity is shown irrespective of them. A comparison with past work for the rough condition revealed that the limiting value was close to q=8.87 γB given by Shiau et al. (2003) using FEM, and q=7.83 γB predicted by Meyerhof (1951) using a model test. Moreover, the results obtained for the strain rate distribution of the footing-soil system for the two friction conditions are shown in Fig. 2. The norm of the strain rate, presented by contour lines, is in the range of $\dot{e}_{max}$ to $\dot{e}_{min}(=0)$. The distribution of $\dot{e}$ shows the failure mode of the ground and reflects the footing-soil contact condition. The failure depth of the ground from the footing base is observed to be nearly equal to 1.0 B for the rough footing (**Fig. 6.1(a)**) and 0.5 B for the smooth footing (**Fig. 6.1(b)**). This is because, when the ultimate load is applied to a footing, the failure area will develop up to a certain depth depending on the value of ϕ and the friction conditions of the footing surface. Furthermore, the rigid block forming below the footing was apparently different between the two friction conditions. The failure mechanism of the rough condition is characterized by a triangular wedge under the footing moving downward as a rigid block with the same velocity as the footing. While the failure mechanism of the smooth condition is characterized by two rigid triangular wedges, the two rigid wedges tend to move towards the two edges of the footing. The obtained failure mode shows a good agreement with the slip line of the rough footing reported by the FEM of Nguyen et al. (2016) and Pham et al. (2019b). The results obtained of RPFEM for the ultimate bearing capacity and the failure mechanism were found to closely match those in past works.


a) Typical finite element mesh and boundary condition of model (Rough condition, q=8.47 γB)
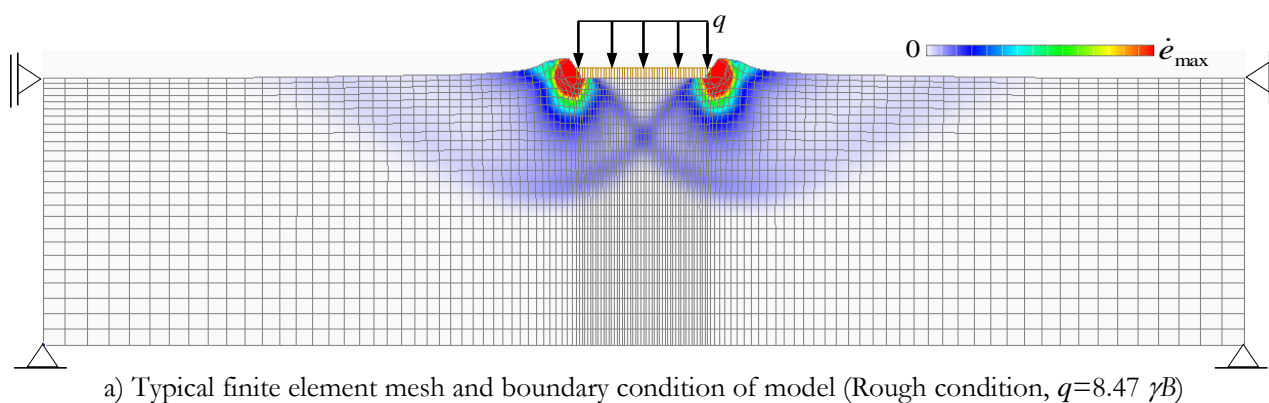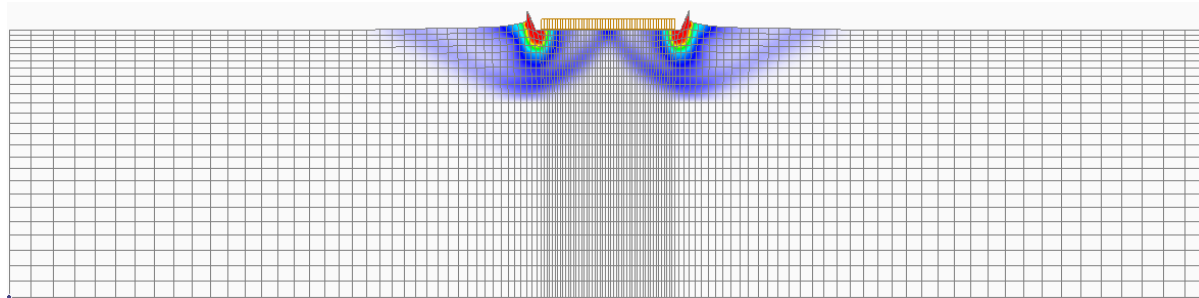
b)   Deformation diagrams of footing-soil (Smooth condition, $q=4.42\ \gamma B$)

Figure 6.1. Typical finite element meshes, boundary conditions, and deformation diagrams of footing-soil on single layer of sandy soil of $\phi=30$ deg

6.3 ULTIMATE BEARING CAPACITY OF RIGID FOOTING ON SAND OVERLYING CLAY

6.3.1 Interaction of footing and soil under two contact conditions.

In practice, the base of a rigid footing often rests on the soil-layer system of more than one layer. This study examined the ultimate bearing capacity of a rigid footing on a two-layered horizontal soil substrate, for which the rigid footing was situated on a sand layer with an internal friction angle ϕ overlaying infinite deep clay with undrained shear strength c_u. D is the thickness of the sand layer and γ is the unit weight of the sand layer, as shown in **Fig. 6.2**. Yamamoto et al. (2005) evaluated the ultimate bearing capacity of a vertically loaded footing on sand-over-clay for the rough condition. In their results, a difference was found in the distribution of normal stress $\sigma_n/\gamma B$ acting on the footing base corresponding to changes in sand layer thickness D. However, only a few researches have been performed to evaluate the distribution of contact normal stress under two extreme friction conditions. The present study investigated the distribution of contact normal stress $\sigma_n/\gamma B$ under two friction conditions in a typical case of a sand layer of $\phi=30$ deg overlying a weak clay layer of $c_u=0.5\ \gamma B$. The values for the sand layer thickness were varied in the range of 0.25 B to 2.0 B.
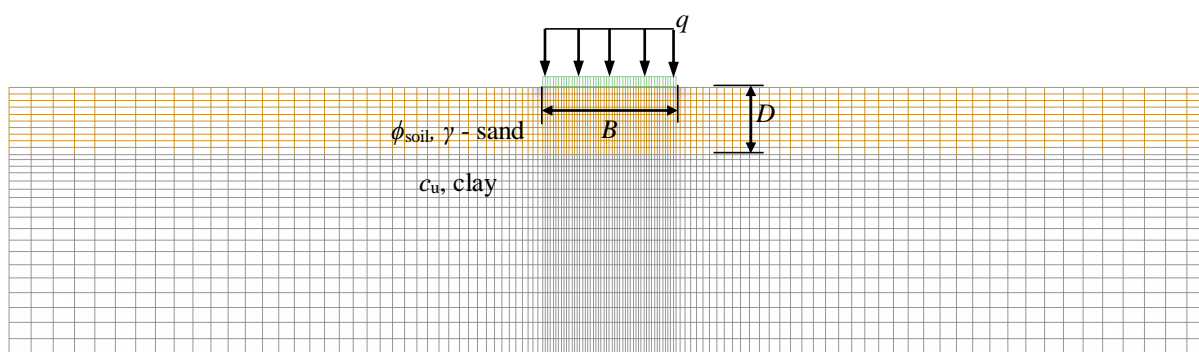
Figure 6.2. Schematic of the RPFEM model of rigid footing on sand-over-clay
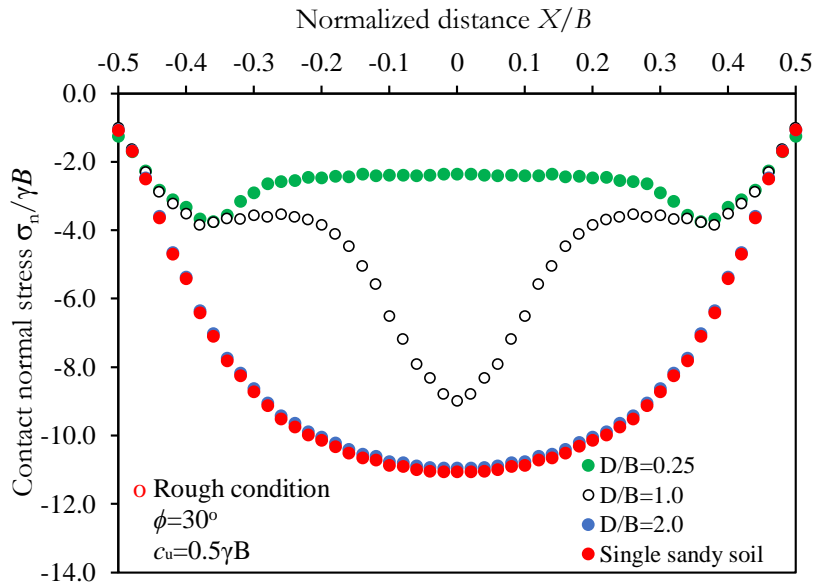
a) Rough condition
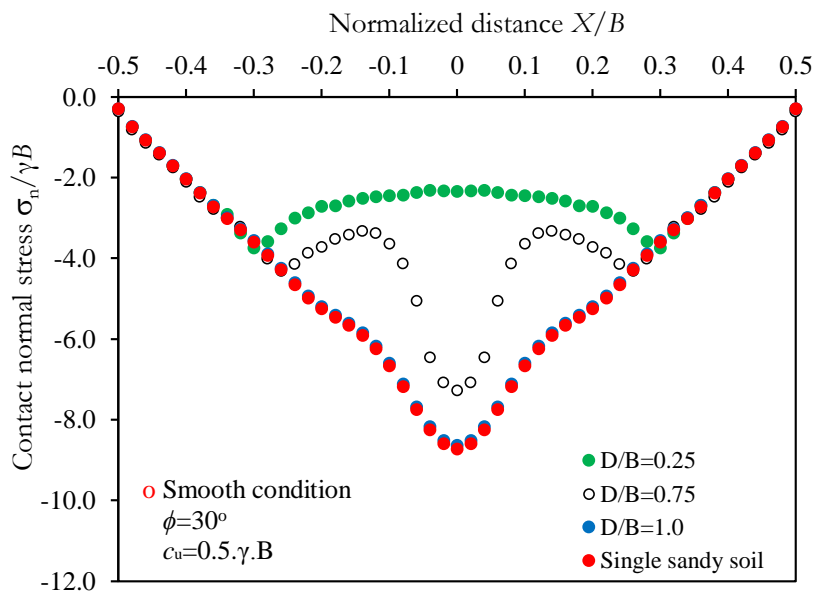
b) Smooth condition

Figure 6.3. Distributions of contact normal stress $\sigma_n/\gamma B$ acting at footing base on sand of $\phi=30$ deg overlying clay $c_u=0.5\ \gamma B$ for rough and smooth conditions

Figure 6.3 shows the distributions of contact normal stress $\sigma_n/\gamma B$ at the footing base corresponding to normalized distance X/B, in which, X is the location in the footing from the center of the footing. The normal stress $\sigma_n/\gamma B$ is assessed by computing the interaction force at the nodes of the interface elements. It is seen that, when sand layer thickness D is increased, the size of the normal stress distribution ($\sigma_n/\gamma B$)

increases for both rough and smooth conditions, and that the contact normal stress is observed as being smaller than that of a single layer of sandy soil. The size of $\sigma_n/\gamma B$ for the rough condition is larger than that for the smooth condition. For a single layer of sandy soil, the normal stress distribution is seen to have a convex shape, with a curved shape for the rough condition and a triangular shape for the smooth condition. On the contrary, Pham et al. (2019b) reported that, for a single layer of clayey soil, the normal stress distribution is seen to have a concave shape with respect to the center of the footing for both rough and smooth conditions. From the results obtained by the RPFEM for sand overlying clay at the small thickness of $D=0.25$ B, the shape of the distribution ($\sigma_n/\gamma B$) is presented as the combined distribution of the sand and clay layers which are characterized by a concave shape in the center of the footing and by a convex shape on the two edges of the footing. However, when the sand layer thickness is then increased to $D=1.0$ B for the rough condition and $D=0.75$ B for the smooth condition, the shape of the distribution ($\sigma_n/\gamma B$) is presented as a large-convex shape at the center of the footing. This proves that the influence of the clay layer on the distribution of contact normal stress is lowered, while the influence of the sand layer is raised by an increase in thickness. When the sand layer thickness reaches $D=2.0$ B for the rough condition and $D=1.0$ B for the smooth condition, the distribution of contact normal stress is observed to coincide with that of a single layer of sandy soil. As expected, increasing the sand layer thickness led to the behavior of the two-layered soil becoming similar to that of a single layer of sandy soil.

Figure 6.4 shows the failure modes of a rigid footing obtained for two values of thickness, namely, $D=0.25$ B and 1.0 B, in typical cases of the rough condition. It is seen that the failure mechanism of the footing-soil system reflects the collapse mode of two-layered systems. The failure mode is seen to have broken through the sand layer into the clay layer, where the punching failure mode is formed in the sand layer as a rigid sand block. The failure zone of a rigid footing becomes wider and deeper in the sand layer, while the general failure zone in the clay layer is greatly reduced as the sand layer thickness increases. Moreover, the ultimate bearing capacity was computed using the RPFEM, as $q=1.39$ γB for $D=0.25$ B and $q=4.51$ γB for $D=1.0$ B. As expected, the vertical and horizontal extents of the failure mode increased in the sand layer, which contributed to the increase in the size of the normal stress distribution and the ultimate bearing capacity of the two-layered soils. The numerical results of the RPFEM showed that the effects of sand layer thickness D on the distribution of the contact normal stress ($\sigma_n/\gamma B$) and the failure mechanism

for the two friction conditions are considerable.

a) Rough condition, $D=0.25 B$ ($q=1.39 \gamma B$)

b) Rough condition, $D=1.0 B$ ($q=4.51 \gamma B$)
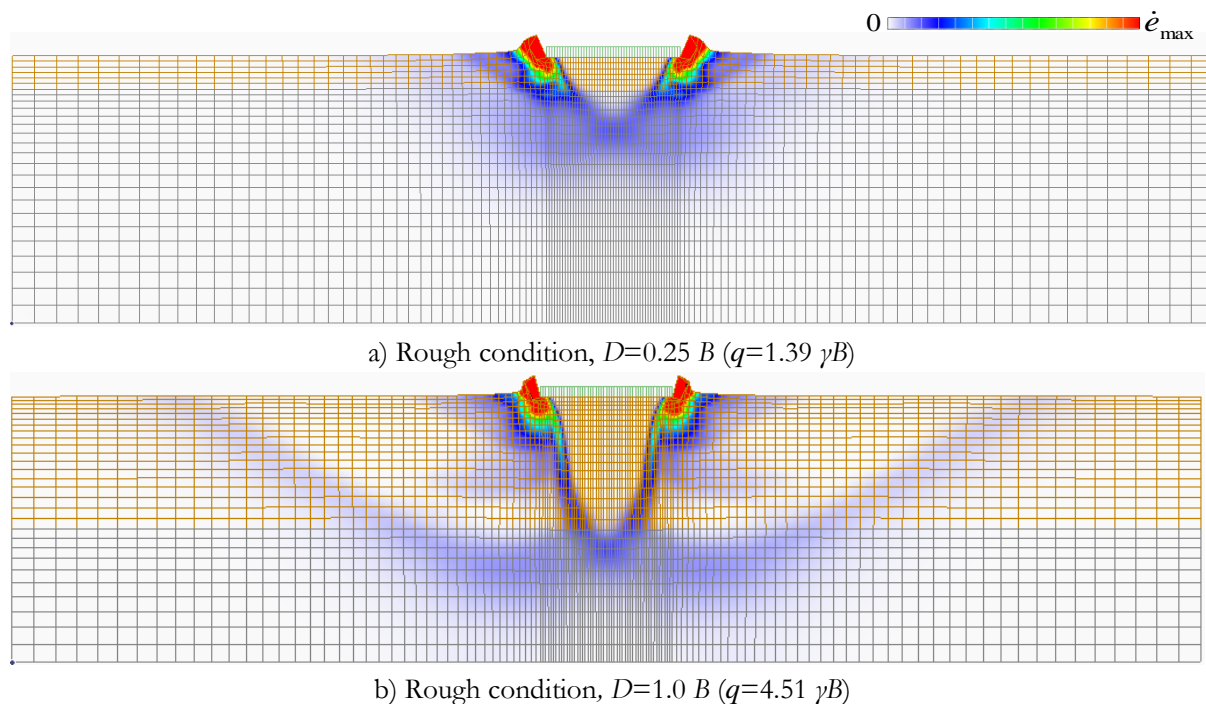
Figure 6.4. Deformation diagrams of footing-soil on sand layer of $\phi=30$ deg overlying clay of $c_u=0.5 \gamma B$ for two typical rough conditions

6.3.2 Case study for increasing internal friction angle and thickness of sand layer

In geotechnical practice, the top layer of soft clay in native soils is often replaced by cohesionless soil in order to improve the bearing capacity of the substrate. Thus, this study widely investigates the improvement of the ultimate bearing capacity by increasing sand layer thickness D and internal friction angle ϕ in a case study of a weak clay layer. Moreover, focus is placed on evaluating the critical depth of the sand layer for two friction conditions. Critical depth D_{cr}, is defined as the minimum depth at which the failure mode develops completely within the sand layer. The values for the sand layer thickness were varied in the range of $D=0.0 B$ to -5.0 B, while the undrained shear strength of c_u was set as a small cohesion in the range of 0.125 to 3.0 γB in order to simulate the weak clay layer.

Figure 6.5 presents dimensionless bearing capacity $q/\gamma B$ by increasing normalized thickness D/B for various values of $\phi=30, 35$, and 40 deg for the rough and smooth conditions. In the figure, $q/\gamma B$ is seen to increase proportionally as thickness D and the value of ϕ are increased. These plots clearly demonstrate an improvement in the bearing capacity resulting from increases in sand layer thickness D and internal friction angle ϕ. However, it can be seen that the increase in ϕ is more dominant with a larger bearing capacity than

the increase in thickness D. This is because that the ultimate bearing capacities of the rough and smooth footings in the case of ϕ=40 deg are determined as close to 44.88 γB and 23.84 γB, respectively, which are much larger values than those in the case of ϕ=30 deg. When the sand layer thickness reaches the critical depth, D_{cr}, $q/\gamma B$ becomes the constant value of a single layer of sandy soil. The magnitude of critical depth D_{cr} seems to be dependent on the value of ϕ and the level of c_u. Moreover, the critical depth for the rough condition is observed to be greater than that for the smooth condition. Thus, increasing the sandy layer thickness will not affect the ultimate bearing capacity regardless of the friction condition. From **Fig. 6.5**, for one typical case of ϕ=30 deg and c_u=0.50 γB, it is easy to determine that critical depth D_{cr} is nearly equal to 2.0 B for the rough condition, while the value is observed at around 1.0 B for the smooth condition. These results agree well with those using a value slightly lower than the thickness D_{cr}=2.0 B reported by Shiau et al. (2003) for the rough condition. They indicate that the RPFEM can provide reasonable predictions of the ultimate bearing capacity and the critical depth of the sand layer by increasing thickness D and ϕ for both friction conditions. However, it should be noted that, despite the need for a greater thickness of the sandy layer, the maximum improvement is considerably intensified by increasing ϕ.

The results obtained for the strain rate distribution of the footing on a sand layer of ϕ=30 deg and D=0.5 B overlying weak clay of c_u=0.5 γB for the rough and smooth conditions are shown in **Fig. 6.6**. It is interesting that the failure modes for the two friction conditions are observed to be almost similar in shape. These results are completely opposite to those for a single layer of sandy soil. It can be understood that two rigid wedges form below the smooth footing base, but that its depth exceeds the sand layer thickness. This leads to the failure mechanism of the smooth footing being characterized as the punching shear failure in same way as that of the rough footing. The size of the rigid sand block below the footing base for the rough condition seems to slightly larger than that for the smooth condition. These results agree well with the results obtained in Shiau et al. (2003). Moreover, ultimate bearing capacity q was obtained as a value close to 2.92 γB for the rough condition and 2.76 γB for the smooth condition. The difference in ultimate bearing capacities due to the footing roughness is not so large in the case study of the weak clay layer.
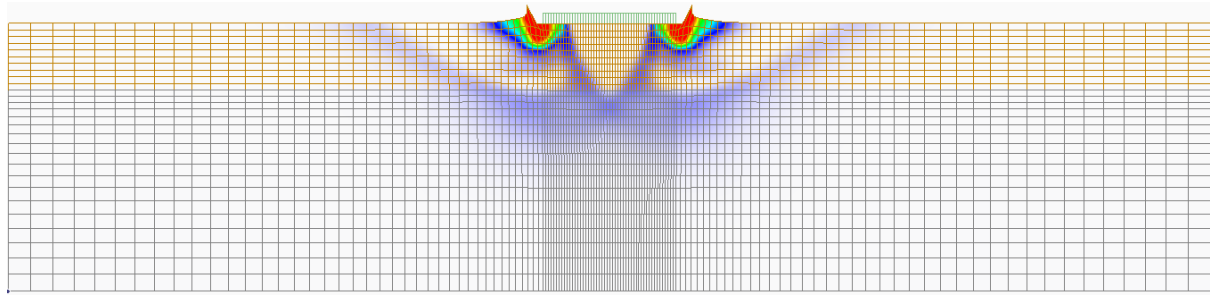
a) ϕ=30 deg

b) ϕ=35 deg

c) ϕ=40 deg
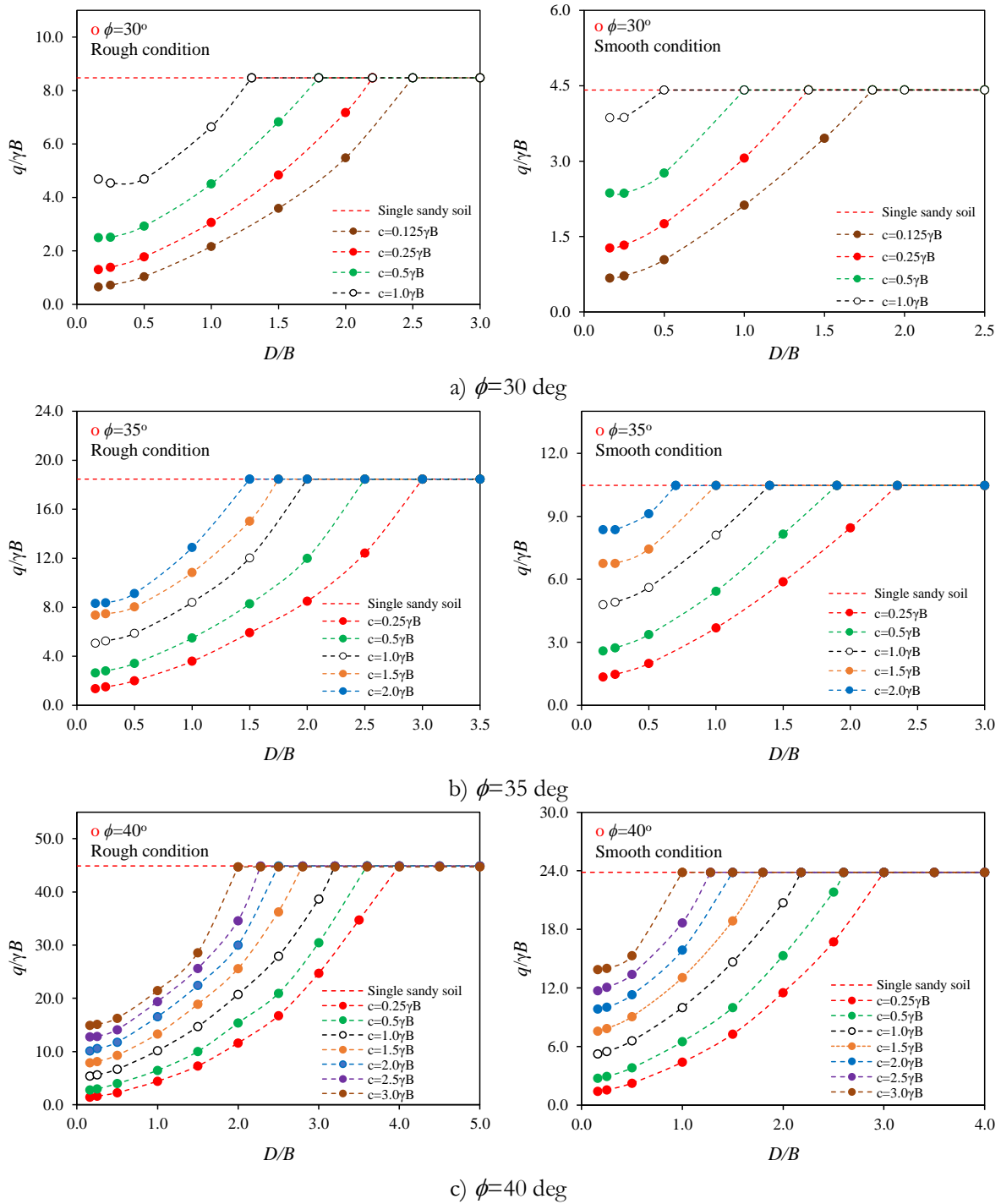
Figure 6.5. Design charts of dimensionless bearing capacity $q/\gamma B$ by increasing sand layer friction angle and thickness for rough and smooth conditions

a) Rough condition, q=2.92 γB
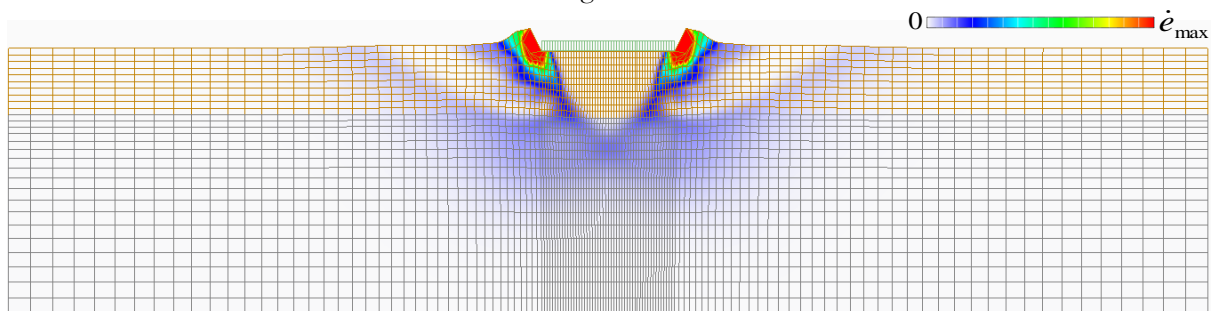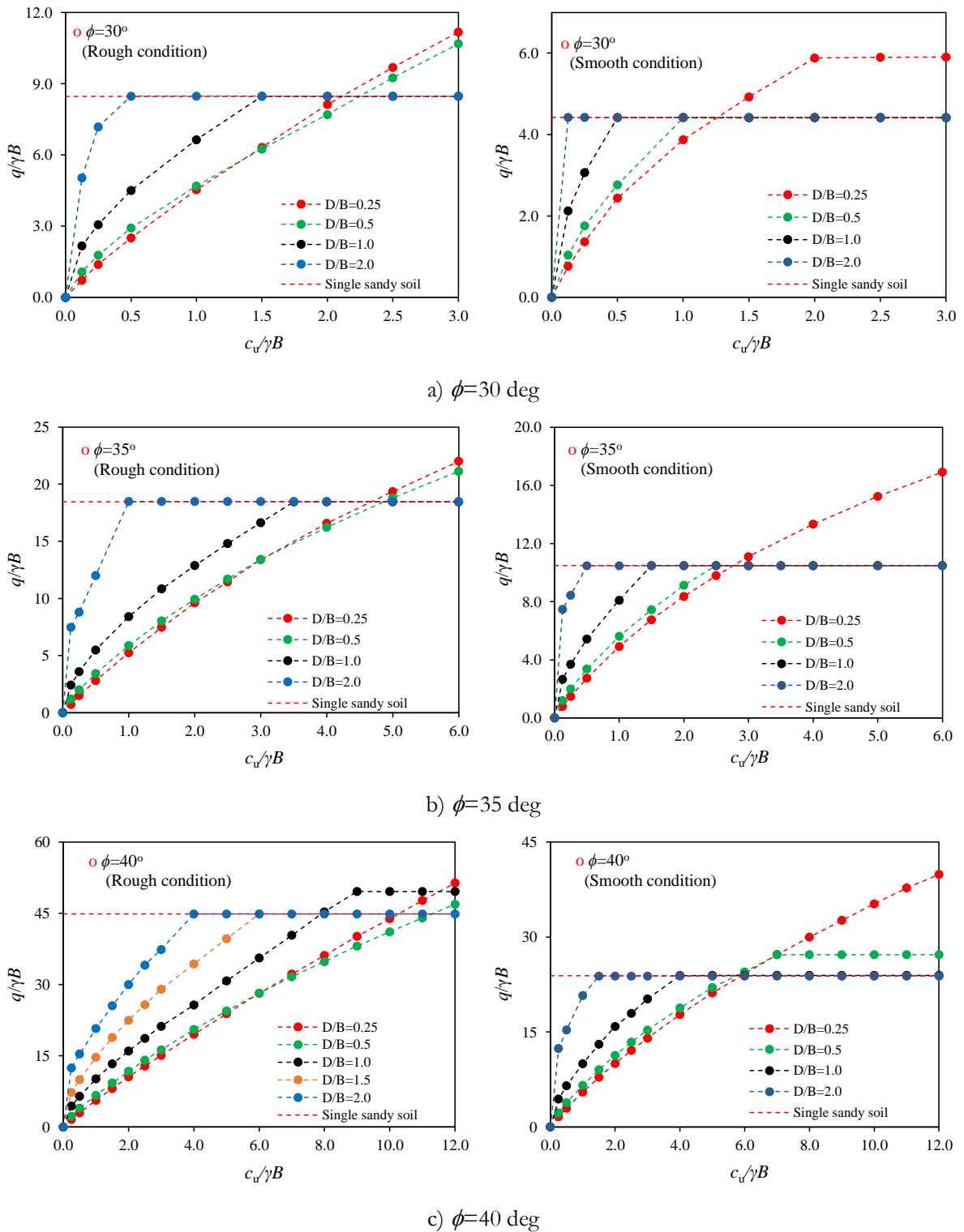
b) Smooth condition, $q=2.76\ \gamma B$

Figure 6.6. Deformation diagrams of footing-soil on sand layer of $\phi=30$ deg and $D=0.5\ B$ overlying clay of $c_u=0.5\ \gamma B$

6.3.3 Case study for increasing undrained shear strength of clay layer

The study widely evaluates the ultimate bearing capacity by assuming larger shear strength c_u for the clay layer for the two friction conditions. A question arises with the failure mechanism of two-layered soils as to whether or not the mechanism is affected by the footing roughness when the shear strength of the clay is large. Values for sand layer thickness D were varied in the range of 0.25 B to 2.0 B, while the undrained shear strength of c_u was set to increase from small cohesion to large cohesion in order to simulate the stiff clay layer.

The effects of the shear strength of the clay layer, $c_u/\gamma B$, on the dimensionless bearing capacity, $q/\gamma B$, for the various values for ϕ are illustrated in **Figs. 6.7(a)** to **(c)** for the rough and smooth conditions. These figures show that the bearing capacity increases with an increase in $c_u/\gamma B$, and that its growth is nearly non-linear in proportion to this quantity. It is interesting to note that if thickness D is smaller than a critical depth D_{cr}, the limit value of $q/\gamma B$ is observed to be larger than that of a single layer of sandy soil. This is because the thin sand layer is supported by the stiff clay layer which is able to support a higher applied load. When D is larger than a critical depth D_{cr}, the limit value of $q/\gamma B$ reaches the ultimate bearing capacity of a single layer of sandy soil. This is because the failure mode of the footing-soil system develops completely within the sand layer at a certain depth which is similar to that of a single layer of sandy soil. The existence of a certain depth is shown clearly in **Fig. 6.7**; critical depth D_{cr} are approximately equal to 1.0 B for $\phi=30$ and 35º and 1.5 B for $\phi=40$º of the rough condition, while they are nearly equal to 0.5 B for $\phi=30$ and 35º and 1.0 B for $\phi=40$º for the smooth condition. Similar results can be found in the computational results of Michalowski et al. (1995) with the value of the critical depth of $D_{cr}=1.0\ B$ for $\phi=30$ and 35º in the case of

the rough condition.

Figure 6.7. Design charts of dimensionless bearing capacity $q/\gamma B$ by increasing clay layer shear strength c_u for rough and smooth conditions

Figures 6.8(a) and **(b)** show the deformation diagrams of the footing-soil system in the cases of sand ϕ=30 deg and D=0.5 B overlying the stiff clay layer of c_u=3.0 γB for the rough and smooth conditions,

respectively. It can be seen that the general failure mode is observed to be completely contained within the sand layer regardless of the friction condition, and that the size of the failure mode seems to smaller than that of a single layer of sandy soil. For the rough condition, the failure mechanism of the rigid footing is presented as a rigid triangular wedge in the sand layer, and the deformation of the ground that is almost less occurs in the clay layer. For the smooth condition, the failure mechanism is characterized by two rigid wedges within the sand layer. It proves that the footing roughness has a significant effect on the failure mechanism of a footing when the clay shear strength becomes larger. Moreover, the ultimate bearing capacity was obtained as a value close to 10.68 γB for the rough condition which is greater than that of 4.42 γB for the smooth condition. The difference in ultimate bearing capacities due to the footing roughness is very large in the case of the stiff clay layer. It can be seen that giving consideration to the large shear strength of the clay layer leads to improvement in ultimate bearing capacity of the rigid footing, and the difference between the two friction conditions is clarified.

a) Rough condition, q=10.68 γB

b) Smooth condition, q=4.42 γB
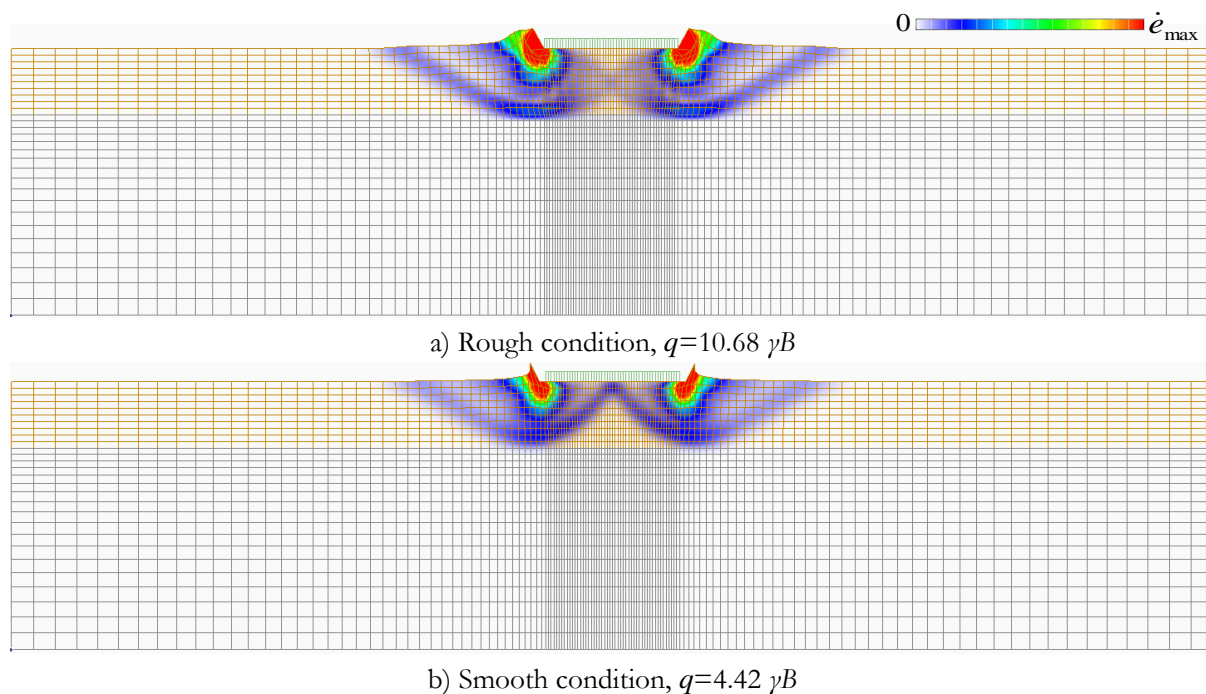
Figure 6.8. Deformation diagrams of footing-soil on sand layer of ϕ=30 deg and D=0.5 B overlying stiff clay layer c_u=3.0 γB

6.4 BEARING CAPACITY MODEL OF FOOTING ON SAND LAYER OVERLYING CLAY

6.4.1 Propose for bearing capacity model

It can be concluded from the results of the RPFEM analysis that the bearing capacity of a rigid footing

on two-layered soils can be presented as follows:

$$\frac{q}{\gamma B} = f\left(\phi, \frac{c_u}{\gamma B}, \frac{D}{B}, \text{friction - condition}\right) \tag{1}$$

According to the shape of the failure mode obtained from the RPFEM analysis, the failure mode of two-layered soils was found to change from the punching shear failure to the general shear failure by an increase in the shear strength of the clay layer. This study widely investigates the limit equilibrium condition of a rigid sand block during punching shear failure. **Figure 6.9** shows the sidelines of the rigid sand block creating shear angle θ in the shear plane. One problem arises, namely, that the magnitude of shear angle θ may be a positive angle or a negative angle, as shown in **Figs. 6.9(a)** and **(b)**, respectively. In the bearing capacity model, if shear angle θ is known, the ultimate bearing capacity of the rigid footing on sand overlying clay can be calculated. **Figure 6.10** shows the failure mechanism assumed for the shear angle θ of the rigid sand block during punching shear failure. It can be seen that vertical force P_v along the shear plane is shown to be completely dependent on the geometry of the sand block, the normal stress acting on the sand block which is considered by the coefficient of the passive earth pressure K_p, and mobilised friction angle δ as follows:

$$P_v = P_n \sin(\pm\theta) + P_\tau \cos\theta = P_n \sin(\pm\theta) + P_n \tan\delta \cos\theta = \gamma D^2 K_p \left(\tan(\pm\theta) + \tan\delta\right) \tag{2}$$

Meyerhof (1974) and Hana (1981) reported that, in practice, it is convenient to use a coefficient (K_s) of punching shear resistance to quantify the vertical component of the total force acting on shear plane. In this study, vertical force P_v is estimated to express the influence of the above via the coefficient (K_s) as follows:

$$P_v = \gamma D^2 K_s \tan\phi \qquad \text{with} \qquad K_p\left(\tan(\pm\theta) + \tan\delta\right) = K_s \tan\phi \tag{3}$$

The limit equilibrium condition of the rigid sand block has been applied in order to estimate the ultimate bearing capacity of a rigid footing, as seen in the following equation:

$$q.B = \gamma D^2 K_s \tan\phi + \left(N_c c_u + \gamma D\right)\left[B + 2D\tan\left(\pm\theta\right)\right] - \left[B + D\tan\left(\pm\theta\right)\right]\gamma D \tag{4}$$

For a simpler equation,

$$\frac{q}{\gamma B} = \left(\frac{D}{B}\right)^2 K_s \tan\phi + N_c \frac{c_u}{\gamma B}\left[1 + 2\frac{D}{B}\tan\left(\pm\theta\right)\right] + \left(\frac{D}{B}\right)^2 \tan\left(\pm\theta\right) \le \frac{q_s}{\gamma B} \tag{5}$$

where N_c is the bearing capacity factor for clayey soil, and exact plasticity solution N_c is 5.14. The inequality

in Eq. (5) suggests that the ultimate bearing capacity cannot exceed the value of q_s, which is the bearing capacity of the rigid footing resting on a single layer of sandy soil corresponding to different friction conditions. The unknown parameters of Eq. (5) are shear angle θ and punching shear coefficient K_s, which can be estimated by an RPFEM analysis. Shear angle θ is determined graphically from effective footing width B' by the contour lines of the strain rate distribution, as shown in **Fig. 6.9**. A series of analyses was conducted in the cases of a sand layer of ϕ=30, 35, and 40 deg with D=0.25 to 2.0 B, and a clay layer of $c_u/\gamma D$=0-8.0. **Figure 6.11** shows the relationship between shear angle θ against normalized clay shear strength $c_u/\gamma D$ for rough and smooth conditions. It can be seen that shear angle θ seems to greatly depend on the values of ϕ and $c_u/\gamma D$, but not on the value of D/B. Moreover, the value of shear angle θ only occurs with a positive angle if internal friction angle ϕ is large and $c_u/\gamma D$ is small. The results illustrated in **Fig. 6.11** suggest that shear angle θ is a function of the relative strength of the two layers, ϕ and $c_u/\gamma D$. This study proposes a new equation to quantify shear angle θ based on the form of the formula by Eshkevari et al. (2019).

$$\theta(\text{rad}) = A.\ln\left(c_u / \gamma D\right) + B \tag{6}$$

where
$$\begin{cases} A = 0.02\ln\left(\tan\phi\right) - 0.16 \\ B = 0.49\ln\left(\tan\phi\right) - 0.05 \end{cases} \quad \text{for the rough condition} \tag{7}$$

$$\begin{cases} A = 0.03\ln\left(\tan\phi\right) - 0.18 \\ B = 0.55\ln\left(\tan\phi\right) - 0.115 \end{cases} \quad \text{for the smooth condition} \tag{8}$$

Figure 6.12 shows punching shear coefficient K_s for various values of ϕ which were calculated from the results of the RPFEM through Eq. (5). The value of K_s increases as normalized shear strength $c_u/\gamma D$ increases. The figure demonstrates that K_s greatly depends on the values of ϕ and $c_u/\gamma D$, but not on the value of D/B. From **Fig. 6.12**, this study proposes a new equation to quantify K_s based on the form of the formula by Eshkevari et al. (2019).
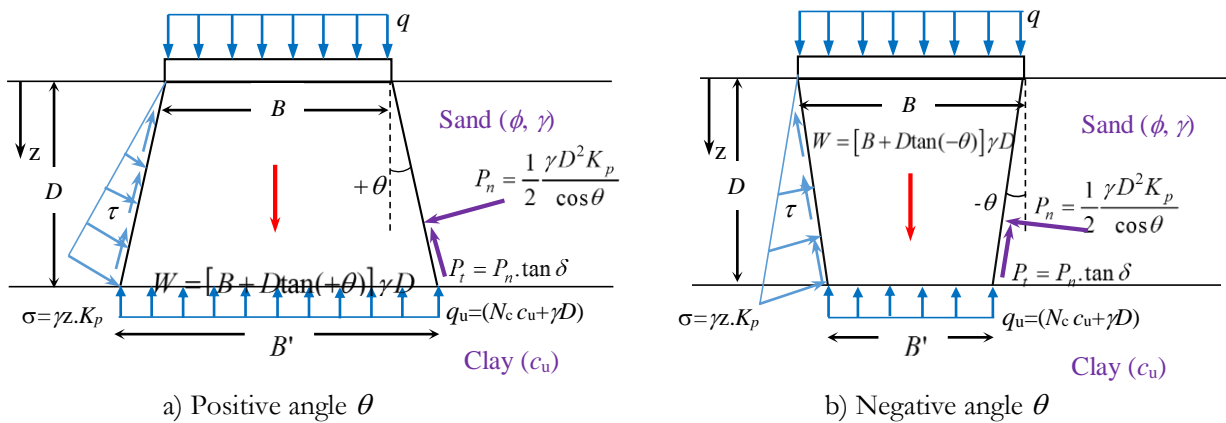
$$K_s = C.\left(c_u / \gamma D\right) + 2 \tag{9}$$

where $\quad C = -3.51\left(\tan\phi\right) + 8.7 \quad$ for the rough condition $\tag{10}$

$$C = -3.2\left(\tan\phi\right) + 9.1 \text{ for the smooth condition} \tag{11}$$

a) Positive angle θ
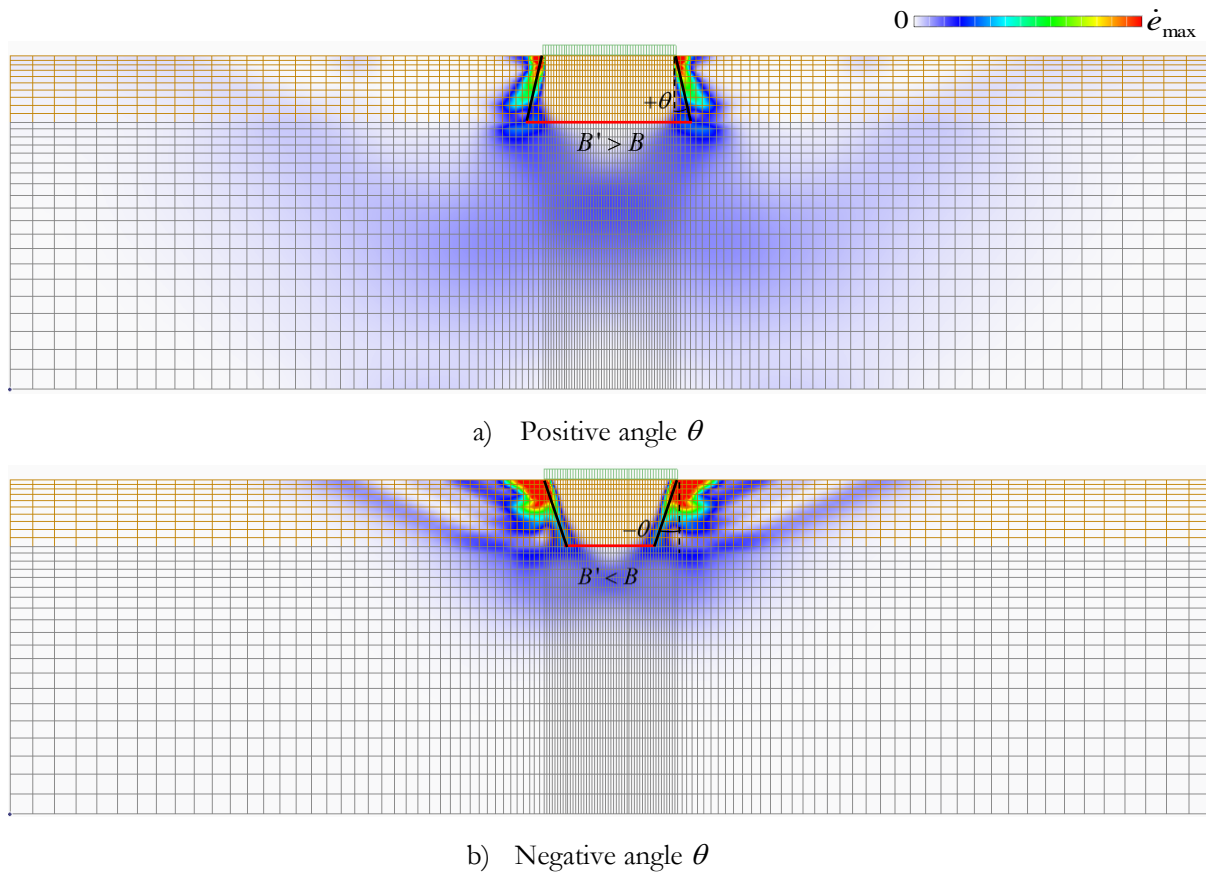
b) Negative angle θ

Figure 6.9. Distributions of strain rates for determination of effective footing width B' in two cases of positive and negative angles θ

a) Positive angle θ b) Negative angle θ

Figure 6.10. Failure mechanism assumed by Eshkevari et al. (2019) for rough condition
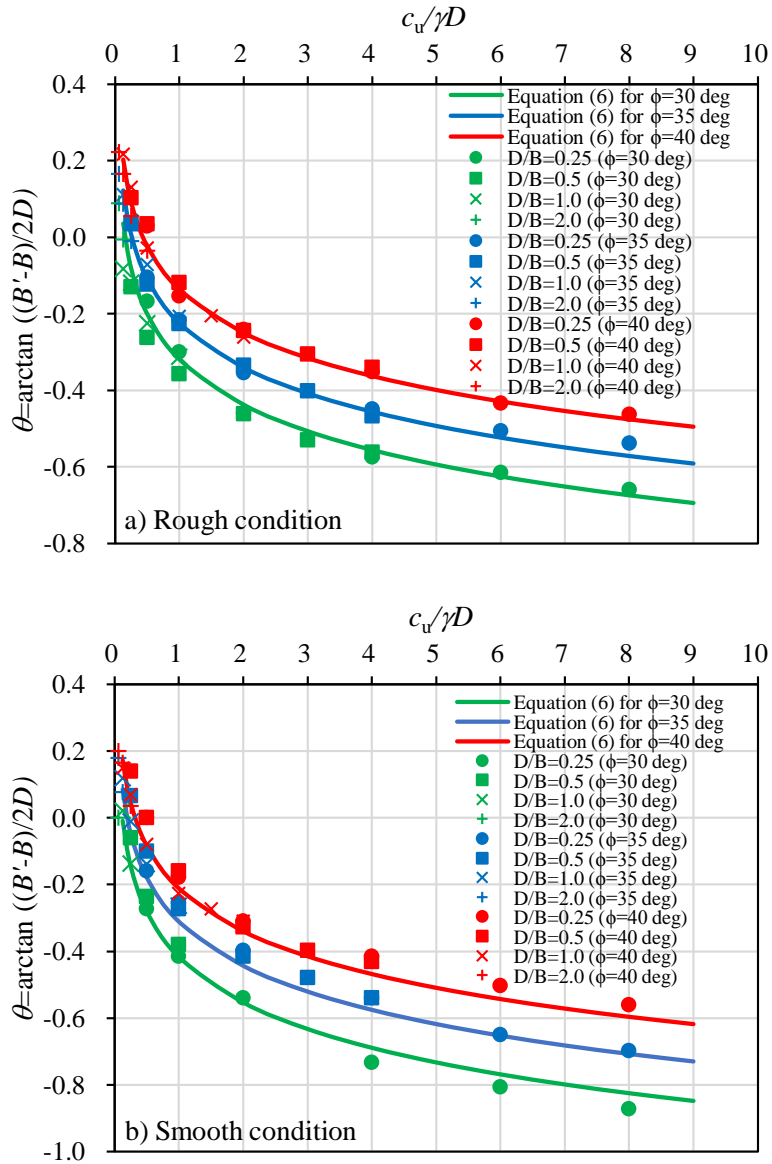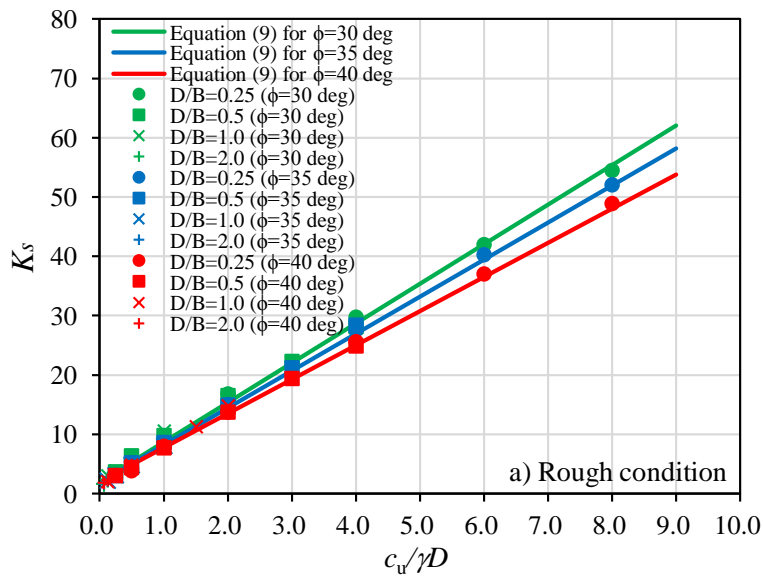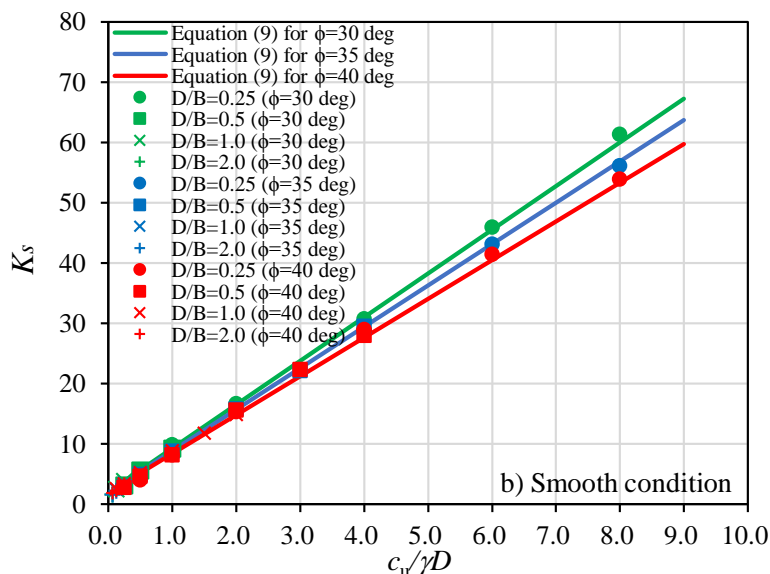
Figure 6.11. Variation in shear angle θ with dimensionless clay strength $c_u/\gamma D$ for various values of ϕ

Figure 6.12. Variation in coefficient K_s with dimensionless clay strength $c_u/\gamma D$ for various values of ϕ

6.4.2 Validation of the developed approach

To validate the proposed equation, this study performs a comparison between the dimensional bearing capacity $(q/\gamma B)$ of Eq. (5) and $(q/\gamma B)$ of the RPFEM with a total of nearly 250 data values, where ϕ=30, 35, and 40 deg, $c_u/\gamma B$=0.25-12.0, and D/B=0.25-2.0 for both rough and smooth conditions. All of the estimated values need to be within ±20% of the 1:1 line, as shown in **Fig. 6.13**. The horizontal-axis of the figure shows the measured bearing capacity $(q_m/\gamma B)$ of the RPFEM analysis, while the vertical-axis of the figure shows the calculated bearing capacity $(q_c/\gamma B)$ of Eq. (5). The figure indicates that the proposed equation has a high predictive ability for the bearing capacity of sand overlying clay. In design practice, the factor of safety is widely introduced in the assessment of bearing capacity. The value in factor of safety is generally taken as Fs=3.0 due to the poor information on ground condition, especially on the soil constants. The applicability of the proposed equation is thought to be admissible from the precision ratio in **Figures 6.11 to 13**.

Yamamoto et al. (2005) used the finite element analysis to find the exact limit load of a rough rigid footing on a sand layer overlying clay. In this study, the bearing capacity values predicted with the proposed equation, Eq. (5), are compared against the superposition formulas of Meyerhof (1974) and Eshkevari et al. (2019) and the FEM of Yamamoto et al. (2005) for the rough and smooth conditions, as shown in **Fig. 6.14**. The results obtained with the RPFEM are observed as being slightly higher than those of Eshkevari

et al. (2019) at large shear strength c_u, and smaller than those of Meyerhof (1974). However, they show a good agreement with those of the FEM of Yamamoto et al. (2005) for all values of c_u under the rough condition. In addition, the figure shows that dimensional bearing capacity $q/\gamma B$ for the rough condition is observed to be almost the same as that for the smooth condition at a small shear strength c_u regardless of the values of ϕ and D/B. However, the difference becomes greater as shear strength c_u increases, due to the effect of the upper sand layer, and the footing roughness dominates more than the clay layer. The results indicate that the new equation for the RPFEM can provide reasonable predictions of the bearing capacity of a rigid footing on sand-over-clay during punching shear failure, which is simple and efficient enough to be used in engineering practice.
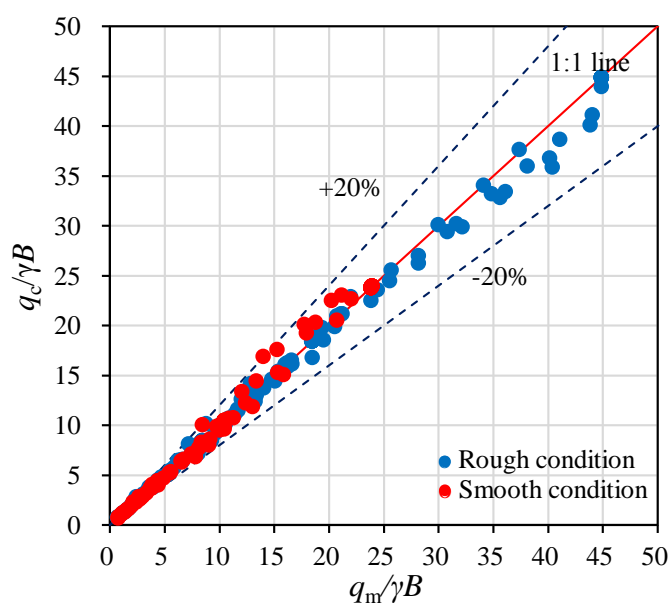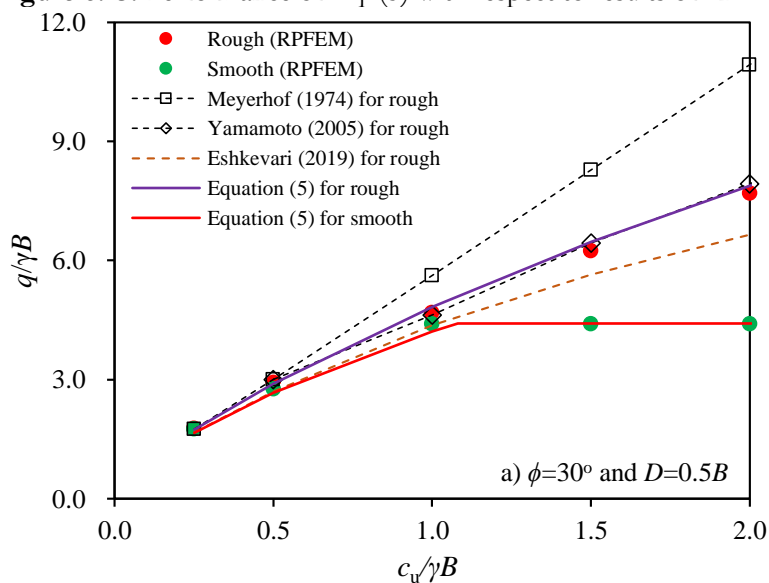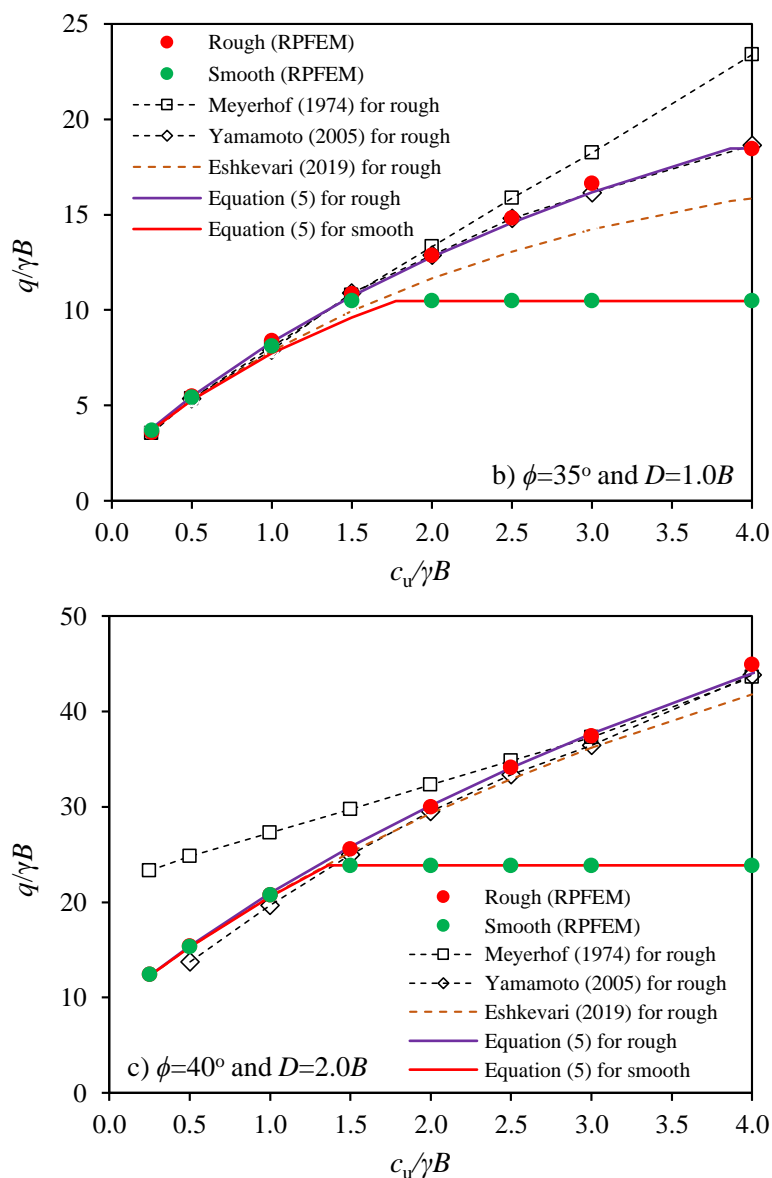

Figure 6.13. Performance of Eq. (5) with respect to results of RPFEM

Figure 6.14. Dimensionless bearing capacity $q/\gamma B$ for various values of $c_u/\gamma B$ from RPFEM compared with results found in literature for cases of $\phi=30$, 35, and 40 deg with $D =0.5B$, 1.0B, and 2.0B

6.5 CONCLUSION

This study has investigated the ultimate bearing capacity of a vertically loaded footing on sand-over-clay using the rigid plastic finite element method (RPFEM). The effects of the soil properties and the geometric conditions of two-layered soils on the ultimate bearing capacity and the failure mechanism were analyzed. The conclusions of this study are as follows.

1. An interface element was used to simulate the contact footing-soil plane validating that the method was effective for analyzing the interaction between the footing and the soil. The effect of the friction condition of the footing surface was found to reflect the different failure modes of the footing-soil system. The failure

mechanism has been verified with that discussed in past work.

2. The effect of the sand layer thickness on the shape and size of the contact normal stress distribution for two friction conditions was clarified. The distribution of the normal stress was found to reflect the combined shape of two-layered soils according to each magnitude of the sand layer thickness. When the sandy layer thickness was increased, the influence of the top sand layer on the contact normal stress was raised and the influence of the lower clay layer was lowered. The sand layer thickness reached the sufficiently large depth, and the normal stress distribution was observed to coincide with that of a single layer of sandy soil corresponding to each friction condition.

3. For sand over a weak clay layer, the results obtained from the RPFEM suggested that a greater internal friction angle and a greater thickness of the sand layer are the improvements seen for the ultimate bearing capacity. However, it is noted that the increase in the internal friction angle was more dominant with a higher bearing capacity than that of the sand layer thickness. The maximum improvement in the bearing capacity was obtained at the critical depth of sand layer which depended on the value of ϕ, the level of c_u, and the friction condition of the footing surface. Moreover, punching shear failure formed in the sand layer as a rigid sand block, while general shear failure formed in the clay layer as a rigid triangular wedge regardless of the friction condition.

4. For sand over a stiff clay layer, the improvement in the ultimate bearing capacity was intensified by increasing the undrained shear strength. The ultimate bearing capacity was observed to surpass that of a single layer of sandy soil in the case study with a thin thickness of the sand layer. However, when the sand layer thickness was large, the ultimate bearing capacity coincided with that of a single layer of sandy soil. General shear failure formed within the sand layer as a rigid triangular wedge for the rough condition and as two rigid triangular wedges for the smooth condition.

5. From the numerical results of the RPFEM, during punching shear failure, it is concluded that the ultimate bearing capacity of sand-over-clay is a function of the sand layer friction angle, its thickness, the clay layer shear strength, and the friction condition. Shear angle θ and punching shear coefficient K_s are functions of ϕ and $c_u/\gamma D$, the relative strength of the two layers, and do not depend on footing width B. A new equation was proposed to predict the bearing capacity of a rigid footing with a wide range of problem parameters for both friction conditions.

✧ **Publication:** Chapter 6 will be submitted as article: **Pham, N. Quang**, Ohtsuka, S.: Ultimate bearing capacity of rigid footing resting on sand layer overlying clay, **Journal of Geotechnical and Geoenvironmental Engineering (ASCE)**, 2020:

References.

Asaoka, A., and Ohtsuka, S., 1986. The analysis of failure of a normally consolidated clay foundation under embankment loading. Soils and Foundations. 26(2), 47-59.

Asaoka, A., and Ohtsuka, S., 1987. Bearing capacity analysis of a normally consolidated clay foundation. Soils and Foundations. 27(3), 58-70.

Asaoka, A., Ohtsuka, S., and Matsuo, M., 1990. Coupling analyses of limiting equilibrium state for normally consolidated and lightly overconsolidated soils. Soils and Foundations. 30(3), 109-123.

Meyerhof, G. G. (1951). The ultimate bearing capacity of foundations. Geotechnique; 2(4): 301-332.

Meyerhof, G. G. (1974). Ultimate bearing capacity of footings on sand layer overlying clay. Canadian Geotechnical Journal, 11(2), 223-229.

Michalowski, R. L., and Shi, L. (1995). Bearing capacity of footings over two-layer foundation soils. Journal of Geotechnical Engineering; 121(5): 421-428.

Hanna, A. M., and Meyerhof, G. G. (1980). Design charts for ultimate bearing capacity of foundations on sand overlying soft clay. Can Geotech J; 17(2): 300-303.

Hana, A. M., (1981). Foundations on strong sand overlying weak sand. J Geotech Eng; 107(7): 915-27

Hansen, J. B. (1970). A revised and extended formula for bearing capacity. Bulletin of the Danish Geotechnical Institute, 28. 5-11.

Hoshina, T., Ohtsuka, S., and Isobe, K., 2011. Rigid plastic analysis for slope including thin weak layer. Geotechnical Journal. 6, 191-200 (in Japanese).

Hossain, M. S., Hu, Y., & Ekaputra, D. (2014). Skirted foundation to mitigate spudcan punch-through on sand-over-clay. Géotechnique, 64(4), 333-340.

Nguyen, D. L., Ohtsuka, S., Hoshina, T., & Isobe, K. (2016). Discussion on size effect of footing in ultimate bearing capacity of sandy soil using rigid plastic finite element method. Soils and foundations, 56(1), 93-103.

Okamura, M., Takemura, J., Kimura, T. (1997). Centrifuge model tests on bearing capacity and deformation of sand layer overlying clay. Soils and Found; 37(1): 73-88.

Okamura, M., Takemura, J., & Kimura, T. (1998). Bearing capacity predictions of sand overlying clay based on limit equilibrium methods. Soils and Foundations, 38(1), 181-194.

Pham, Q. N., Ohtsuka, S., Isobe, K., & Fukumoto, Y (2019a). Group effect on ultimate lateral resistance of piles against uniform ground movement. Soils and Found. 59(1): 27-40.

Pham, Q. N., Ohtsuka, S., Isobe, K., Fukumoto, Y., & Hoshina, T (2019b). Ultimate bearing capacity of rigid footing under eccentric vertical load. Soils and Found. 59(6): 1980-1991.

Pham, Q. N., Ohtsuka, S., Isobe, K., & Fukumoto, Y (2020). Limit load space of rigid footing under eccentrically inclined load. Soils and Found. 60(4), 1-14.

Rajaei, A., Keshavarz, A., & Ghahramani, A. (2019). Static and seismic bearing capacity of strip footings on sand overlying clay soils. Iranian Journal of Science and Technology, Transactions of Civil Engineering, 43(1), 69-80.

Salimi Eshkevari, S., Abbo, A. J., & Kouretzis, G. (2019). Bearing capacity of strip footings on sand over clay. Canadian Geotechnical Journal, 56(5), 699-709.

Shiau, J. S., Lyamin, A. V., & Sloan, S. W. (2003). Bearing capacity of a sand layer on clay by finite element limit analysis. Canadian Geotechnical Journal, 40(5), 900-915.

Tamura, T., Kobayashi, S. and Sumi, T., 1984. Limit analysis of soil structure by rigid plastic finite element method. Soils and Foundations. 24 (1), 34-42.

Tamura, T., Kobayashi, S. and Sumi, T., 1987. Rigid Plastic Finite Element Method for Frictional Materials. Soils and Foundations. 27 (3), 1-12.

Tamura, T., Kobayashi, S. and Sumi, T., 1990. Rigid Plastic Finite Element Method in Geotechnical Engineering Computational. Current Japanese Material Research. 15-23.

Teh, K. L., & Leung, C. F. (2010). Centrifuge model study of spudcan penetration in sand overlying clay. Géotechnique, 60(11), 825-842.

Terzaghi, K. R. B. Peck (1948). Soil Mechanics in Engineering Practice. New York, John Wiley and Sons.

Yamamoto, K., Hira, M (2005). Bearing capacity analysis of rigid strip footings on sand overlying clay. Journal of Applied Mechanics; 8: 337-348. (in Japanese).

Zheng, G., Wang, E., Zhao, J., Zhou, H., & Nie, D. (2019). Ultimate bearing capacity of vertically loaded strip footings on sand overlying clay. Computers and Geotechnics, 115, 103151.